NONCOHERENT SEQUENCE DETECTION RECEIVER FOR BLUETOOTH SYSTEMS

by

Mani Jain

B.Tech., Regional Engineering College Kurukshetra, India, 1995

A THESIS SUBMITTED IN PARTIAL FULFILLMENT OF
THE REQUIREMENTS FOR THE DEGREE OF
Master of Applied Science
in
THE FACULTY OF GRADUATE STUDIES
(Department of Electrical and Computer Engineering)

We accept this thesis as conforming
to the required standard

The University of British Columbia

September 2004

Library Authorization

In presenting this thesis in partial fulfillment of the requirements for an advanced degree at the University of British Columbia, I agree that the Library shall make it freely available for reference and study. I further agree that permission for extensive copying of this thesis for scholarly purposes may be granted by the head of my department or by his or her representatives. It is understood that copying or publication of this thesis for financial gain shall not be allowed without my written permission.

MANI JAIN
Name of Author *(please print)*

21/09/2004
Date (dd/mm/yyyy)

Title of Thesis: Noncoherent sequence detection receiver for Bluetooth systems.

Degree: M A Sc. Year: 2004

Department of Electrical and Computer Engineering
The University of British Columbia
Vancouver, BC Canada

Abstract

Bluetooth is an increasingly popular and widely deployed standard for wireless personal area networks (WPAN). The Bluetooth physical layer employs Gaussian frequency shift keying (GFSK), which is a particular form of continuous phase modulation (CPM). GFSK provides a favorable trade-off between power and bandwidth efficiency, and allows for low-complexity transmitter and receiver implementations. A simple discriminator detector is used to recover the GFSK modulated data in Bluetooth devices.

Though structurally and computationally simple, discriminator detectors are very power inefficient. Coherent sequence detectors are significantly more power efficient for modulation schemes with memory, since the memory introduced by CPM is properly taken into account. However, realization of sequence detection (SD) for Bluetooth systems is very difficult because the modulation index h is allowed to vary in a wide interval. This varying modulation index leads to a varying trellis structure for SD with possibly a large number of states. The design of the optimal receiver filter for a sufficient statistic for SD after sampling is also dependent on h. The receiver filter design is further complicated by the operation of Bluetooth systems in a license-free band, thereby, requiring the designed receiver filter to be robust against interference from other devices operating in the same band. Moreover, coherent SD requires phase synchronization, which is a difficult task as well because of the frequency hopping radio of Bluetooth and the allowed local oscillator dynamics.

Several approaches to a simple and power-efficient receiver design for Bluetooth have

been discussed in the literature. The drawbacks of these approaches are that either the achieved power efficiency is insufficient or perfect channel phase estimation at the receiver has been assumed. These designs are restricted to a particular value of h and the effects of high frequency offsets at the receiver oscillator on the performance have not been accounted for. Therefore, the practical applicability of these receivers is limited.

In the present research work, a novel noncoherent SD (NSD) receiver for Bluetooth systems is proposed. The receiver design is based on the decomposition approach to CPM and the concept of noncoherent sequence detection of CPM. A low-complexity implementation of the receiver is presented with only one receiver filter and NSD on a two-state trellis, which accomplishes significant performance gains of more than 4 dB over the discriminator-based detector. The proposed receiver caters to the requirements of Bluetooth systems comprehensively in that (a) the entire range of possible h is considered and an adaptive solution to account for varying h is provided, (b) a frequency offset compensator is incorporated into NSD to cope with the large local oscillator frequency deviations allowed in Bluetooth systems, and (c) improved decoding methods for the forward error correction (FEC) schemes employed in Bluetooth are devised. Simulation and analytical results verify that the presented NSD receiver operates close to the theoretical limits. The proposed receiver is robust and simple, and therefore, is an attractive solution for Bluetooth devices.

Contents

List of Figures

List of Tables

Acknowledgments

It is a pleasure to convey my gratitude to my research supervisor Dr. Robert Schober and co-supervisor Dr. Lutz Lampe for guiding me throughout this research work. Their constant encouragement and critical assessment of the thesis work helped me finish a challenging project. The various discussions we had from time to time were fruitful and the team work was instrumental in allowing me to acquire the required skills and achieve the proposed research objectives. The courses offered by Dr. Robert Schober on 'Detection and Estimation of Signals in Noise' and by Dr. Cyril Leung on 'Communication and Information Theory' helped me build strong fundamentals in digital communications and were of immense value in allowing me to think independently.

I thank National Sciences and Engineering Research Council (NSERC) and Dr. Robert Schober for funding this project.

I would also like to thank the colleagues at the department of Electrical and Computer Engineering, UBC, for creating a stimulating and a friendly environment at work.

Chapter 1

Introduction

The growing dependence of modern man on portable electronic devices created the need to allow these devices to communicate with each other. The sophisticated wireless technology of today provides the solution for convenient wireless connection of electronic devices, giving rise to wireless personal area networks (WPAN). Bluetooth[TM1] is a WPAN technology that enables devices like cellular phones, personal digital assistants, laptops, desktop computers and printers, to communicate with each other at a raw bit rate of 1 Mega bits per second (Mbps) over a short range without using cables [BTS03]. There is a multitude of other useful applications of Bluetooth enabled devices like home and industrial automation, entertainment devices, toys, digital cameras, headsets etc., that can benefit people in many ways [She01]. The important differentiating features of Bluetooth devices from other short range wireless technologies are their low cost, robustness, low complexity, and low power consumption [She01].

The need for an improved global solution for short range wireless communications led Ericsson, IBM, Intel, Nokia, and Toshiba to guide research efforts towards developing the Bluetooth industry standard in 1998 [Bis01]. A Special Interest Group (SIG) was formed by these five companies aimed at creating a user-friendly, flexible, and efficient standard,

[1]The BLUETOOTH trademark in owned by Bluetooth SIG, Inc., USA [She01].

which was later joined by over 3000 other companies [BT.org]. The standard is named after the 10^{th} century Danish king Harald Blatand (Bluetooth in English), who had been instrumental in uniting warring Scandinavian people just as Bluetooth wireless technology allows collaboration between computing, mobile phone, and automotive industries [BT.org]. Since then Bluetooth has grown into a well accepted technology in the telecommunications industry. Bluetooth technology is complementary to the 802.11 wireless local area network (WLAN) technology as the latter caters to higher data rates in bigger areas at higher cost and power consumption. The emerging technology for high data rate short range wireless communications, known as "ultra-wideband", targets similar applications as Bluetooth, but the standard is still in the developmental stage. Bluetooth devices already have a big market and the number of Bluetooth enabled devices entering the market is growing every year. According to the studies made by a market research firm called In-Stat/MDR [BT.com] [Zdnet], the number of Bluetooth chip shipments reached 69 million in 2003, up from 35.8 million in 2002. Shipments are expected to exceed 100 million in 2004 and with the continuing trend are likely to surpass 510 million by the year 2006.

The promising market for Bluetooth devices is the motivating factor to explore the possibility of an improved receiver design for Bluetooth systems. The state-of-the-art receiver for Bluetooth systems uses the noncoherent limiter-discriminator with integrate and dump filter (LDI) [SV01a], which although being very simple and robust, is highly power inefficient. The aim of the present research work is to design a more power efficient receiver, complying with the requirements of the Bluetooth standard.

The following section provides an overview of the Bluetooth system and specification as defined in the standard [BTS03]. The second section of this chapter states the objective of the thesis work more precisely including its motivation and the associated challenges. The contributions of this work are briefly summarized in the third section, and the concluding

section outlines the organization of this thesis.

1.1 The Bluetooth System

Bluetooth devices can communicate with each other using point-to-point or point-to - multipoint radio links within a range of 10 m extendable to 100 m [SV01b]. An interconnection of up to eight such devices forms a piconet. The Bluetooth network may be expanded by interlinking several such piconets together to form a scatternet. For communication of voice and data within piconets and scatternets, Bluetooth provides asynchronous connectionless (ACL) links using packet switching and synchronous connection oriented (SCO) links which use circuit switching [Bis01]. For voice traffic, SCO links are used, which can support voice traffic at 64 Kbps. Time slots at regular intervals are reserved for SCO traffic. For asynchronous data transmission, the ACL provides best-effort links.

The information between the Bluetooth devices is exchanged using packets. A packet can occupy up to five time slots with each time slot having a duration of 625 μs. Each packet is transmitted over a different hop frequency. The general format of a packet is shown in Fig. 1.1.

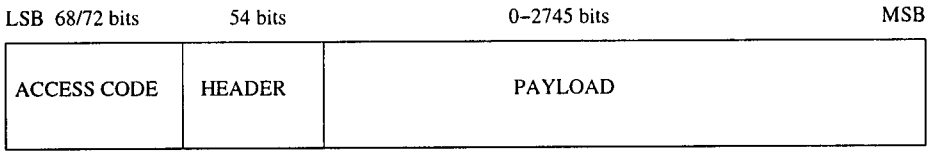

Figure 1.1: General packet format [BTS03].

The packet consists of a 68 or 72 bit long access code, a 54 bit long header, and up to 2745 payload bits. The access code consists of 4 preamble bits, a 64 bit sync word and an optional 4 bit trailer. The generation of the sync word is based on the device's address. Therefore, the sync word is known to the communicating devices, and is used for synchronization and timing acquisition. The header contains relevant link information. Depending upon the

requirements of the communication process, 15 different packet types have been defined. Error correction schemes are also defined for each packet type. 1/3 rate FEC, 2/3 rate FEC or an automatic repeat request (ARQ) scheme for data is used for reliable error free transmission of packets.

To guarantee the compatibility between different radios used in the system and to define the quality of the system, the Bluetooth specifications define the following requirements for Bluetooth radios [BTS03]:

- Bluetooth devices operate in the license free industrial, scientific and medical (ISM) 2.4 GHz band.
- The radio employs frequency hopping spread spectrum (FHSS). The radio hops on a packet by packet basis in a pre-determined sequence at a frequency of 1600 hops/second on 79 channels of 1 MHz bandwidth, located in the 2.400-2.4835 GHz frequency range. The specifications permit a reduced channel hop over only 23 channels for countries that have restrictions in their ISM band [BTS03].
- Gaussian frequency shift keying (GFSK) modulation is used to map binary data symbols to modulated symbols.
- Time division duplexing is employed for full duplex transmission.
- Three classes of Bluetooth devices are defined depending on the maximum transmitter power. Class 1, 2, and 3 devices have maximum transmit powers of 20 dBm (100 mW), 4 dBm (2.5 mW), and 0 dBm (1 mW), respectively [She01].
- The maximum allowed raw bit error rate is specified as 0.1%.

1.2 Challenges and Motivation

The objective of this research work is to design a power efficient, low cost, and robust receiver for Bluetooth devices. The optimum receiver for GFSK modulated signals consists of a correlator followed by a maximum likelihood sequence detector (MLSD) [Pro01, Ch. 5]. However, the trellis structure for sequence detection (SD) is dependent on the modulation index h, which is allowed to vary in a broad interval of 0.28 to 0.35 in the Bluetooth standard [BTS03]. This relaxation results in a varying trellis structure for SD possibly with a large number of states that differs with h, and the complexity of SD increases with the number of states (cf. Section 2.2). Hence, the realization of MLSD for Bluetooth systems involves a complex receiver structure. On the other hand, for practical implementation it is necessary to keep the receiver structure simple and cost effective.

Acquisition of a phase reference for coherent MLSD is also a difficult task as Bluetooth systems allow up to 100 KHz carrier frequency deviation [BTS03]. The permitted variation of the modulation index and the frequency hopping make it even more difficult to estimate the phase reference explicitly. Therefore, in this work, noncoherent sub-optimum sequence detection schemes are investigated for the detection of Bluetooth signals.

The design of the optimal receiver filters which are necessary to obtain a sufficient statistic after sampling, is also dependent on h [ARS81]. Moreover, the operation of Bluetooth in the ISM band makes it vulnerable to interference from other users of Bluetooth, WLANs, and cordless phones, operating in the same frequency band. Therefore, a careful receiver filter design is needed to suppress co-channel and adjacent channel interference as far as possible.

As has been mentioned earlier, the popular receiver for Bluetooth systems uses the LDI detector which offers a very cost effective, structurally simple, and robust solution for

Bluetooth devices. However, the performance of the LDI detector is highly sub-optimum which is verified by the bit error rate (BER) vs. $10\log_{10}(E_s/N_0)$ graph of the LDI detector and optimum coherent MLSD performance shown in Fig. 1.2, where E_s denotes the average symbol energy of the transmitted signal and N_0 is the single-sided power spectral density of the noise. The comparison of the LDI detector and optimum coherent MLSD performance reveals that to achieve a BER of 0.1% the LDI detector requires a 6 dB higher signal power than the optimum receiver. This observation indicates the possibility of a reduction in power consumption by a factor of four, thereby achieving increased throughput or better coverage for Bluetooth systems at the same signal power. Inspite of the aforementioned challenges, the large possible power efficiency gains motivate an investigation of an alternative approach for receiver design for Bluetooth systems.

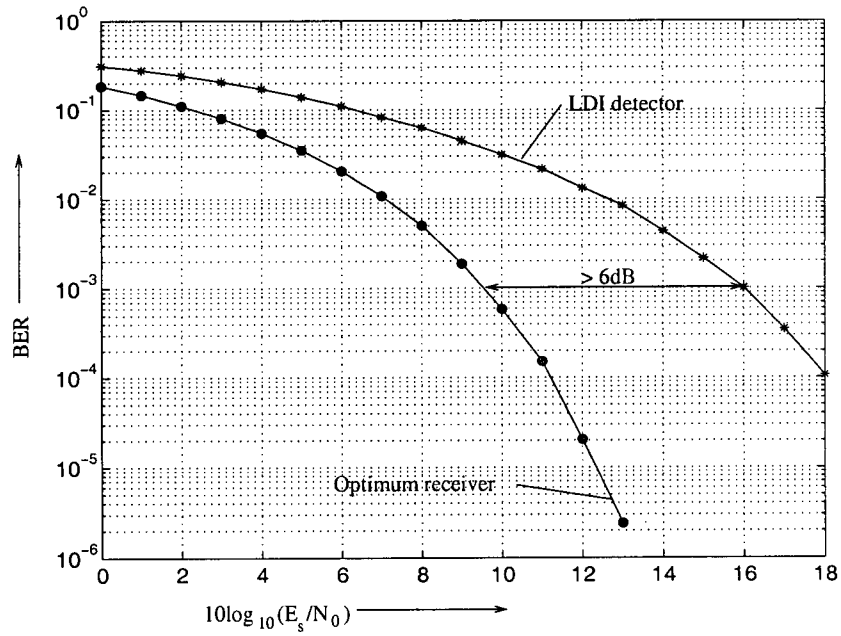

Figure 1.2: Performance comparison of LDI and optimum receiver.

1.3 Contributions

The main contributions of the present research work are as follows:

- A novel receiver design is proposed that shows performance gains of 3 to 5 dB over the conventional LDI detector. The receiver design is based on the Rimoldi/Huber&Liu decomposition of GFSK [Rim88] [HL89] and the concept of non-coherent SD (NSD) [CR99]. A simple receiver structure is obtained consisting of a single filter and a subsequent two-state sequence detector. The reduction to two states for any value of h is achieved using per survivor processing [RPT95] which solves the varying trellis structure problem associated with MLSD.

- A new filter design for the novel receiver is proposed to effectively combat interference.

- A simple frequency estimation method is devised for robustness against high frequency offsets.

- To obtain acceptable performance for all values of h, an adaptive NSD strategy is proposed, which allows for fast adaptation of NSD to the actually used value of h. The proposed strategy offers a low complexity solution to estimate h thereby improving the performance of the detector.

- The capability of the (15,10) expurgated Hamming code to correct double errors, is used to modify the decoder to achieve improvement in the performance of NSD for coded transmission. The conventional LDI receiver also benefits from the modification with negligible added complexity.

1.4 Thesis Organization

The thesis is organized as follows.

In Chapter 2, the required theoretical background for this research work is reviewed. There, the structure of the optimum receiver for GFSK is presented followed by a discussion of the state-of-the-art receivers for Bluetooth systems.

Chapter 3 provides the theory and the structure of the proposed receiver. The decomposition approach given by Rimoldi/Huber&Liu [Rim88][HL89] is discussed. Furthermore, the application of NSD to GFSK and the phase estimation techniques are presented. The frequency estimation technique devised to provide robustness against frequency offsets is also discussed. Subsequently, a filter design is presented that is extremely effective in combating interference. The varying modulation index h affects the receiver performance adversely. Therefore, a simple estimation algorithm for h is devised which significantly improves the performance. Thereafter, the proposed approach to achieve state reduction is presented followed by the modified FEC decoding algorithm.

Chapter 4 discusses the performance of the proposed receiver for different design parameters. A comparison of performance for the available filter designs, phase estimation techniques, and numbers of states directs an appropriate selection of the receiver parameters. The performance of the designed receiver is then evaluated under a set of different channel conditions to test the effectiveness of the proposed h and frequency estimation techniques, along with the modified FEC decoding strategies. A comparison of the performance of the new receiver with that of state-of-the-art receivers is also presented.

Finally, the research work is summarized in Chapter 5, and possible future work is suggested.

Chapter 2

Background and State-of-the-Art

In this chapter, the background information required for the present thesis work is reviewed and the benchmark receivers are introduced. The Bluetooth standard specifies the requirements for a Bluetooth radio and the expected receiver performance [BTS03]. This research work precisely follows the widely accepted Bluetooth radio specifications to develop a simple and power efficient receiver for short range wireless communications. In Section 2.1 of this chapter the Bluetooth system model is described in detail including the modulation scheme and the channel. Section 2.2 discusses optimum detection and disadvantages of the optimum detector. A theoretical lower bound for the receiver performance is also obtained. The subsequent section introduces the popular LDI detector [SV01b], and other state-of-the-art receivers for Bluetooth such as the max-log-maximum-likelihood LDI (MLM-LDI) [SWJ04] and the maximum-a-posteriori probability (MAP) receiver [SHS03].

2.1 Bluetooth System Model

This section outlines the specifications required for the receiver design and presents the system model based on the channel characteristics defined in the Bluetooth standard [BTS03].

2.1.1 GFSK Modulation

As has been mentioned earlier (cf. Section 1.1), Bluetooth employs frequency hopping spread spectrum (FHSS). The implemented modulation scheme is binary partial response Gaussian frequency shift keying (GFSK) which provides a favorable trade-off between power and bandwidth efficiency, and allows for low-complexity transmitter and receiver implementations. GFSK belongs to the family of continuous phase modulation (CPM), which is a non-linear modulation scheme with memory. The high spectral efficiency of CPM is attributed to the following characteristics of the modulated signal:

- The transmitted signal has a constant envelope, i.e., non-linear amplifiers do not cause out-of-band power.
- The phase of the modulated signal is constrained to be continuous which avoids large spectral side-lobes outside of the main spectral band of the signal [Pro01, Ch. 4]. This also introduces memory in the modulated signal.

The modulated CPM signal can be represented as [AAS86]

$$s_{\mathrm{RF}}(t, \boldsymbol{a}) = \frac{\sqrt{2E}}{T} \cos\left(2\pi f_c t + \phi(t, \boldsymbol{a})\right) \tag{2.1}$$

where E denotes the signal energy per modulation interval T, f_c is the carrier frequency, $\boldsymbol{a}$ is the random input stream of binary data bits $a[i]$, $a[i] \in \{\pm 1\}$. $\phi(t, \boldsymbol{a})$ is the information carrying phase, given by

$$\phi(t, \boldsymbol{a}) = 2\pi h \sum_{i=-\infty}^{\infty} a[i] q(t - iT) \tag{2.2}$$

where h is the modulation index and $q(t) = \int_{-\infty}^{t} g(\tau) d\tau$ is the phase pulse. For GFSK, the frequency pulse $g(t)$ is obtained by filtering a rectangular pulse with a Gaussian filter $h(t)$ [LVNKM03], i.e.,

$$g(t) = h(t) * \mathrm{rect}\left(\frac{t}{T}\right)$$

where $*$ denotes convoloution and $h(t)$ is a Gaussian low pass filter given by

$$h(t) = \frac{cB}{\sqrt{2\pi}} \exp\left(-\frac{c^2(Bt)^2}{2}\right)$$

with B as the 3 dB bandwidth of the Gaussian low pass filter, and constant $c = 2\pi/\sqrt{\ln(2)}$. The rectangular pulse is defined as

$$\text{rect}\left(\frac{t}{T}\right) = \begin{cases} 1/T & \text{for } |t| < T/2 \\ 0 & \text{otherwise} \end{cases} . \tag{2.3}$$

Hence, the frequency pulse can be expressed as [LVNKM03]

$$g(t) = \frac{1}{2T}\left[Q(c \cdot B(t - T/2)) - Q(c \cdot B(t + T/2))\right] \tag{2.4}$$

where $Q(t)$ is the standard Gaussian Q function, $Q(t) = 1/\sqrt{2\pi}\int_t^\infty \mathrm{e}^{-\tau^2/2}d\tau$. The phase pulse $q(t)$ is normalized such that it is given by

$$q(t) = \begin{cases} 0 & t < 0 \\ \int_0^t g(\tau)d\tau & 0 \le t < LT \\ 1/2 & t \ge LT \end{cases} , \tag{2.5}$$

where L is the span of frequency pulse $g(t)$. In the Bluetooth standard [BTS03], the time-bandwidth product of $g(t)$ is specified as $BT = 0.5$ with $T = 10^{-6}$ s. Since $q(LT) \simeq 1/2$ is true for $L = 2$ [Pro01, Ch. 4], GFSK can be approximated as a partial response CPM with a truncated frequency pulse of duration $2T$, i.e., $L = 2$. Hence, the data symbol is spread over two symbol durations which introduces additional memory and reduces the spectral occupancy of the modulated signal. Introducing L in Eq. (2.2), the phase deviation in the interval $nT \le t \le (n+1)T$ can be written as

$$\phi(t, \boldsymbol{a}) = 2\pi h \sum_{i=n-L+1}^{n} a[i]q(t - iT) + \pi h \sum_{i=-\infty}^{n-L} a[i]. \tag{2.6}$$

For Bluetooth devices the modulation index h is allowed to vary in the range of 0.28 to 0.35 [BTS03], which is lower than the classical minimum shift keying (MSK) requirement of 0.5. The sub-MSK modulation index affects the system performance adversely [Pro01]. However, this restriction is imposed to satisfy federal communications commission (FCC) section

15.247 rule governing frequency hopping spread spectrum ISM devices [FCC]. Hence, as the modulation index value affects the peak frequency deviation, the maximum frequency deviation is between 140 and 175 KHz. For the design of the sequence detector the modulation index is appropriately quantized such that h can be expressed as a rational number $h = k/p$ with relatively prime integers k and p [Pro01, Ch. 4].

2.1.2 Channel and Interference Model

Bluetooth systems are designed for short range wireless applications. For such applications the root mean square (rms) delay T_d introduced by the time-spreading mechanism of the channel is below 70 ns for indoor radio at 2.4 GHz [ZW99][JSP96][SV01a], which is very low when compared with the symbol duration of 1 μs for Bluetooth systems. Moreover, at high carrier frequencies, the channel is very slowly varying [SV01a] and the Doppler frequency shift can be ignored. This renders the channel frequency non-selective with a static fading gain for the duration of one packet. Furthermore, a line-of-sight (LOS) path is assumed to be available, therefore, the envelope of the faded signal closely follows the Ricean distribution [JNG02]. The Ricean distribution is given by [Rap96]

$$p(g) = \frac{g}{\sigma^2} \mathrm{e}^{\left(-\frac{g^2+P_{\mathrm{los}}}{2\sigma^2}\right)} I_0\left(\frac{g\sqrt{P_{\mathrm{los}}}}{\sigma^2}\right), \qquad g \geq 0, \tag{2.7}$$

where g is the envelope of the channel gain, $2\sigma^2$ is the variance of the multipath , P_{los} is the peak amplitude of the LOS signal, and $I_0(.)$ is the 0^{th} order Bessel modified function of the first kind. The average channel power gain is assumed to be one, i.e., $P_{\mathrm{los}} + 2\sigma^2 = 1$. The ratio $P_{\mathrm{los}}/2\sigma^2$ is defined as the Ricean factor K. Rayleigh fading is obtained as a special case for $P_{\mathrm{los}} \rightarrow 0$ and the static AWGN channel results for $\sigma^2 \rightarrow 0$. The equivalent complex baseband (ECB) received signal in a slow fading channel can be expressed as

$$r(t) = g\mathrm{e}^{j\phi_0} \cdot s(t, \boldsymbol{a}) + n(t), \qquad 0 \leq t \leq T_p, \tag{2.8}$$

where g is constant over one packet length T_p and is independent from packet to packet. $s(t, \boldsymbol{a})$ is the ECB transmit signal, $n(t)$ is complex-baseband AWGN and ϕ_0 is the time-invariant phase introduced due to fading. $s(t, \boldsymbol{a})$ is related to the pass-band signal $s_{\mathrm{RF}}(t, \boldsymbol{a})$ by $s_{\mathrm{RF}}(t, \boldsymbol{a}) = \Re\{s(t, \boldsymbol{a})e^{j2\pi f_c t}\}$ where $\Re\{x\}$ denotes real part of the complex number x.

The Bluetooth specifications allow a ± 100 kHz frequency offset between transmitter and receiver oscillator, which is fairly relaxed compared to the 1 MHz bandwidth of the signal. This undesirable high frequency offset Δf deteriorates the receiver performance to a great extent as shown in the performance results in Chapter 4. Besides introducing frequency offset, the receiver oscillator also introduces phase jitter, $\Delta\phi_c(t, \tau)$. For a given t and τ, $\Delta\phi_c(t, \tau)$ can be modelled as a white Gaussian process with variance $\sigma_\Delta^2(\tau) = (2\pi f_c)^2 k\tau$, where k is a constant depending on the employed oscillator [DMR00]. The variance increases linearly with time. The time varying phase introduced by the channel can be expressed as

$$\phi_c(t + \tau) = \phi_c(t) + 2\pi\Delta f\tau + \Delta\phi_c(t, \tau). \tag{2.9}$$

The received signal in the presence of phase noise and frequency offset becomes

$$r(t) = ge^{j(\phi_c(t)+\phi_0)}s(t, \boldsymbol{a}) + n(t), \qquad 0 \leq t \leq T_p. \tag{2.10}$$

As Bluetooth operates in the license-free ISM band, there is no control over the usage of the band. Therefore, other piconets operating independently in the vicinity may cause undesirable interference. The Bluetooth standard specifies the co-channel and adjacent channel interference performance of the receiver [BTS03]. Apart from other Bluetooth devices, interference may also be caused by other users of the ISM band e.g. WLANs. In the present work, only the effect of interference from other Bluetooth piconets, synchronized to the packet boundaries, is considered. The signal-to-interferer power ratio (CIR) for an interferer at $f_c + \Delta f_{c,i}$, where $\Delta f_{c,i}$ is the frequency offset of interferer compared to the desired signal, is given in Table 2.1. Taking into account this unwanted interference $i(t)$,

the Bluetooth ECB system model can be mathematically expressed as

$$r(t) = ge^{j(\phi_c(t)+\phi_0)}s(t,\boldsymbol{a}) + i(t) + n(t), \qquad 0 \leq t \leq T_p. \tag{2.11}$$

Table 2.1: Interference performance [BTS03].

Type of Interference	$\Delta f_{c,i}$	CIR
Co–channel interference	0 MHz	11 dB
Adjacent channel (1 MHz) interference	1 MHz	0 dB
Adjacent channel (2 MHz) interference	2 MHz	–30 dB
Adjacent channel (⩾3 MHz) interference	3 MHz	–40 dB

To summarize, the Bluetooth ECB system model can be graphically represented by the block diagram shown in Fig. 2.1, where $\hat{a}[i]$ is the signal estimated by the receiver. Though the channel is the same for the desired signal and the interferer, the Ricean distributed fading gain g' and phase shift ϕ_0' observed by the interfering signal may be different from that of the desired signal as the paths between the transmitter and receiver may not be the same for the two.

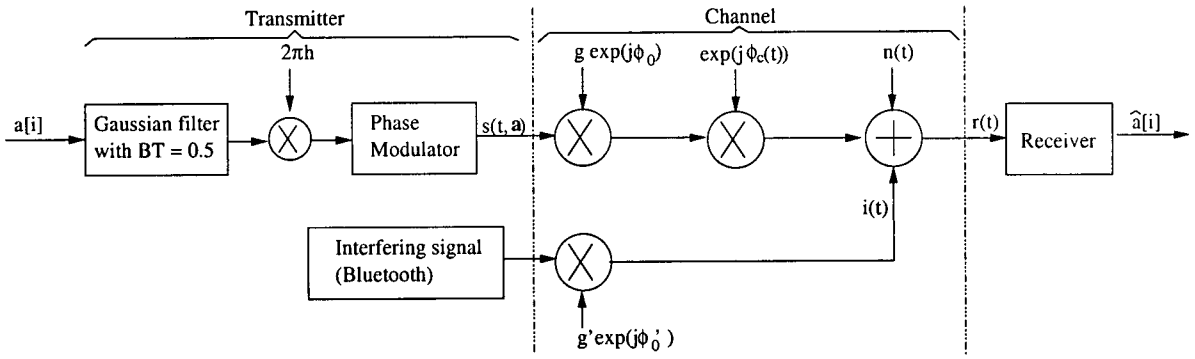

Figure 2.1: Bluetooth baseband system model.

2.1.3 Error Correction

The Bluetooth specifications define different packet types depending upon the application and its requirements of quality and data rate. For error free reception of the packets three error correction schemes are defined, which are described as follows:

1. An automatic repeat request (ARQ) scheme is defined to acknowledge the correct reception of the payload of a packet. A cyclic redundancy check (CRC) code is added to the packet to determine if the received packet is error free or not. If the packet is not correctly received, it is retransmitted until it is received correctly. ARQ is used for payload protection of all the data packets and the special control packet for frequency hop synchronization (FHS).

2. A simple 1/3 rate FEC scheme is defined for the protection of header and high quality voice (HV1) packets. Each bit is repeated three times to implement this repetition code. Though the overhead is high, it provides better reliability as compared to uncoded or (15,10) Hamming coded transmission. Therefore, the header is always 1/3 rate FEC protected as it carries important link information. Since it is undesirable to retransmitted the voice packets, HV1 packets are also repetition coded to maintain good quality for the voice traffic.

3. A 2/3 rate (15,10) expurgated[1] Hamming code, is defined to protect medium rate data packets (DM1, DM3, DM5), data voice (DV) packets, the voice packet type HV2, and the FHS control packets. This code is used to correct single errors [BTS03] in a codeword of 15 bits. Five parity bits are appended to a block of 10 information bits. The calculation of parity bits is as follows: if 10 binary data symbols are represented by $\boldsymbol{m} = [m_0, m_1, ..., m_9]$ and associated with the message polynomial

[1] In the specifications, the (15,10) Hamming code is referred to as 'shortened' Hamming code.

$m(x) = m_0 + m_1 x + ... m_9 x^9$, then the parity bits are given by the remainder obtained from dividing $m(x)x^5$ by the generator polynomial $g(x) = 1 + x^2 + x^4 + x^5$ [BTS03].

2.2 Optimum Receiver

In this section, the structure of an optimum receiver for GFSK in a pure AWGN channel is discussed. Considering the inherent memory in CPM signals an optimum detector takes decisions based on the sequence of received signals, minimizing the probability of error. The interdependence of successive symbols can be represented by a trellis diagram, the minimum Euclidean distance path through which gives the maximum-likelihood sequence [Pro01, Ch. 5]. As mentioned in Section 2.1.1, the phase of the GFSK modulated signal, for $L = 2$ can be rewritten as (cf. Eq. (2.6))

$$\phi(t, \boldsymbol{a}) = 2\pi h \sum_{i=n-1}^{n} a[i]q(t - iT) + \pi h \sum_{i=-\infty}^{n-2} a[i], \tag{2.12}$$

where $nT \leq t \leq (n+1)T$. In the time interval $nT \leq t \leq (n+1)T$, the phase deviation of the modulated signal is dependent on (a) the current symbol and the previous $(L-1)$ input symbols represented by the first term in Eq. (2.12) and (b) the accumulated phase till time $(n-L)T$, represented by the second term. The phase transitions are controlled by the current symbol and the $(L-1)$ last symbols only, as the phase pulse $q(t)$ is constant for $t \geq LT$ (cf. Eq. (2.5)). Hence, the vector $(\theta[n-L], a[n-L+1], ..., a[n-1], a[n])$ uniquely specifies the signal element during n^{th} interval, where $\theta[n-L]$ represents the accumulated phase referred to as phase state. Since the phase is unique only in the interval from 0 to 2π, the phase state can be defined as [Liu90]

$$\theta[n-L] = \left[\pi h \sum_{i=-\infty}^{n-L} a[i]\right] \text{mod}(2\pi) = \frac{\pi}{p}\left[k \sum_{i=-\infty}^{n-L} a[i]\right] \text{mod}(2p) \tag{2.13}$$

For even k, there are p phase states and $\theta[n-L]$ belongs to

$$\left\{0, \frac{\pi k}{p}, \frac{2\pi k}{p}, ..., \frac{(p-1)\pi k}{p}\right\},$$

and for odd k, there are $2p$ phase states which belong to the set

$$\left\{0, \frac{\pi k}{p}, \frac{2\pi k}{p}, ..., \frac{(2p-1)\pi k}{p}\right\}.$$

For odd k, the term in the bracket in Eq. (2.13) is alternating between even and odd resulting in twice the number of phase states compared to even k. This alternation between even and odd phase states for an odd k introduces time variance in the trellis as the possible set of attainable states in one time interval of duration T differs from the next time interval. Nevertheless, the number of attainable states per time interval is equal to p. This is shown in the phase state trellis diagram in Fig. 2.2 which is drawn for binary GFSK with $h = 1/3$ and $L = 2$.

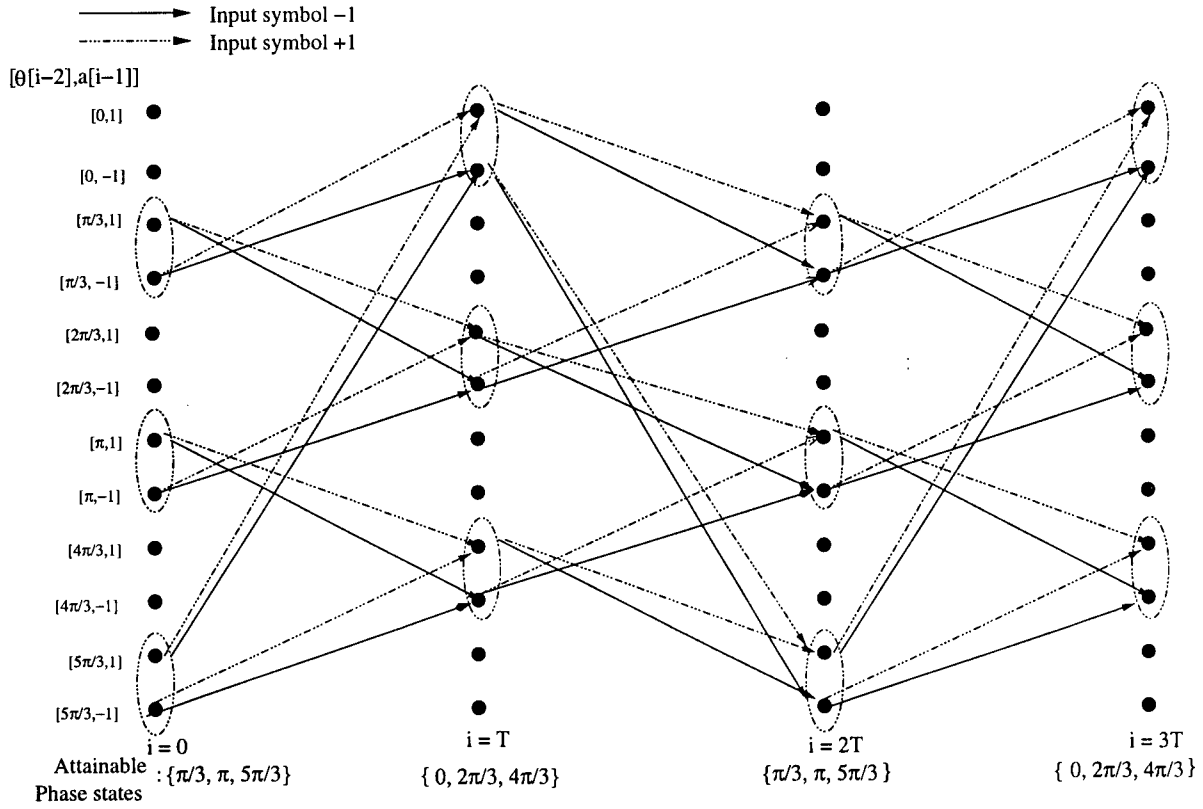

Figure 2.2: Time-variant trellis of phase state for $h = 1/3$, $M = 2$, and $L = 2$.

Thus, GFSK can be represented as a finite state time-variant Markov process with pM^{L-1} (or $2pM^{L-1}$) states and the state vector $\boldsymbol{S}_n = [\theta[n-L], a[n-L+1], ...a[n-1]]$.

For binary GFSK with $L = 2$, the state vector $\boldsymbol{S}_n$ becomes $[\theta[n-2], a[n-1]]$. The number of possible states is $2p$ for even k and $4p$ for odd k. The state vector at $t = (n+1)T$ is obtained as

$$\boldsymbol{S}_{n+1} = [\theta[n-1], a[n]] \tag{2.14}$$

where

$$\theta[n-1] = \theta[n-2] + \pi h a[n-1]. \tag{2.15}$$

For optimum demodulation of GFSK, the Viterbi algorithm (VA) is an efficient method to perform MLSD [ARS81] which takes decisions based on the best path metrics of the survivor paths. The path metric is the sum of the branch metric and the corresponding survivor path metric for each branch. The preliminary decision is taken in favor of that path metric which maximizes the log-likelihood function. The log-likelihood function is proportional to the cross correlation metric [Pro01, Ch. 5]

$$CM_n(\tilde{\boldsymbol{a}}) = \int_{-\infty}^{(n+1)T} \Re\{r(t)\mathrm{e}^{-j\phi(t,\tilde{\boldsymbol{a}})}\}dt \tag{2.16}$$

$$= CM_{n-1}(\tilde{\boldsymbol{a}}) + \int_{nT}^{(n+1)T} \Re\{r(t)\mathrm{e}^{-j\phi(t,\tilde{\boldsymbol{a}})}\}dt \tag{2.17}$$

where $CM_n(\tilde{\boldsymbol{a}})$ represents the path metric up to time nT for the surviving sequences, $\tilde{\boldsymbol{a}}$ are the possible hypothetical sequences, $r(t)$ is the received signal, $r(t) = s(t, \boldsymbol{a}) + n(t)$. For each state there is one survivor path and M possible branches. Therefore, the number of possible branches or hypothetical sequences per symbol interval is pM^L (or $2pM^L$). Hence, in each symbol interval there are pM^L (or $2pM^L$) cross correlation values to be calculated.

To obtain the cross-correlation metric using a basic quadrature receiver the number of matched baseband filters required is $2M^L$ with the impulse response [ARS81]

$$h_c(t, \tilde{\boldsymbol{a}}) = \begin{cases} \cos\left[2\pi h \sum_{i=-L+1}^{0} \tilde{a}[i] q((1-i)T - t)\right] \\ 0 \quad \text{for } t \text{ outside } [0, T], \end{cases} \tag{2.18}$$

and

$$h_s(t,\tilde{\boldsymbol{a}}) = \begin{cases} \sin\left[2\pi h \sum_{i=-L+1}^{0} \tilde{a}[i] q((1-i)T - t)\right] \\ 0 \quad \text{for } t \text{ outside } [0,T]. \end{cases} \tag{2.19}$$

Thus, the optimum receiver consists of a bank of matched filters $h_c(t,\tilde{\boldsymbol{a}})$ and $h_s(t,\tilde{\boldsymbol{a}})$ followed by an MLSD processor.

From the aforementioned discussion, it may be observed that the complexity of an optimum receiver increases exponentially with M and L. Also, the modulation index h is an important parameter that influences the trellis structure, the number of phase states, and the filter design. The variable h for Bluetooth systems complicates the optimum receiver design to a great extent. For $h = 1/3$, there are 12 possible states, therefore 24 computations per symbol interval have to be performed. For $h = 0.29 = 29/100$, there are 400 states and 800 computations, that are required to be performed in each symbol interval. Such a high number of computations increases the cost and compromises the robustness of the receiver, thereby, defeating the purpose of the design.

2.2.1 Optimum Receiver in the Presence of Random Phase in the Channel

In the discussion so far, the channel is assumed to be a pure AWGN, hence no phase distortion is introduced by the channel. But for practical Blutooth devices, a random time-variant phase distortion $\phi_c(t)$ may be introduced in the received signal as described in Section 2.1.2. For an optimum coherent receiver, the phase $\phi_c(t)$ has to be estimated explicitly, e.g. by introducing known pilot symbols into the transmitted signal stream and using a phase-locked loop [Pro01, Ch.6], at the expense of increased complexity.

For optimum NSD with the assumption of a constant phase rotation ϕ_0, the received signal $r(t)$ is expressed as $r(t) = s(t,\boldsymbol{a})e^{j\phi_0} + n(t)$. The phase distortion ϕ_0 is modeled as random variable with uniform distribution in the interval $[0, 2\pi)$ [CR99]. The decoding

strategy for optimum NSD for any modulation format is expressed as [CR99]

$$\hat{\boldsymbol{a}} = \arg\max_{\tilde{\boldsymbol{a}}} \left\{ -\frac{1}{2N_0} \int_{T_0} |s(t,\tilde{\boldsymbol{a}})|^2 dt + \log I_0 \left(\frac{1}{N_0} \left| \int_{T_0} r(t) s^*(t,\tilde{\boldsymbol{a}}) dt \right| \right) \right\} \tag{2.20}$$

where $\hat{\boldsymbol{a}}$ is the detected sequence, $\tilde{\boldsymbol{a}}$ is a hypothetical information sequence, and T_0 is the observation interval. As the observation interval T_0 increases linearly with time, the lengths of the transmitted sequence and the hypothetical sequence increase causing an exponential increase in the receiver complexity with time. Thus, the channel phase introduces infinite memory in the transmitted signal rendering the realization of a simple receiver based on optimum NSD infeasible.

2.2.2 Lower Bound for Performance of MLSD

It is desirable to establish a theoretical bound for the best achievable performance of MLSD. For large average signal bit energy to noise ratios (SNRs), the probability of a bit error of coherent MLSD in an AWGN channel is given by [AAS86, Ch. 3]

$$P_e \sim Q\left(\sqrt{\frac{d_{\min}^2}{R_c} \frac{E_s}{N_0}} \right) \tag{2.21}$$

where $d_{\min}$ is the minimum normalized Euclidean distance between two possible sequences of symbols $a[i]$ and R_c denotes the code rate.

The Euclidean distance between two sequences $\boldsymbol{a}_{1,N}$ and $\boldsymbol{a}_{2,N}$ of length N for constant envelop signals depends on the phases of the two signals, and hence, depends on h [AAS86, Ch. 3]. The squared Euclidean distance between $\boldsymbol{a}_{1,N}$ and $\boldsymbol{a}_{2,N}$ can be written as [AS81]

$$D^2(\boldsymbol{a}_{1,N}, \boldsymbol{a}_{2,N}) = \int_0^{NT} |s(t,\boldsymbol{a}_{1,N}) - s(t,\boldsymbol{a}_{2,N})|^2 dt, \tag{2.22}$$

which results in the following expression for the minimum Euclidean distance normalized by average bit energy E_b [AS81]

$$d_{\min,N}^2 = \log_2(M) \cdot \min_{\boldsymbol{\gamma}_N} \left\{ N - \frac{1}{T} \int_0^{NT} \cos[\phi(t,\boldsymbol{\gamma}_N)] dt \right\}. \tag{2.23}$$

Here $\phi(t, \boldsymbol{\gamma}_N) = 2\pi h \sum_{i=0}^{\infty} \gamma[i] q(t - iT)$ (Eq. (2.2)) with $\boldsymbol{\gamma}_N$ defined as the difference of the two sequences, i.e., $\boldsymbol{\gamma}_N = \boldsymbol{a}_{1,N}$ - $\boldsymbol{a}_{2,N}$ (cf. [AS81]). The Euclidean distance increment over each symbol interval is nonnegative. Therefore, the Euclidean distance is a nondecreasing function of the length of the observation interval N. An upper bound for the minimum distance may be obtained as a function of h for any N by considering the infinitely long sequence pair that merges the earliest for any h. Two sequences are said to have merged at a certain time if their phases coincide for all subsequent time intervals. Therefore, for establishing the performance bounds for a particular h for different cases of coded and uncoded transmission, first the sequence pair of infinite length that merges the earliest is found. Then, using the difference sequence of the pair an upper bound for minimum Euclidean distance is obtained as in Eq. (2.23). If the pair merges after N_B observation intervals, then the upper bound becomes

$$d^2_{\min}(h) = \log_2(M) \left\{ N_B - \frac{1}{T} \int_0^{N_B T} \cos[\phi(t, \boldsymbol{\gamma}_{N_B})] dt \right\}. \tag{2.24}$$

Here, the notation $d^2_{\min}(h)$ is used to indicate the dependence of the minimum Euclidean distance on h. Replacing $d_{\min}$ in Eq. (2.21) by the upper bound $d_{\min}(h)$ of the minimum distance where $d_{\min} \leq d_{\min}(h)$, the probability of error as a function of h becomes

$$P_e \geq Q\left(\sqrt{\frac{d^2_{\min}(h)}{R_c} \frac{E_s}{N_0}} \right) \tag{2.25}$$

As $Q(x)$ is a decreasing function of x, a lower performance bound of MLSD is achieved which is a lower performance bound for NSD too. Therefore, BER is dependent on the normalized squared Euclidean distance $d^2_{\min}(h)$ which allows for a quantitative comparison of different coding and decoding schemes. For reference, $d^2_{\min}$ for binary phase shift keying (BPSK) is 2 units which means the minimum difference in the energies of the two BPSK modulated sequences is $2E_b$ [AS81].

2.3 Benchmark Receivers for Bluetooth

Since the idea of Bluetooth system originated in 1998, many researchers have been working on the development of low complexity, robust, and power efficient receivers [PYPJC01][HL01] [SJ03b][SWJ04][SHS03]. The popular receiver used in Bluetooth devices is the limiter-discriminator with integrate and dump filter [SV01a], which is a simple-to-implement, low cost, and robust noncoherent receiver. However, the LDI receiver is very power inefficient compared to the optimum receiver, as shown in Fig. 1.2. To improve the performance of the LDI receiver, several techniques have been devised such as channel estimation [PYPJC01], fractionally-spaced differential detection [HL01], and least squares based post-integration filtering [SJ03a]. To simplify the receiver structure, modified zero-crossing demodulation of intermediate frequency (IF) signals has also been proposed [SJ03b]. However, the performance gain achieved by these schemes over the conventional LDI receiver, at the target BER of 10^{-3}, is in the range of 0.5 to 1 dB [SJ03b][SWJ04], which is not substantial. Recently, Scholand et al. proposed a receiver referred to as max-log-maximum-likelihood LDI (MLM-LDI) [SWJ04], which achieves significant performance gains over the conventional LDI detector but at the cost of increased complexity. Another receiver which achieves close-to-optimum performance is the maximum-a-posteriori probability (MAP) receiver, proposed by Schiphorst et al. [SHS03]. This receiver is based on Laurent's decomposition of GFSK. The MAP receiver has a similar performance as coherent MLSD and achieves close to 6 dB gain in performance as compared to the LDI detector, however, it requires an exact knowledge of the channel phase and the modulation index.

In the following section the concepts of the LDI detector and the MLM-LDI detector are briefly introduced.

2.3.1 LDI Detector

The classic LDI receiver consists of a limiter-discriminator for data demodulation, followed by an integrate and dump (I&D) post-detection filter. The block diagram of the LDI detector is shown in Fig. 2.3.

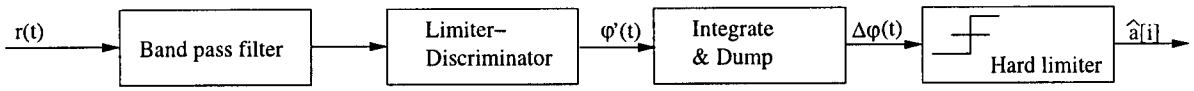

Figure 2.3: Block diagram for LDI receiver.

A pre-detection band-pass Gaussian filter is applied, with equivalent low pass impulse response

$$h_r(t) = \sqrt{\frac{2\pi}{\ln 2}} B_r \mathrm{e}^{-\left(\frac{2\pi^2}{\ln 2}\right)(B_r t)^2}, \tag{2.26}$$

where B_r is the 3 dB bandwidth of the filter. The optimum bandwidth of the filter is given by $B_r = 1.1/(2T)$ [SV01a]. The limiter-discriminator outputs the derivative of the filtered signal phase $\varphi(t)$ [Paw81]. The I&D filter is a rectangular filter of duration T and amplitude one. The I&D filter re-integrates the derivative over one symbol duration giving a phase difference which is the net increment or decrement in the phase over a symbol duration [Paw81]. The decision is taken at each interval T after sampling at the maximum eye opening instant [SV01a]. The hard limiter compares the sampled data with the set decision level which is zero for binary GFSK. If the phase difference is greater than zero, which means increasing phase of the received signal, the decision is taken in favor of +1. To get the results in various scenarios like varying h and interference, the LDI receiver has been simulated in the present research work.

2.3.2 MLM-LDI Detector

The MLM-LDI detector employs a max-log-maximum likelihood (MLM) symbol estimation post processor followed by a least-squares based post-integration filter to the output of a

digital LDI [SWJ04][SJ03b]. The MLM involves a forward-backward (FB) algorithm on a four state trellis [KB90]. This post-processor improves the performance by approximately 3.5 dB, but an increased design complexity is introduced because of the post processing and the four state trellis involved in MLM. For comparison purposes in the present research work, the results presented in [SWJ04, Figure 1] have been used.

Chapter 3

Noncoherent Sequence Detection Receiver for Bluetooth

In this chapter, the proposed receiver design for Bluetooth devices is presented. As discussed in the previous chapter, the Bluetooth receiver is desired to be cost-effective and power-efficient, at the same time meeting the Bluetooth radio specifications [BTS03]. The most challenging problem in the design of the receiver is to ensure good performance with a low-complexity receiver under the high permissible frequency offset and the varying modulation index. For a simple yet power efficient receiver design, the Rimoldi/Huber&Liu representation of CPM [Rim88][HL89] has been adopted as shall be explained in Section 3.1. In Section 3.2, a new receiver filter design is proposed which ensures good performance in the presence of interference. The novel receiver employs noncoherent sequence detection (NSD) where the phase is implicitly estimated. Methods for implicit phase and frequency offset estimation for NSD are described in Section 3.3. The variable modulation index results in a trellis with a variable number of states (cf. Section 2.2), consequently increasing the receiver complexity. This problem is solved by reducing the number of states to two as discussed in Section 3.4. Besides the complexity of the receiver, a deviation in h from its true value also affects the receiver performance adversely. To tackle this problem a

simple h estimation scheme is presented in Section 3.5. In Section 3.6, channel coding and techniques to improve the decoding performance are discussed. Finally, the receiver design is summarized in the concluding section of this chapter.

3.1 Rimoldi/Huber&Liu Representation of GFSK

The high complexity of the optimum CPM receivers due to the inherent memory of CPM motivated the search for reduced complexity receivers. Laurent (1986) [Lau86] proposed an alternative representation of CPM where CPM is represented as a superposition of finite amplitude modulated pulses. This results in significant complexity reduction because for modulations with good spectral characteristics, the representation with only one pulse achieves high accuracy. However, for noncoherent sequence detection an additional whitening filter is necessary [CR98]. Laurent's approach to represent CPM has been applied to Bluetooth receivers in [SHS03], but the varying modulation index problem has not been addressed in the receiver design. An alternative representation of CPM, addressed as the decomposition approach in the present work, was proposed independently by Rimoldi (1988) [Rim88] and Huber and Liu (1989) [HL89]. The decomposition approach shows that CPM can be represented as a linear time-invariant trellis encoder with memory and a time-invariant memoryless signal mapper. This results in the decoupling of filter design and trellis search. Complexity reduction is also achieved as four or six signal elements are sufficient to represent all signal elements of CPM with $M \leq 4$ while maintaining good accuracy [HL89]. In the present work, the decomposition approach given by Rimoldi/Huber&Liu has been adopted. The following section discusses the decomposition approach in brief.

3.1.1 The Decomposition Approach to CPM

In Section 2.2, it was shown that CPM has a time-variant phase state trellis. In the decomposition approach, first the time-variant phase state trellis is transformed into a time-invariant phase state trellis, thereby enabling the decomposition of nonlinear CPM with memory into a simple trellis encoder and a signal mapper.

To achieve a time-invariant trellis, a slope function is introduced which is defined as [HL89]

$$c(t) = \begin{cases} 0 & t < 0 \\ \frac{M-1}{2LT}t & 0 \leq t < LT \\ \frac{M-1}{2} & t \geq LT \end{cases} \tag{3.1}$$

Adding a zero term to the phase of the CPM modulated signal $s_{\mathrm{RF}}(t, \boldsymbol{a})$ (Eq. (2.1)), the phase of the modulated signal can be written as

$$\Phi(t, \boldsymbol{a}) = 2\pi f_c t - 2\pi h \sum_{i=-\infty}^{n} c(t - iT) + \phi(t, \boldsymbol{a}) + 2\pi h \sum_{i=-\infty}^{n} c(t - iT). \tag{3.2}$$

For convenience, a new reference frequency f_r is defined as

$$f_r = f_c - h\frac{M-1}{2T} \tag{3.3}$$

and a modified unipolar information symbol $b[i]$ is introduced that is given by

$$b[i] = \frac{a[i] + M - 1}{2} \quad \in \{0, 1, ...M-1\}. \tag{3.4}$$

With the new variables f_r and $b[i]$, the phase in Eq. (3.2) can be rewritten as [HL89]

$$\Phi(t, \boldsymbol{b}) = 2\pi f_r t + \varphi_{0r} + \frac{2\pi}{p}\Psi[n-L] + 2\pi h \sum_{i=n-L+1}^{n} p(t - iT, b[i]), \tag{3.5}$$

where $\boldsymbol{b}$ is the vector $[b[0], b[1]..., b[n]]$, φ_{0r} is the initial phase and $\Psi[n-L]$ is the normalized modified phase state. The phase transition function $p(t, b[i])$ is defined as

$$p(t, b[i]) = (2b[i] - (M-1))q(t) + c(t). \tag{3.6}$$

The new modified information carrying phase becomes

$$\psi(t, \boldsymbol{b}) = \frac{2\pi}{p}\Psi[n-L] + 2\pi h \sum_{i=n-L+1}^{n} p(t - iT, b[i]) \tag{3.7}$$

with modified normalized phase state definition as

$$\Psi[n-L] = \left[k \sum_{i=-\infty}^{n-L} b[i] \right] \bmod(p) \in \{0, 1, ..., p-1\}. \tag{3.8}$$

The phase state is updated recursively as

$$\Psi[n-L+1] = (\Psi[n-L] + k \cdot b[n-L+1]) \bmod(p). \tag{3.9}$$

Hence, the number of modified phase states is equal to p for any k with respect to the new reference frequency, achieving the desired time-invariance in the phase trellis as shown in Fig. 3.1. Comparison of Fig. 2.2 with Fig. 3.1, which has been drawn for the same h ($h = 1/3$), reveals that the trajectories in the modified trellis are the same for any time interval unlike the original trellis of Fig. 2.2.

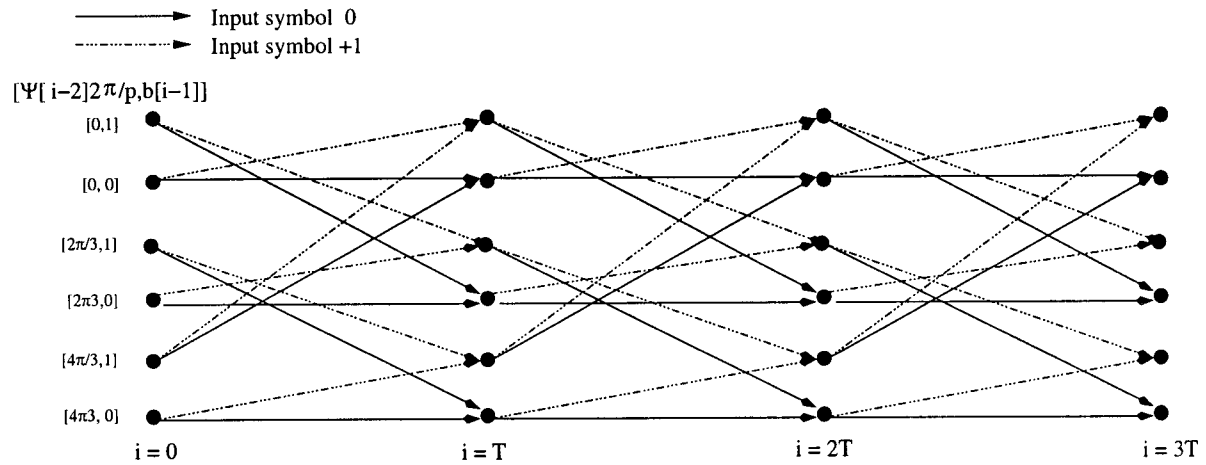

Figure 3.1: Time-invariant trellis of phase state for $h = 1/3$, $M = 2$, and $L = 2$.

There are pM^{L-1} possible states with M branches each, resulting in pM^L possible trajectories in each time interval. Hence, there are pM^L different modulated signals of

duration T which are referred to as the signal elements $\rho(t, \boldsymbol{d}[i])$. $\boldsymbol{d}[i]$ is a unique address vector associated with each signal element,

$$\boldsymbol{d}[n] = [\Psi[n-L], b[n-L+1], ..., b[n-1], b[n]]. \tag{3.10}$$

Therefore, the CPM modulator can be decomposed into a trellis encoder which generates the unique address vector based on the recursively updated phase state and previous L data inputs, and a signal mapper which maps the encoded address to a signal element representing the modulated signal. Hence, the transmitted ECB signal can be represented as a sequence of time-limited signal elements $\rho(t, \boldsymbol{d}[i])$

$$s(t, \boldsymbol{d}) = \sum_{i=0}^{\infty} \rho(t - iT, \boldsymbol{d}[i]). \tag{3.11}$$

Here $\boldsymbol{d}$ represents the sequence of associated addresses, i.e., $\boldsymbol{d} = [\boldsymbol{d}[0], \boldsymbol{d}[1], ..., \boldsymbol{d}[n]]$.

The decomposed equivalent CPM modulator is shown in Fig. 3.2. The intersymbol-interference (ISI) memory due to the previous $(L-1)$ symbols is represented by $(L-1)$ shift registers. The phase memory is recursively updated using a simple phase integrator as shown in the Fig. 3.2. The signal mapper stores a table of pM^L signal elements for the exact representation of CPM.

Having represented CPM as a simple combination of a trellis encoder and a signal mapper, the corresponding reduced complexity receiver structure is presented in the following section.

3.1.2 Receiver Structure

The optimum receiver requires a bank of $2M^L$ matched filters [AAS86] for detecting the received signal. However, it has been shown that the required number of complex filters D to obtain sufficient statistics of the received signal is given by $2D = \min(2D_{max}, 2M^L)$

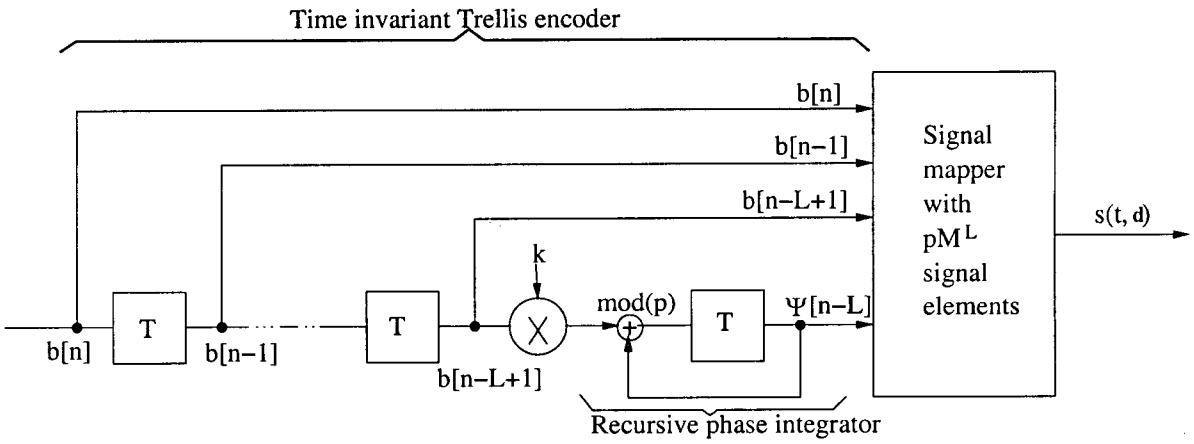

Figure 3.2: Equivalent representation of CPM modulator using decomposition approach.

[HL89], where D_{max} is given by

$$2D_{max} = 2\lceil 1.11h(M-1) + 2.22 \rceil. \tag{3.12}$$

The factor of 2 present in Eq. (3.12) is because of complex baseband signal elements. The dimension D is the number of baseband time-limited functions which represent the signal space formed by the modulated signal with sufficient accuracy. Hence, for Bluetooth systems, with a maximum $h = 0.35$, the dimension D of the matched filter bank reduces to three. To find a proper set of basis functions with dimension D, which spans the whole bandwidth of all the pM^L signal elements $\rho(t, \boldsymbol{d}[i])$, Huber and Liu [HL89] proposed a simple set of D pairs of sine and cosine passband functions of duration T. The proposed basis functions are a set of non-orthogonal exponential functions which are symmetrical to the carrier frequency and equally spaced on the frequency axis. The receiver low-pass filters with respect to the carrier frequency f_c are given by [HL89]:

$$h_D^{(d)}(t) = \frac{1}{T} e^{j2\pi f_d t}, \qquad \frac{-T}{2} \leq t \leq \frac{T}{2} \tag{3.13}$$

with frequencies given by

$$f_d = \frac{\Delta f_d}{2}(2d - 1 - D), \qquad d \in \{1, 2, ..., D\}. \tag{3.14}$$

Δf_{d} is the frequency spacing between the basis function frequencies, $0 \leq \Delta f_{\mathrm{d}} T \leq 1$. It has been shown that the performance degrades negligibly for $0.5 \leq \Delta f_{\mathrm{d}} T \leq 0.7$ with $0.25 \leq h \leq 0.5$ for $D = 3$ and $D = 2$ [Liu90, Fig. 5.4] [HL89, Fig. 6]. Moreover, in Section 3.2 it shall be shown that $D = 1$ can be used for the proposed receiver for which $f_d = 0$. Hence, in the present work it has not been attempted to optimize Δf_{d}. Therefore, $\Delta f_{\mathrm{d}} T = 0.5$ has been used for $D > 1$ in all the simulation work.

The matched filter bank necessary for demodulation is specified by a vector of D coordinates $\boldsymbol{h}_D(t) = [h_D^{(1)}(t), ...h_D^{(D)}(t)]$. The D samples of the filtered received signal in the n^{th} time interval are given by

$$\boldsymbol{x}[n] = r(t) * \boldsymbol{h}_D^*(-t)|_{t=nT} = [x_1[n], ..., x_D[n]] \tag{3.15}$$

where $\boldsymbol{h}_D^*(-t)$ represents complex conjugate of matrix $\boldsymbol{h}_D(-t)$. $[x_1[n], ..., x_D[n]]$ are the sufficient statistic to estimate the input information sequence $\boldsymbol{a}$ using a Viterbi processor. The Viterbi processor stores D values for each signal element $\boldsymbol{\rho}(\tilde{\boldsymbol{d}}[i]) = [\rho_1(\tilde{\boldsymbol{d}}[i]), ..., \rho_D(\tilde{\boldsymbol{d}}[i])]$, which are obtained by multiplying the correlation of D basis functions with signal elements $\rho(t, \tilde{\boldsymbol{d}}[i])$ corresponding to pM^L hypothetical sequences with address vector $\tilde{\boldsymbol{d}}[i]$, and a matrix $\boldsymbol{C}^{-1}$ [Liu90],

$$\boldsymbol{\rho}(\tilde{\boldsymbol{d}}[i]) = \int_0^T \rho(t, \tilde{\boldsymbol{d}}[i]) \boldsymbol{h}_D^*(t) dt \cdot \boldsymbol{C}^{-1}. \tag{3.16}$$

The matrix $\boldsymbol{C}$ is a D-by-D array of cross-correlations of basis functions, introduced to take into account the effect of non-orthogonal basis functions $\boldsymbol{h}_D(t)$. It is given by

$$\boldsymbol{C} = \frac{1}{T} \int_0^T \boldsymbol{h}_D^T(t) \boldsymbol{h}_D^*(t) dt, \tag{3.17}$$

where $\boldsymbol{h}_D^T(t)$ represents transpose of matrix $\boldsymbol{h}_D(t)$.

For coherent detection the Viterbi processor cross-correlates the received sample $x_d[i]$ with $\rho_d(\tilde{\boldsymbol{d}}[i])$ for all hypothetical sequences to get the branch metric

$$\lambda[i] = \Re\{\boldsymbol{x}[i] \cdot \boldsymbol{\rho}^H(\tilde{\boldsymbol{d}}[i])\}, \tag{3.18}$$

where $\boldsymbol{\rho}^H(\tilde{\boldsymbol{d}}[i])$ represents Hermitian transposition of matrix $\boldsymbol{\rho}(\tilde{\boldsymbol{d}}[i])$. A survivor path traces the estimated symbol in each time interval for every state. The calculated branch metric is added to the corresponding survivor path to get the path metric of that branch. For each state the decision is taken in favor of the branch with maximum path metric. The corresponding symbol is added to the relevant survivor path and the path metric of the survivor path is updated. The estimated sequence is the survivor path with maximum path metric among all the states. The number of states in the Viterbi processor is pM^{L-1} using the decomposition approach, which is only half the number of states required for an odd value of k if the conventional representation of CPM is used. It is worth observing that the number of states in the Viterbi processor is independent of the filters preceding it. The modified receiver structure is shown in Fig. 3.3.

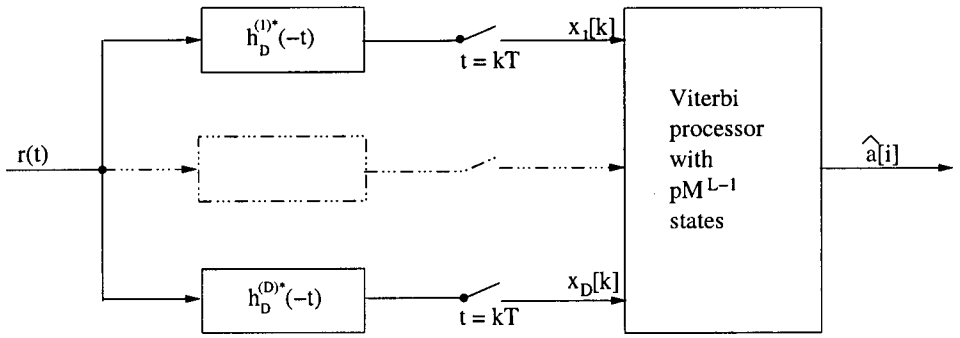

Figure 3.3: Matched filter receiver for CPM using decomposition approach.

Comparing the receiver structure obtained with the Rimoldi/Huber&Liu's decomposition approach with the optimum receiver structure described in Section 2.2, it is observed that the bank of $2M^L$ filters has been replaced by a bank of sub-optimum D-dimensional filters $\boldsymbol{h}_D(t)$. Unlike the optimal filters, the baseband filters $\boldsymbol{h}_D(t)$ are independent of h and the number of states in the Viterbi processor. Also, as mentioned above, the number of states required in the Viterbi processor reduces to pM^{L-1} from $2pM^{L-1}$ for an odd k while it remains the same for an even k.

In the discussion so far, it has been assumed that the channel does not introduce any phase distortion. The effect of phase distortion is discussed in Section 3.3 which describes NSD and the corresponding branch metric calculation.

3.1.3 Application of the Decomposition Approach to Bluetooth

The equivalent transmitter structure for Bluetooth systems using the decomposition approach is shown in Fig 3.4. As mentioned earlier in Section 2.1.1, for Bluetooth systems, $L = 2$, $M = 2$, and h can take any value from 0.28 to 0.35. Therefore, there is only one shift register with the number of signal elements in the signal mapper varying with h.

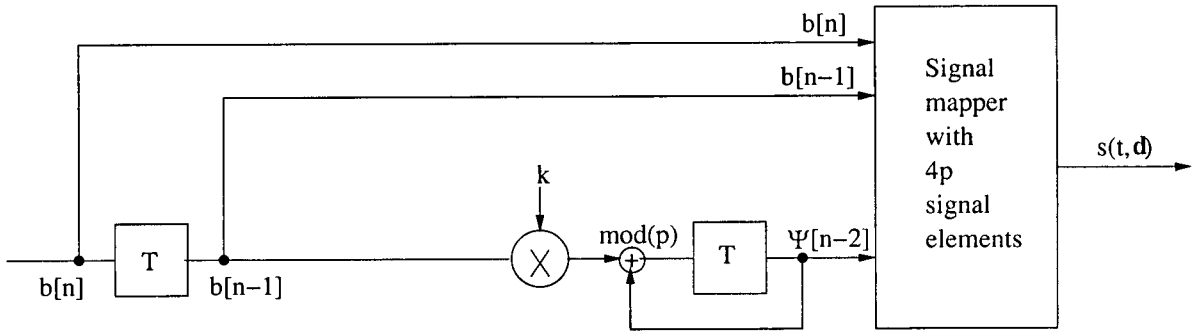

Figure 3.4: Equivalent GFSK modulator using decomposition approach.

The baseband receiver can be represented by a bank of 3 complex exponential filters (cf. Section 3.1.2), followed by a Viterbi processor with $2p$ states. However, for a low cost receiver it is desirable to reduce the number of filters even further. With this intent, a discussion on the required number of filters and on an improved filter design is presented in the following section. Moreover, the problems of varying trellis structure with varying p and the high computational complexity still exist, implying that, the number of states needs to be reduced for all values of h. A state reduction method will be presented in Section 3.4.

3.2 Filter Design

Using the time-limited complex-exponential functions $h_D^{(d)}(t)$, three complex matched filters are required as has been explained in the previous section. However, as GFSK is a very bandwidth efficient modulation scheme, a reduced number of basis function may represent the GFSK signal space with sufficient accuracy. Therefore, the performance of receivers with $D = 2$ and $D = 1$ was investigated. It was found that there is no degradation in performance for $D = 2$, while for $D = 1$ the required $10\log_{10}(E_s/N_0)$ increases by only 0.5 dB to achieve the target BER of 10^{-3} (cf. Section 4.1.1). The number of filters required reduces to one with $D = 1$ as $f_d = 0$. Hence, as reduction in complexity is achieved at the expense of very small loss in performance, it is proposed to use $D = 1$.

As mentioned in Section 1.1, Bluetooth systems operate in the license-free ISM band. Therefore the receiver is required to be robust against co-channel interference (CCI) and adjacent channel interference (ACI) (cf. Section 2.1.2). For effective suppression of ACI, the receiver filter should be able to stop the frequencies outside the passband of 1 MHz of the desired signal. Fig. 3.5 (a) shows the magnitude frequency response of the filter $h_1^{(1)}(t)$ with $D = 1$ from which it may be inferred that the filters proposed in Eq. (3.13) can accomplish only limited ACI suppression. Therefore, the passband characteristics of the proposed receiver filter $h_1^{(1)}(t)$ need to be modified for interference suppression.

The LDI detector is quite robust in the presence of interference [SV01a]. Fig. 3.5 (a) shows the magnitude of the frequency response of the Gaussian pre-filter applied in the LDI receiver with impulse response

$$h_r(t) = \sqrt{\frac{2\pi}{\ln 2}} B_r \mathrm{e}^{-\left(\frac{2\pi^2}{\ln 2}\right)(\mathrm{B_r t})^2}, \tag{3.19}$$

where B_r is the 3 dB bandwidth of the filter, a typical value of which is $B_r T = 0.55$ [SV01a]. While the passband spans more than twice the bandwidth of the desired signal, the stop-

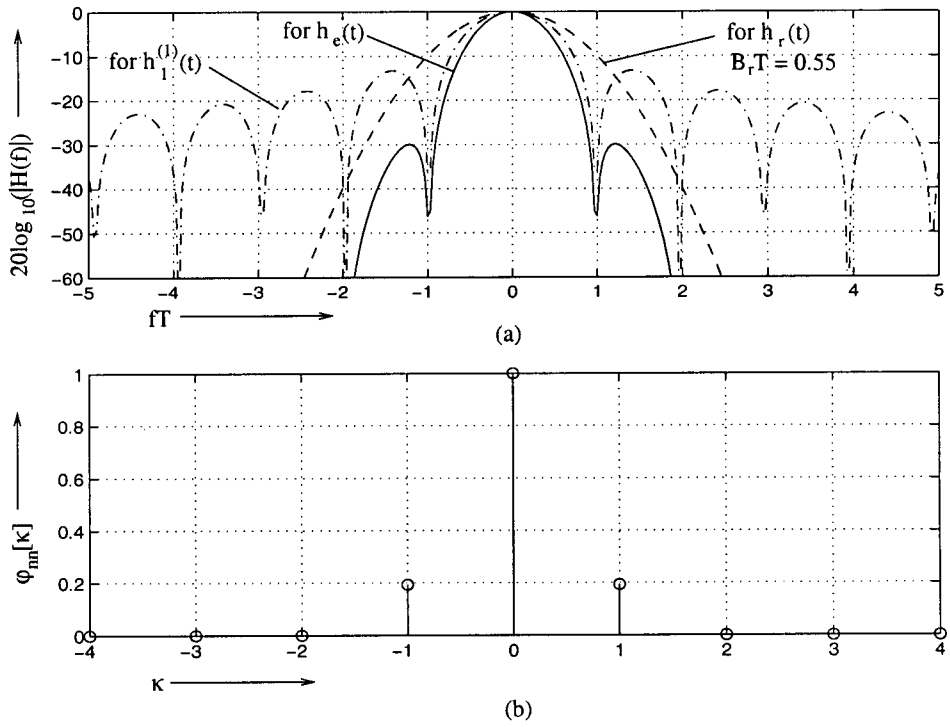

Figure 3.5: (a) Magnitude frequency responses for different filters. (b) Noise autocorrelation function $\varphi_{nn}[\kappa]$ after filter $h_e(t)$ and sampling.

band efficiently suppresses the interference from adjacent channels separated by more than 2 MHz. Therefore, a new filter design is proposed with an additional Gaussian pre-filter $h_r(t)$ cascaded with filter $h_1^{(1)}(t)$, with an effective impulse response

$$h_e(t) = h_r(t) * h_1^{(1)}(t), \tag{3.20}$$

that may be expressed as

$$h_e(t) = \frac{1}{T}\left(\mathrm{Q}(c \cdot B_r(t - T/2)) - \mathrm{Q}(c \cdot B_r(t + T/2))\right) \tag{3.21}$$

with constant $c = 2\pi/\sqrt{\ln(2)}$ and $\mathrm{Q}(t)$ as the standard Gaussian Q-function. The combined filter characteristics $h_e(t)$ are also shown in Fig. 3.5 (a). The passband of $h_e(t)$ is narrower than that of $h_r(t)$ and the stop-band characteristics are significantly improved as compared to the originally proposed filter $h_1^{(1)}(t)$. Therefore, the combined filter is capable of improved interference suppression as demonstrated in the performance results in Section 4.1.1.

Since $h_e(t)$ is not time-limited and $h_e(t) * h_e^*(-t)$ is not a Nyquist pulse, ISI and colored noise are unavoidable after sampling. However, these effects are minor as can be seen from the rapidly decaying noise autocorrelation function depicted in Fig. 3.5 (b). For this reason and for the sake of simple implementation, ISI and noise coloring are neglected in the following NSD design. The performance results, however, include these effects which are not major as seen in the results presented in Section 4.1.1.

3.3 Noncoherent Sequence Detection

As discussed in Section 2.2, coherent detection or optimum noncoherent detection are not feasible solutions for the desired low cost Bluetooth receiver design. For derivation of a sub-optimum NSD metric for GFSK from the optimum NSD metric discussed in Section 2.2.1, the channel phase is assumed to be constant. However, since practical Bluetooth devices are required to cope with time-variant channel phase (cf. Section 2.1.2), the assumption of constant channel phase will be relaxed later in this section. For linear modulation schemes with constant envelop it has been shown [CR99] that the maximum likelihood noncoherent sequence detector derived from Eq. (2.20) for optimum NSD, for a block of N_T transmitted symbols maximizes the sequence metric

$$\Lambda[N_T - 1] = \Re\left\{\sum_{n=1}^{N_T-1} r[n]\tilde{\boldsymbol{c}}^*[n] \sum_{l=0}^{n-1} r^*[l]\tilde{\boldsymbol{c}}[l]\right\} \tag{3.22}$$

where $\tilde{\boldsymbol{c}}$ is the code sequence uniquely associated with the hypothetical information sequence $\tilde{\boldsymbol{a}}$ and $r[i]$ are the received samples. The incremental metric $\lambda[i] = \Lambda[i+1] - \Lambda[i]$ can be written as

$$\lambda[i] = \Re\{r[i]\tilde{\boldsymbol{c}}^*[i] \sum_{l=0}^{i-1} r^*[l]\tilde{\boldsymbol{c}}[l]\}. \tag{3.23}$$

The receiver front end derived in Section 3.1.2, allows the application of the noncoherent detection method for linear modulation given by Eq. (3.22) directly to CPM [LSEH01]. Unlike other demodulation schemes for CPM, cf. e.g. [CR98], a whitening matched filter is

not required for the receiver design discussed in Section 3.1.2. Hence, the sequence metric for a block of N_T symbols and the incremental branch metric for MLSD of CPM using the decomposition approach can be written respectively as [LSEH01]

$$\Lambda[N_T-1] = \Re\left\{\sum_{n=1}^{N_T-1} \boldsymbol{x}[n]\boldsymbol{\rho}^H(\tilde{\boldsymbol{d}}[n])\tilde{q}^*_{\text{ref}}[n-1]\right\}, \tag{3.24}$$

and

$$\lambda[i] = \Re\{\boldsymbol{x}[i]\boldsymbol{\rho}^H(\tilde{\boldsymbol{d}}[i])\tilde{q}^*_{\text{ref}}[i-1]\} \tag{3.25}$$

where $\tilde{q}_{\text{ref}}[i-1]$ is the reference phase for the survivor path corresponding to the hypothetical information sequence address vector $\tilde{\boldsymbol{d}}[i]$, $0 \leq i \leq N_T-2$, and is defined as

$$\tilde{q}_{\text{ref}}[i-1] = \sum_{l=0}^{i-1} \boldsymbol{x}[l]\boldsymbol{\rho}^H(\tilde{\boldsymbol{d}}[l]). \tag{3.26}$$

The expression for branch metric given by Eq. (3.25) is similar to branch metric computation for coherent metric using Eq. (3.18) where channel phase is known at receiver. Since under low noise conditions $\boldsymbol{x}[l]\boldsymbol{\rho}^H(\tilde{\boldsymbol{d}}[l]) \approx e^{j\phi_0}$ for correct hypothetical sequence, the phase reference gives the average of the estimated channel phase over all transmitted bits. Therefore, for constant channel phase the phase reference can be interpreted as the implicit estimation of the phase distortion introduced by the channel. However, in practice, the assumption of constant channel phase over the whole transmission period is not true. Moreover, the computation of the phase reference in Eq. (3.26) is done over all the transmitted symbols. The number of transmitted symbols grows linearly with time, thereby, introducing unlimited phase memory. Therefore, in order to limit the complexity of the receiver and to relax the constant channel phase assumption, the application of a rectangular and a exponential observation window has been proposed [CR99][SG99] as will be explained in the following two sections.

3.3.1 Rectangular Windowing

Colavolpe and Raheli proposed the use of a rectangular window of length N, $N \ll N_T$ and $N \geq 2$, to limit the number of observations while calculating the phase reference, with equal weight given to each observation in the window. Hence, the phase memory is truncated to the N most recent symbols, the phase reference calculation thus becomes [CR99]

$$\tilde{q}_{\text{ref}}^{N}[i-1] = \sum_{l=i-N+1}^{i-1} \boldsymbol{x}[l]\boldsymbol{\rho}^{H}(\tilde{\boldsymbol{d}}[l]), \quad i \geq N-1, \tag{3.27}$$

where $\tilde{q}_{\text{ref}}^{N}[i-1]$ represents the modified phase reference. The channel phase is assumed to be constant only over the period of N symbol intervals. The new branch metric, referred to as N-metric is defined as

$$\lambda^{N}[i] = \Re\{\boldsymbol{x}[i]\boldsymbol{\rho}^{H}(\tilde{\boldsymbol{d}}[i])\tilde{q}_{\text{ref}}^{N*}[i-1]\}. \tag{3.28}$$

The phase reference is updated as

$$\tilde{q}_{\text{ref}}^{N}[i] = \boldsymbol{x}[i]\boldsymbol{\rho}^{H}(\tilde{\boldsymbol{d}}[i]) + \tilde{q}_{\text{ref}}^{N}[i-1] - \boldsymbol{x}[i-N+1]\boldsymbol{\rho}^{H}(\tilde{\boldsymbol{d}}[i-N+1]). \tag{3.29}$$

With the increase in the length of the window N, the number of data samples increases, resulting in a decrease in noise variance of the phase estimation. Therefore, the phase estimation becomes better with an increase in N for approximately constant channel phase. However, if the phase of the channel varies with time, for example in the presence of phase jitter or frequency offset, the noise variance may increase with increasing N, causing a deterioration in the performance. The optimum value of N depends on the SNR and the channel characteristics. Performance results for the proposed receiver with N-metric for different values of N and under different channel conditions are given in Section 4.1.2.

3.3.2 Exponential Windowing

An exponentially decaying window was proposed in [SG99], where an unlimited size window is adopted but the weight given to each observation decays exponentially with time. The

most recent observation is given a maximum weight of one. The phase reference is updated recursively by [SG99]

$$\tilde{q}_{\text{ref}}^{\alpha}[i] = \boldsymbol{x}[i]\boldsymbol{\rho}^{H}(\tilde{\boldsymbol{d}}[i]) + \alpha \cdot \tilde{q}_{\text{ref}}^{\alpha}[i-1] \tag{3.30}$$

where α is the forgetting factor, $0 \leq \alpha < 1$. The corresponding branch metric is called α-metric. The N-metric and α-metric are identical for the special cases $N = 2$, $\alpha = 0$ and $N \to \infty$, $\alpha \to 1$. As for the N-metric the optimum value of α depends on the SNR and the channel characteristics. As α approaches one, all the observations are given the same weight of 1, which is favorable if the channel phase is constant, but affects the performance adversely in a time-varying channel.

In terms of the computational processing required for updating the phase reference, a comparison of Eqs. (3.29) and (3.30) reveals that the α-metric requires less arithmetic operations compared to the N-metric. Hence, for a simple receiver design the α-metric is preferable. A performance comparison of the two metrics is given in Section 4.1.2.

3.3.3 Frequency Offset Estimation

The NSD using the α-metric or the N-metric is very power efficient and robust against channel phase variations. However, the frequency offset Δf allowed in the Bluetooth systems is of the order of ± 100 kHz [BTS03], i.e., the normalized offset $\Delta f T$ can be as large as ± 0.1. To cope with such high frequency deviations it is mandatory to estimate the frequency offset Δf and incorporate the effect of Δf into the definition of the phase reference. The maximum-likelihood function for sequence detection now has to maximize the joint function for data detection and frequency estimation [CR02]. The sequence metric equivalent to Eq. (3.22) for equal-energy, linearly modulated signals is obtained by introducing a

trial value of the frequency offset $\Delta\tilde{f}$ [CR02, Eq. 18]

$$\Lambda[N_T]_{\tilde{\mathbf{a}},\Delta\tilde{f}} = \Re\left\{\sum_{n=1}^{N_T-1} r[n]\tilde{\mathbf{c}}^*[n]\sum_{l=0}^{n-1} r^*[l]\tilde{\mathbf{c}}[l]\mathrm{e}^{-j2\pi(n-l)\Delta\tilde{f}T}\right\} \tag{3.31}$$

in which the inner sum (index l) is the new estimate of the channel phase. Applying Eq. (3.31) to CPM and truncating the memory using exponential windowing, the modified reference symbol can now be defined as:

$$q_{\mathrm{ref}}^{\alpha}[i] = \left(\alpha q_{\mathrm{ref}}^{\alpha}[i-1] + \boldsymbol{x}[i]\boldsymbol{\rho}^H(\tilde{\boldsymbol{d}}[i])\right)\mathrm{e}^{j2\pi\Delta\hat{f}[i-1]} \tag{3.32}$$

with the frequency offset estimate

$$\mathrm{e}^{j2\pi\Delta\hat{f}[i]} = \frac{p_{\mathrm{ref}}[i]}{|p_{\mathrm{ref}}[i]|} \tag{3.33}$$

obtained using the adaptive estimator

$$p_{\mathrm{ref}}[i] = \beta q_{\mathrm{ref}}[i-1] + \boldsymbol{x}[i]\boldsymbol{\rho}^H(\tilde{\boldsymbol{d}}[i])(\boldsymbol{\rho}(\tilde{\boldsymbol{d}}[i-1])\boldsymbol{x}^H[i-1]). \tag{3.34}$$

β is the forgetting factor for the calculation of $p_{\mathrm{ref}}[i]$, $0 \leq \beta < 1$. The second term in Eq. (3.34) can be interpreted as an estimate of the frequency drift over one symbol duration because for high SNR and low noise conditions $\boldsymbol{x}[i]\boldsymbol{\rho}^H(\tilde{\boldsymbol{d}}[i])(\boldsymbol{\rho}(\tilde{\boldsymbol{d}}[i-1])\boldsymbol{x}^H[i-1]) \approx \mathrm{e}^{j(\phi_c[i]-\phi_c[i-1])}$ for $\tilde{\boldsymbol{d}}[i] = \boldsymbol{d}[i]$. By using Eq. (3.32) in the branch metric Eq. (3.25), NSD is still robust against random phase noise and residual frequency offsets ($\Delta f - \Delta\hat{f}$), but it now explicitly accounts for the most prominent and systematic contributor to the phase variations in Bluetooth systems, i.e., oscillator frequency offset.

The chosen approach is similar to frequency estimation for NSD and linear modulation advocated by Colavolpe and Raheli in [CR02]. Moreover, at typically required SNRs the estimator in Eq. (3.34) resembles Kay's frequency estimator [Kay89], which was also found advantageous in [CR02]. Both Eq. (3.32) and Eq. (3.34) are different from [CR02] and [Kay89] respectively, in that recursive update equations are formulated, which (a) involves

less arithmetic operations than rectangular windowing and (b) are specially well-suited for per-state tracking in the trellis of NSD. It is also worth noting that the devised frequency offset estimation for NSD corresponds to the use of DC offset cancellation methods for the LDI receiver, which were found necessary to compensate the severe frequency offsets encountered in Bluetooth, cf. e.g. [LDF93].

3.4 State Reduction

So far, with the application of the decomposition approach and NSD to Bluetooth, a simple receiver structure has been obtained consisting of a single filter and a Viterbi processor with a simple phase estimation algorithm. However, the varying number of states in the Viterbi processor complicates the receiver structure. A reduction in the number of states to a value independent of h is desirable, and this is readily accomplished by following the per-survivor-processing (PSP) approach [RPT95].

As described in Section 3.1.1, the state vector of the modified trellis using a unipolar information sequence and normalized phase state for Bluetooth system is given by (using Eq. (3.10))

$$\boldsymbol{S}_n^{2p} = [\Psi[n-2], b[n-1]] \tag{3.35}$$

where $\Psi[n-2]$ is updated using (cf. Eq. (3.9))

$$\Psi[n-2] = (\Psi[n-3] + kb[n-2]) \bmod(p). \tag{3.36}$$

There are $2p$ states, i.e., if $h = 1/3$, the number of states is 6 and if $h = 0.29 = 29/100$, the number of states is 200. The large and variable number of states is mainly contributed by the phase state $\Psi[n]$, which can take values from 0 to $(p-1)$. Following the PSP approach [RPT95], the number of states can be reduced if the phase state is decided tentatively according to the survivor path terminating in the current state, thus reducing the number

of states to two. The new state vector is defined as

$$\boldsymbol{S}_n^2 = [\tilde{\Psi}[n-2], b[n-1]] \tag{3.37}$$

where $\tilde{\Psi}[n-2]$ is the phase state of the survivor path at n^{th} time interval for the current state. As the phase state is not allowed to vary anymore, the only variable in the definition of the state vector is $b[n-1]$, which can take two possible values $\{0, 1\}$. Hence, the state is defined by $b[n-1]$ only and the associated phase state is used for branch metric calculation. Fig. 3.6 shows the two-state trellis structure. $\tilde{\Psi}_m[i]$ is the phase state associated with state m, $m \in \{0, 1\}$ at instant iT.

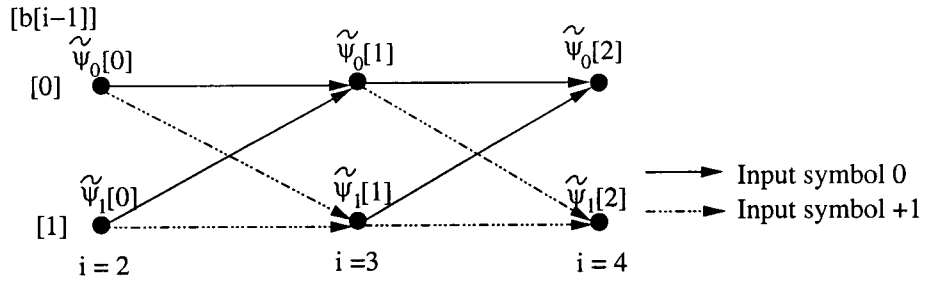

Figure 3.6: Two-state trellis structure.

State reduction to one can similarly be achieved by taking a tentative decision on the phase state as well as $b[n-1]$ for the survivor path. Hence,

$$\boldsymbol{S}_n^1 = [\tilde{\Psi}[n-2], \tilde{b}[n-1]] \tag{3.38}$$

where both $\tilde{\Psi}[n-2]$ and $\tilde{b}[n-1]$ are fixed and correspond to the phase state of the survivor path and the last added symbol to the survivor path. Hence, there is only one survivor path and the symbol is detected based on the branch metric instead of the path metric. The modified one-state trellis is shown in Fig. 3.7.

The following example demonstrates the difference between the three trellis structures for $h = 1/3$. The phase state is updated using $\Psi[n-2] = [\Psi[n-3] + b[n-2]] \bmod(3)$.

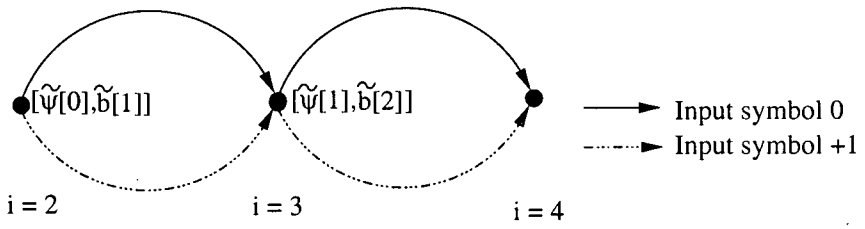

Figure 3.7: One-state trellis structure.

The path trellis for the example is drawn in Fig. 3.8, where all the states are shown. However, the attainable states depend on the trellis structure that is explained below. The full-state trellis has six survivor paths and therefore, can attain all the six states $\{(0,0),(1,0),(2,0),(0,1),(1,1),(2,1)\}$, where the first term in the bracket is the phase state and the second term is the previous input according to the definition of state vector in Eq. (3.35). Similarly, the possible two states for the two-state trellis are either from $\{(0,0),(1,0),(2,0)\}$ or from $\{(0,1),(1,1),(2,1)\}$ and the one-state trellis has only one survivor path which can attain any one state from $(0,0),(1,0),(2,0),(0,1),(1,1)$ and $(2,1)$. In this example, the initial state at $i = 0$ is assumed to be $(1,1)$.

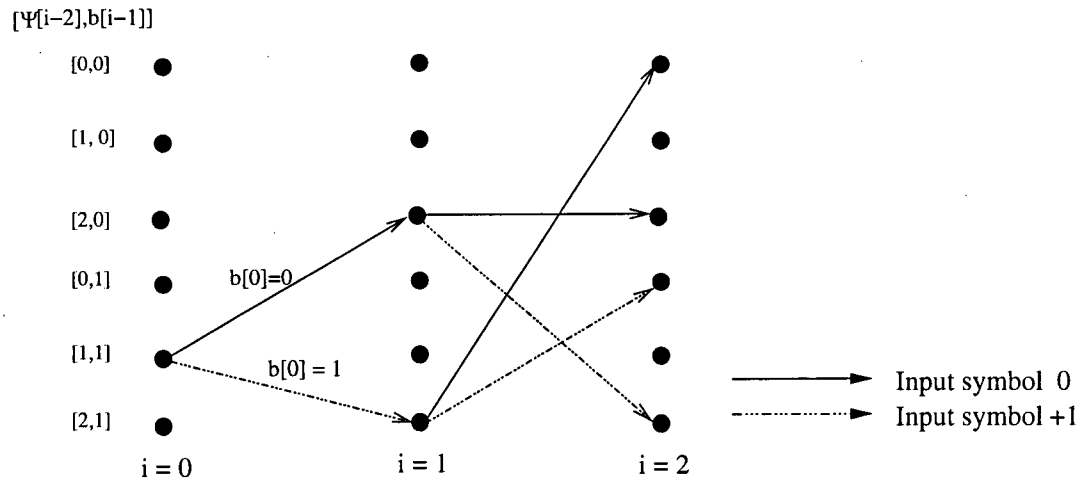

Figure 3.8: An example for the path trellis for $h = 1/3$ to illustrate state reduction.

At instant $i = 1$, the two-state trellis has two survivor paths terminating at states $(2,0)$ and $(2,1)$, but for the one-state trellis only the path with the best branch metric out of

these two survives and the symbol added to the survivor path corresponds to $b[0]$ with the higher branch metric. At instant $i = 2$, the two-state trellis selects one out of the two survivor paths terminating at $(0,1)$ and $(2,1)$ for state '1' and one out of $(0,0)$ and $(2,0)$ for state '0' based on the respective path metric. However, in a full-state trellis none of these paths are terminated and all the four paths continue to trace the sequence.

It is interesting to consider the minimum distance for all the three cases of full-state, two-state, and one-state trellis. As the possible trajectories and error events change with state reduction, the minimum distance changes too, thereby affecting the BER. The distance between the correct and the erroneous path is the difference of their path metrics, which is calculated by adding the branch metric of each trajectory in the path. The branch metric is calculated using Eq. (3.25), i.e., $\lambda[i] = \Re\{\boldsymbol{x}[i]\boldsymbol{\rho}^H(\tilde{\boldsymbol{d}}[i])\tilde{q}^{\alpha *}_{\text{ref}}[i-1]\}$, where $q^{\alpha}_{\text{ref}}[i-1]$ is given by Eq. (3.32) with $\alpha = 0.6$ and $\beta = 0.9$, and $\boldsymbol{x}[i]$ represents noiseless received signal samples here. Table 3.1 gives all possible branch metrics for $h = 1/3$. Fig. 3.9 shows an example of a two adjacent error events path along with the corresponding correct path for the full-state trellis. For the path metric calculation of the erroneous path, the address vector for $\boldsymbol{x}[i]$

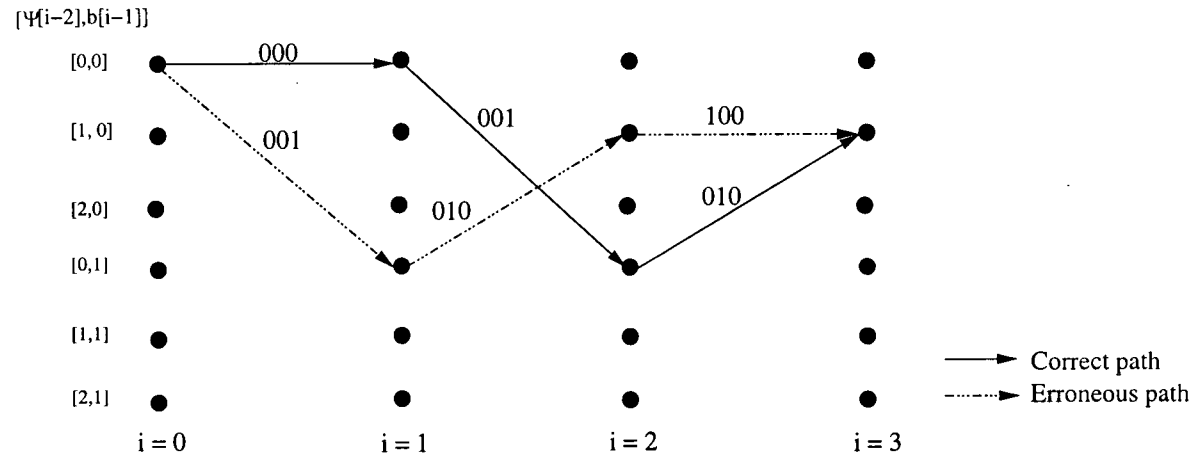

Figure 3.9: Full-state path trellis for two error event example.

are the digits over the correct path and the address vector for $\boldsymbol{\rho}(\tilde{\boldsymbol{d}}[i])$ are the digits over the

erroneous path in Fig. 3.9. Therefore, the difference of the path metrics at instant $i = 3$ is

$$\begin{aligned} D_3^{2p} &= B(000,000) + B(001,001) + B(010,010) - B(000,001) - B(001,010) - B(010,100) \\ &= 0.7593. \end{aligned}$$

where $B(x, y)$ refers to the entry in the Table 3.1.

Similarly, for the two-state trellis, Fig. 3.10 shows the trellis path for the same example of two adjacent error events. Comparing Figs. 3.9 and 3.10 it can be observed that the distance between the correct and erroneous path for the two-state trellis is the same as that for full-state trellis, i.e.,

$$\begin{aligned} D_3^{2} &= B(000,000) + B(001,001) + B(010,010) - B(000,001) - B(001,010) - B(010,100) \\ &= 0.7593. \end{aligned}$$

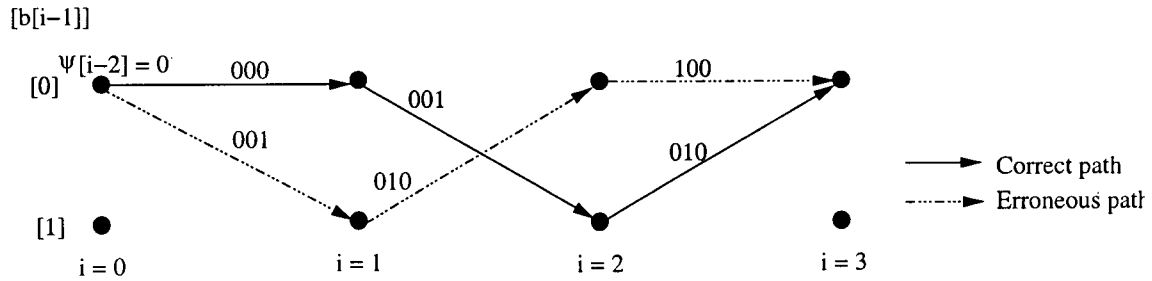

Figure 3.10: Two-state path trellis for two error event example.

For the one-state trellis the distance between the two paths is given by the difference of their branch metrics. Fig. 3.11shows an example of a one error event path. The distance between the two paths is

$$D_1^1 = B(000,000) - B(000,001) = 0.01135.$$

The comparison of these three examples illustrates that while for the full-state trellis and two-state trellis the distance in the correct and the erroneous path is the same, for the

Table 3.1: Branch metric table for $h = 1/3$.

x[i] \ $\rho(\tilde{d}[i])$	000	100	200	010	110	210	001	101	201	011	111	211
000	0.70978	−0.35489	−0.35489	−0.16076	−0.53958	0.70035	0.69843	−0.54385	−0.15485	−0.36018	−0.34957	−0.70975
100	−0.35489	0.70978	−0.35489	0.70035	−0.16077	−0.53958	−0.15458	0.69843	−0.54384	0.70975	−0.36018	−0.34957
200	−0.35489	−0.35489	0.70978	−0.53958	0.70035	−0.16077	−0.54385	−0.15458	0.69843	−0.34957	0.70975	−0.36018
010	−0.16077	0.70035	−0.53958	0.75843	−0.37922	−0.37922	0.068475	0.61990	−0.68837	0.69843	−0.54385	−0.1545 8
110	−0.53958	−0.16077	0.70035	−0.37922	0.75843	−0.37922	−0.68837	0.06847	0.61990	−0.15458	0.69843	−0.54385
210	0.70035	−0.53958	−0.16077	−0.37922	−0.37922	0.75843	0.61990	−0.68837	0.06848	−0.54385	−0.15459	0.69843
001	0.69843	−0.15484	−0.54385	0.06847	−0.68838	0.61990	0.75843	−0.37921	−0.37921	−0.16077	−0.53958	0.70035
101	−0.54385	0.69843	−0.15484	−0.61990	0.06847	−0.68837	−0.37921	0.75843	−0.37921	0.70035	−0.16077	−0.53958
201	−0.15458	−0.54385	0.69843	−0.68837	0.61990	0.06847	−0.37922	−0.37922	0.75843	−0.53958	0.70035	−0.16077
011	−0.36018	0.70975	−0.34957	0.69843	−0.15458	−0.54385	−0.16077	0.70035	−0.53958	0.70978	−0.3549	−0.3549
111	−0.34957	−0.36018	0.70975	−0.54385	0.69843	−0.15458	−0.53958	−0.16077	0.70035	−0.35489	0.70978	−0.35489
211	0.70975	−0.34957	−0.36018	−0.15458	−0.54385	0.69843	0.70035	−0.53958	−0.16077	−0.35489	−0.3459	0.70978

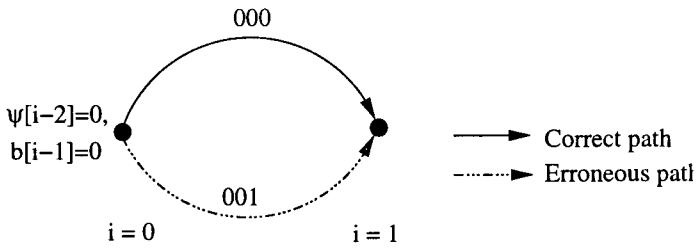

Figure 3.11: One-state path trellis for one error event example.

one state trellis the distance drops by a factor of 65 approximately. Therefore, the probability of error in the presence of noise increases for the one-state trellis while for the two-state trellis it is expected to remain the same as that for the full-state trellis if double adjacent errors is the most prominent error event. This observation is verified by the results shown in Section 4.1.3. Therefore, a two-state trellis structure is a viable solution for the reduced complexity Bluetooth receiver.

3.5 Adaptive Noncoherent Sequence Detection

In the previous section, the effect of a varying modulation index h on the number of states in the trellis has been considered. However, the demodulation frequency f_r is also dependent on h as can be observed from Eq. (3.3), i.e., $f_r = f_c - h\frac{M-1}{2T}$. The deviation of estimated modulation index $\hat{h}$ at the receiver from the true modulation index h of the transmitted signal introduces a frequency offset of $\Delta f_h = \frac{(\hat{h}-h)}{2T}$, hence, deteriorating the performance of NSD. Secondly, h affects $\boldsymbol{\rho}(\tilde{\boldsymbol{d}}[i])$ because of its dependence on f_r and $\tilde{\boldsymbol{d}}[i]$. As $\tilde{\boldsymbol{d}}[i] = [\Psi[i-2], b[i-1, b[i]]$, $\Psi[i-2] \in \{0, 1, ..., (p-1)\}$, the number of address vectors is dependent on h, irrespective of the number of states defined in the trellis. Lastly, h also affects the phase reference $q_{\text{ref}}[i]$ as it is dependent on the received filtered samples $\boldsymbol{x}[i]$ and $\boldsymbol{\rho}(\tilde{\boldsymbol{d}}[i])$. Therefore, for an optimum performance of the receiver the modulation index of the transmitted signal is required to be known at the receiver.

For a low-complexity receiver, the sequence detector could operate with an assumed nominal value $\hat{h}$, regardless of its actual value. But the results given in Section 4.2.1 show that there is a considerable performance degradation as h at the transmitter is allowed to vary in a relatively large interval of 0.28 to 0.35. Therefore, for an acceptable performance under variable h conditions an h estimation scheme is suggested. For a simple receiver design, it is proposed to estimate h by performing NSD for a small number of hypotheses $\tilde{h} \in \mathcal{H}$, where $\mathcal{H}$ is the set of hypotheses, over an estimation period of N_e symbols. The hypothesis yielding the best metric (Eq. (3.24)) in the estimation period N_e is chosen as the estimated modulation index $\hat{h}$ and is used to detect the rest of the sequence, i.e.,

$$(\hat{a}[1], ..., \hat{a}[N_e], \hat{h}) = \underset{\tilde{d}[1],...,\tilde{d}[N_e],\tilde{h}\in\mathcal{H}}{\operatorname{argmax}} \left\{ \Re \left\{ \sum_{i=1}^{N_e} \boldsymbol{x}[i] \boldsymbol{\rho}^H(\tilde{\boldsymbol{d}}[i]) \tilde{q}^*_{\text{ref}}[i-1] \right\} | \tilde{h} \right\}. \tag{3.39}$$

This adaptive NSD can be regarded as an approximate maximum likelihood joint detection and estimation with quantization of the unknown parameter h. For a reasonably small number of tested hypotheses and short estimation periods, e.g. $|\mathcal{H}| = 2, 4$ and $N_e = 25, 50$, the complexity increase due to adaptation is almost negligible. However, considerable improvement in the performance under varying h conditions is obtained. The performance results of adaptive NSD (ANSD) are discussed in Section 4.2.1. Under low noise conditions, the performance of ANSD remains the same whether the symbols during the estimation period are known or not. The complexity of ANSD can be reduced by using smaller values of N_e. Reduction of N_e from 50 to 25 introduces only 0.3 dB loss in performance (cf. Section 4.2.2). The performance improves if the number of hypotheses is increased, however, if frequency offset cancellation is also employed then even two hypotheses yield good results. The reason of better performance with frequency offset estimation is that the frequency drift introduced by the mismatched h is implicitly alleviated by the proposed frequency offset estimation method (cf. Section 3.3.3).

3.6 Channel Coding

As described in Section 2.1.3, Bluetooth devices employ a rate 1/3 repetition code (RC) and a rate 2/3 expurgated Hamming code (HC) for error correction purpose at the receiver. A conventional FEC decoder uses hard-decision decoding subsequent to NSD to retrieve $\hat{\boldsymbol{a}}[i]$. Conventionally, both FEC schemes are utilized to correct only single errors incurred in the transmission for LDI detectors with hard decoding. However, an analysis of the error patterns of the decoded information sequence shows that there is a very high probability of two consecutive errors. For example, an information sequence '101' is received as '011' with a high probability. In general, if $\bar{a}[i]$ denotes a complement of $a[i]$, then the most likely error event is $\{a[i], a[i+1] = \bar{a}[i], a[i+2]\}$ received as $\{\bar{a}[i], \bar{a}[i+1], a[i+2]\}$, i.e., double adjacent errors (DAE) are incurred, which cannot be corrected using the rate 1/3 RC or a single error correcting HC. Fig. 3.12 shows the frequency of five different error patterns occurring in a block of 10 symbols in the two-state NSD and the LDI detector output confirming high occurrence of DAE. The frequency of DAE is much higher in the proposed receiver as compared to the LDI detector. The following error analysis gives an in-depth investigation of the observed error patterns.

3.6.1 Error Analysis

To study the behaviour of the channel for coded and uncoded transmission the analytical results for the binary symmetric channel (BSC) are compared with simulations results. Section 2.2.2 introduced the theoretical lower performance bound for MLSD. Fig. 3.13 shows the graph for the theoretical and the simulated BER vs. $10\log(E_s/N_0)$. It may be observed that the simulation results are in agreement with the analytical MLSD performance for uncoded BER. For coded transmission, the analytical and simulation results of performance can be compared for code-word error rate. For a BSC with error probability BER, the code-

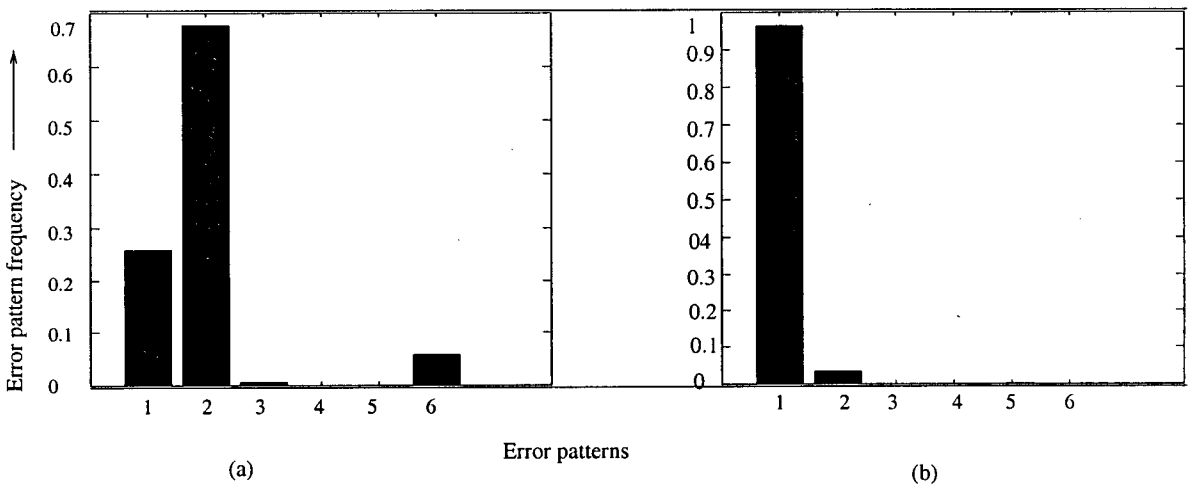

Figure 3.12: Error pattern frequency for (a) NSD with two-states at 11 dB with $\alpha = 0.6$, $\beta = 0.9$, and (b) LDI detector at 16 dB. (Error patterns in a block of 10 symbols: 1-'010'; 2-'0110'; 3-'01010',4-'010010', 5-'0100010', 6-others, where '1' represents an error.)

word error rate (WER) for the rate 1/3 RC is obtained as [Pro01, Ch. 8]

$$\text{WER} = 1 - (1 - \text{BER})^3 - 3 \cdot \text{BER}(1 - \text{BER})^2. \tag{3.40}$$

The WER for (15,10) HC is given by [Pro01, Ch. 8]

$$\text{WER} = 1 - (1 - \text{BER})^{15} - 15 \cdot \text{BER}(1 - \text{BER})^{14}. \tag{3.41}$$

The analytical and simulation results for the WER of RC and HC are also plotted in Fig. 3.13. It can be observed that for BER $= 10^{-3}$, the $10\log(E_s/N_0)$ corresponding to the analytical results for RC (Eq. (3.40)) is 5 dB while it is observed as 7 dB for the simulation results. Similarly for HC at BER $= 10^{-3}$ the difference in $10\log(E_s/N_0)$ for analytical and simulated value is 3 dB. The considerable gap between analytical and simulation results for both the RC and the HC WER curves suggests that the memoryless channel model assumed for Eqs. (3.40) and (3.41) is inadequate.

To investigate the channel memory in more detail, the error-gap-distribution (EGD) of the NSD receiver output and LDI detector output is observed. The EGD is obtained as

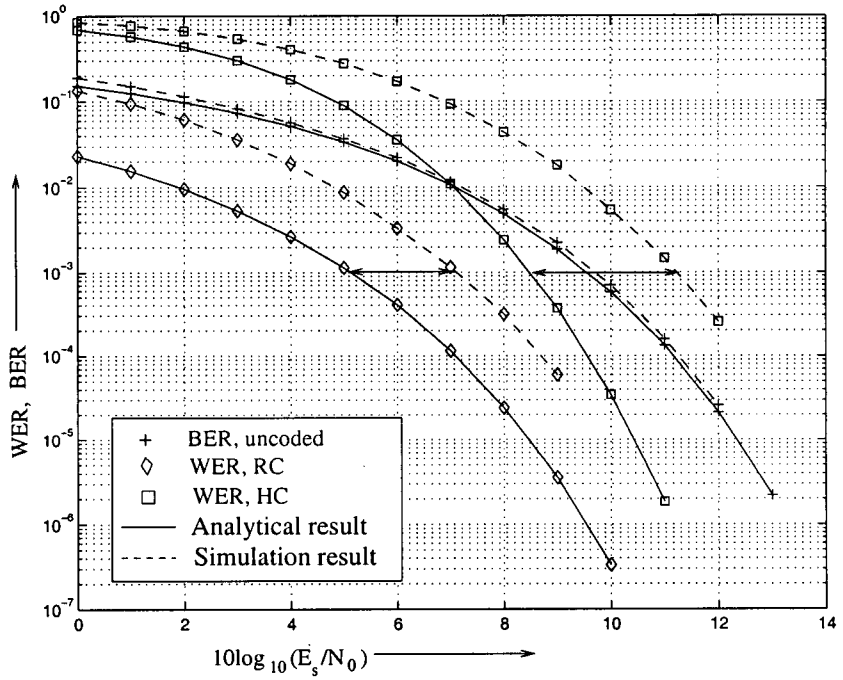

Figure 3.13: BER for uncoded transmission and WER for transmission with 1/3 rate repetition code and (15,10) Hamming code over AWGN channel. Analytical results according to Eq. (2.25) (BER), Eq. (3.40)(WER-RC) and Eq. (3.41)(WER-HC).

[AFK72]

$$\Pr\{0^m|1\} = \sum_{k=m}^{\infty} \Pr(0^k 1|1) \tag{3.42}$$

where a one in the sequence represents an error and 0^k1 is the representation of a sequence of k 0's followed by a one. Thus, the EGD gives the probability of an error-free run of length m after the occurrence of an error. Therefore, $m = 0$ is the event of consecutive errors or DAEs, $m = 1$ is the error pattern of type '101' and error patterns for $m > 1$ can be similarly obtained. The EGDs of the outputs of full-state NSD, two-state NSD, LDI detector, and for a BSC are shown in Fig. 3.14. To obtain EGD of the BSC, an interleaver is implemented between encoder and modulator. A corresponding deinterleaver is employed at the receiver after the Viterbi decoder, thus, eliminating the effect of memory introduced by GFSK modulation.

From Fig. 3.14 it may be observed that for the BSC, the probability of error is independent of the error gap, whereas, for the NSD and LDI detectors the probability of $m = 0$ is quite high as compared to non-zero values of m, implying that the probability of DAE is higher as compared to single error events. The inherent memory of partial response GFSK introduces DAE in the output of all the three detectors. Full-state NSD and two-state NSD employs sequence detection which properly takes into account the GFSK modulation memory and therefore, suffers from higher DAE. The two-state NSD further enhances this effect due to the application of PSP in the detection algorithm.

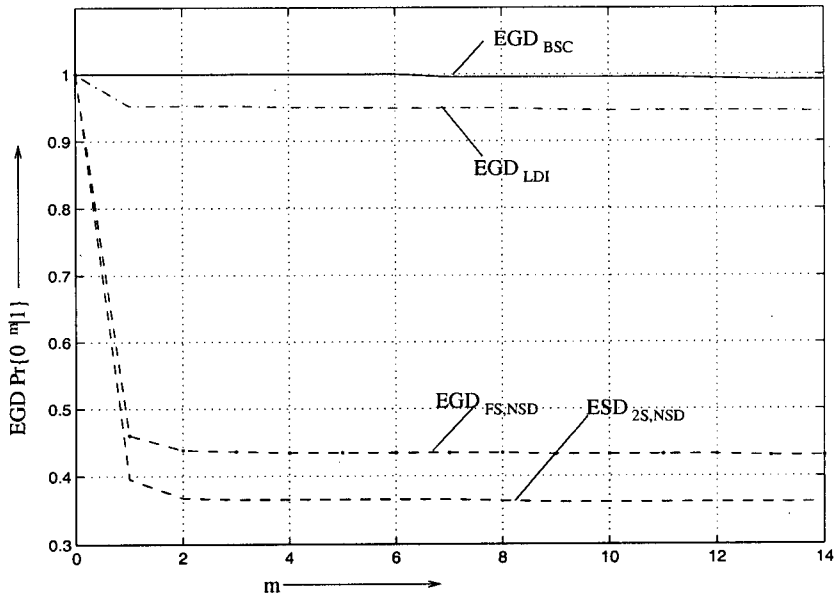

Figure 3.14: Error-gap distribution (EGD) $\Pr\{0^m|1\}$ for AWGN channel. EGD_{LDI}: LDI detector output at 16 dB, $\text{EGD}_{\text{FS,NSD}}$: Full-state NSD with $\alpha = 0.6$, $\beta = 0.9$ at 11 dB, $\text{EGD}_{\text{2S,NSD}}$: Two-state NSD with $\alpha = 0.6$, $\beta = 0.9$ at 11 dB, and EGD_{BSC}: ideal BSC with approximately same BER as LDI and NSD.

As mentioned before, the most likely error event for NSD is $\{a[i], a[i+1] = \bar{a}[i], a[i+2]\} \rightarrow \{\bar{a}[i], \bar{a}[i+1], a[i+2]\}$ which is now supported by EGD analysis. The reason for this is that the first error introduces a phase slip resulting in a $2\pi h$ difference in the correct phase state. Due to PSP of the survivor path, this phase slip affects the next decision,

causing another error event that compensates the phase slip, restoring the correct phase state of the survivor path. The next most likely event is of type $\{a[i], a[i+1] = a[i]\}$ being detected as $\{\bar{a}[i], a[i+1]\}$, i.e., a single erroneous decision, which is followed by another error event with high probability to restore the correct phase. Fig. 3.15 depicts DAE and an example for the second most likely error event.

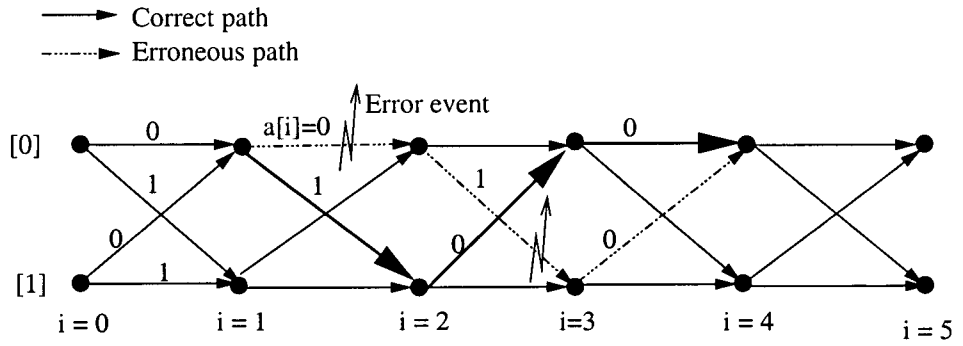

Starting at i=1, Correct Path: 100, Erroneous Path: 010

(a) Double adjacent error event.

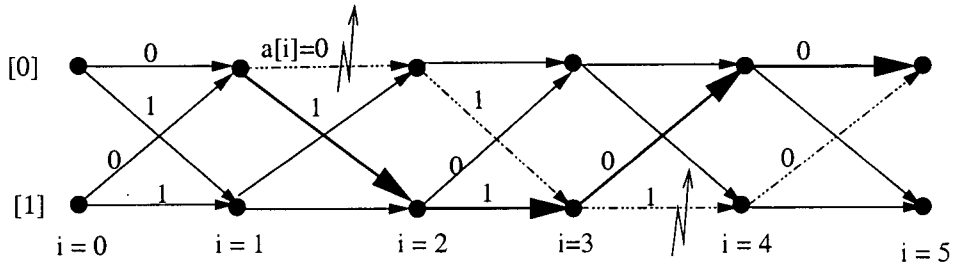

Starting at i=1, Correct Path: 1100, Erroneous Path: 0110

(b) An example for the second most likely error event.

Figure 3.15: The most likely error events for the considered channel.

Motivated by the high probability of burst errors of length two, improved decoding schemes are suggested for RC and HC in the following sections.

3.6.2 Joint NSD and Decoding for Rate 1/3 RC

The most likely error event introduces two errors in two blocks of three symbols at the NSD output, e.g. the coded symbol sequence '000111' may be erroneously received as '001011'

at the NSD output. These two errors can be corrected using repetition hard decoding. However, the high probability of DAE may introduce two DAEs affecting a single block of 3 bits, e.g., a coded sequence of '000111000' is detected as '001010100' after NSD introducing 2 incorrigible errors. Therefore, to improve the receiver performance, it is proposed to perform NSD and decoding jointly, i.e., to decode while detecting the sequence. The joint NSD and decoding restricts the decoded sequence for a coded sequence '000111000' to be either correct '000111000' or incorrect '000000000', i.e., the information sequence $\{a[i], a[i+1], a[i+2], a[i+3]\}$ can be erroneously estimated as $\{\bar{a}[i], \bar{a}[i+1], \bar{a}[i+2], a[i+3]\}$, where due to encoding $a[i] = a[i+1] = a[i+2]$ is enforced. The modified trellis in Fig. 3.16 shows the paths for the correct coded sequence i.e '01110' and the most likely error event '00000'. For hard decoding, the decision about the survivor path for each state is taken at every instant and is decoded after the sequence detection is complete. In joint NSD and decoding of RC, instead of determining the survivor path at every instant for each state, it is determined once in every three symbol durations based on the accumulated path metric for each trajectory. There are only four possible trajectories from instant $i = 3nT$ to instant $i = (3n+3)T$, as shown in Fig. 3.16 (a). Joint NSD and decoding achieves considerable performance gains as will be shown in Section 4.3. The complexity can be reduced by using modified joint NSD and decoding in which the survivor path is determined at instant $i = (3n+1)T$ instead of determining it at $i = (3n+3)T$ as shown in Fig. 3.16 (b). At the subsequent two instants only the branch metric corresponding to the survivor path for the two states is calculated and added to the path metric. This introduces only a negligible performance loss (cf. Fig. 4.19), however, the number of required branch metric calculations per symbol interval reduces to two-third on average.

The normalized Euclidean minimum distance for the modified joint NSD and decoding can be approximated by the difference sequence corresponding to the most likely error event, i.e., {2 2 2 0} (cf. Section 2.2.2). The corresponding curve for $d^2_{\min}(h)/R_c$ is shown

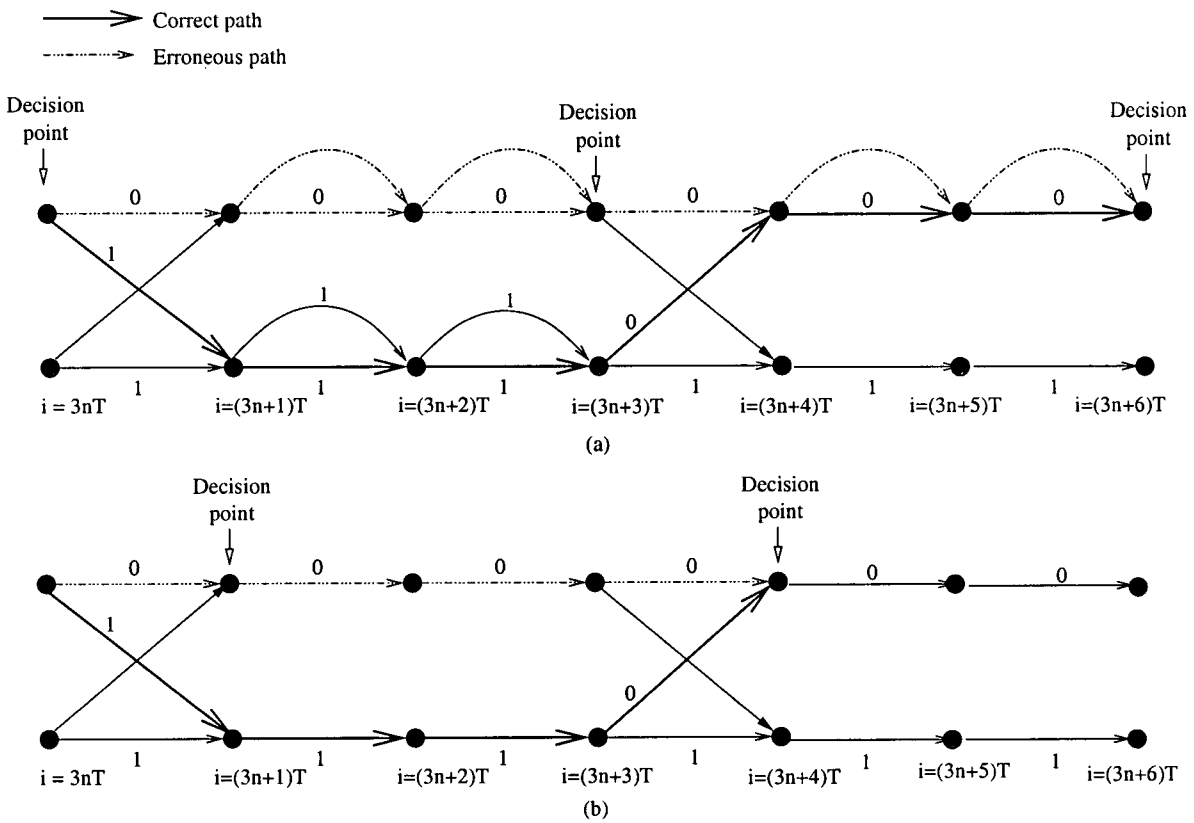

Figure 3.16: (a) Joint NSD and decoding of repetition code with original two-state trellis (b) modified joint NSD and decoding using modified trellis.

in Fig. 3.17. The normalized Euclidean distance squared is increased as compared to the uncoded transmission. For example, for $h = 1/3$ the distance

$$d^2_{\min}(h = 1/3)/R_c = 3.10$$

is obtained, which is 2 units higher than uncoded transmission. As $d^2_{\min}(h)$ corresponds to energy normalized by energy per bit [AAS86], 4.5 dB gain is expected in terms of $10\log(E_s/N_0)$ for $h = 1/3$ with modified joint NSD and decoding. The simulation results of the proposed decoding algorithm will be discussed in Section 4.3.

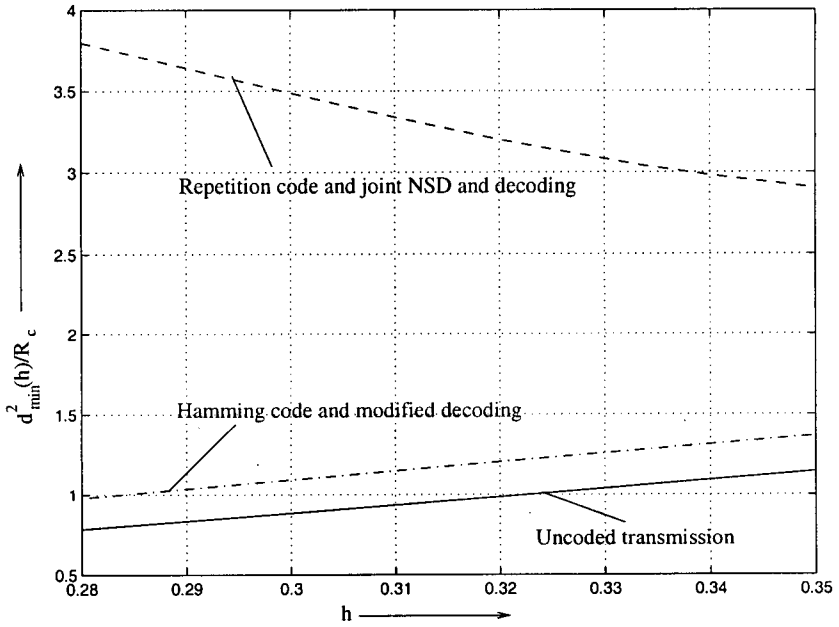

Figure 3.17: Normalized minimum Euclidean distance d^2_{min}/R_c as a function of modulation index h for different coding and decoding schemes.

3.6.3 Modified Decoding for Rate 2/3 HC

For joint decoding of a (n, k) cyclic code over Galois field of order q GF(q), such as the rate 2/3 HC, an alternative and equivalent trellis representation associated with the code is given in [Wol78]. The number of states differs with time with a maximum of $q^{(n-k)}$ states. For the (15,10) expurgated Hamming code specified for Bluetooth systems, the maximum number of states is 32 and on average 34 branch metric calculations per symbol interval are required compared to only 4 in the hard decoding case. Therefore, joint decoding is prohibitively complex for a simple receiver design.

From the error gap analysis given in Section 3.6.1, it is inferred that the channel between the FEC encoder output and decoder input is not memoryless but that burst errors of length two occur with high probability. Based on this observation an improved decoder for the rate 2/3 HC is devised that can correct double errors. This improved decoder is described

in the following para.

The (15,11) HC is strictly a single-error-correcting (SEC) code which can correct 15 error patterns, however, the (15,10) expurgated HC can correct additional 16 error-patterns which can be used to correct errors with Hamming weight larger than one [Bla80, Table 5.1]. This property of the (15,10) HC is utilized to correct highly likely burst-error of length 2. Referred to as a single error correcting-double adjacent error correcting (SEC-DAEC) decoder, it is used to correct error patterns of the type $x^i + x^{i+1}, 0 \leq i \leq 13$. In the simulations, the decoder has been implemented using a syndrome table [Wic95]. The syndrome $\boldsymbol{S}$ for the received vector of 15 symbols $\boldsymbol{R}$ is calculated as $\boldsymbol{S} = \boldsymbol{R} \cdot \boldsymbol{H}^{\mathrm{T}}$. The matrix $\boldsymbol{H}$ is given by $\boldsymbol{H} = [\boldsymbol{I}_{5\times5}|\boldsymbol{P}^{\mathrm{T}}_{10\times5}]$ where $\boldsymbol{I}_{5\times5}$ is the identity matrix and $\boldsymbol{P}_{10\times5}$ is the parity matrix given by [BTS03]

$$\mathbf{P}_{10\times5} = [[11010], [01101], [11100], [01110], [00111], [11001], [10110], [01011], [11111], [10101]]^T.$$

To implement the modified decoding, 9 rows are added to the syndrome table corresponding to 9 DAE events in a code-word of 10 information bits. The modified syndrom table is given in Table 3.2. Since the last five bits in a systematic codeword of 15 bits are parity bits, the error correction is performed over the first 10 bits in a code-word of 15 bits. Therefore, the error patterns for the last five bits are not included in the syndrome table.

Thus, the modified decoding for (15,10) expurgated HC allows to correct a single error and DAE in a block of 15 data symbols. As explained in Section 3.6.1, the next most likely error events are those where the second error event occurs within a block of 15 data symbols with a high probability after the first error followed by a correct data symbol have already been detected. The difference sequence for these incorrigible error events can be approximately given by $\{2\ 0\}$. The minimum distance corresponding to the modified Hamming decoding is shown in Fig. 3.17, which indicates an increase in the squared minimum distance from 1.1 to 1.3 for $h = 1/3$. The minimum ditance for the conventional decoder results

Table 3.2: The modified syndrome table for (15,10) Hamming code.

Error Pattern	Syndrome
1 0 0 0 0 0 0 0 0 0	11010
0 1 0 0 0 0 0 0 0 0	01101
0 0 1 0 0 0 0 0 0 0	11100
0 0 0 1 0 0 0 0 0 0	01110
0 0 0 0 1 0 0 0 0 0	00111
0 0 0 0 0 1 0 0 0 0	11001
0 0 0 0 0 0 1 0 0 0	10110
0 0 0 0 0 0 0 1 0 0	01011
0 0 0 0 0 0 0 0 1 0	11111
0 0 0 0 0 0 0 0 0 1	10101
1 1 0 0 0 0 0 0 0 0	10111
0 1 1 0 0 0 0 0 0 0	10001
0 0 1 1 0 0 0 0 0 0	10010
0 0 0 1 1 0 0 0 0 0	01001
0 0 0 0 1 1 0 0 0 0	11110
0 0 0 0 0 1 1 0 0 0	01111
0 0 0 0 0 0 1 1 0 0	11101
0 0 0 0 0 0 0 1 1 0	10100
0 0 0 0 0 0 0 0 1 1	01010

in the same $d_{\min}(h)$ as uncoded transmission because the most prominent error event is DAE for both the cases. Thus, in terms of $10\log(E_s/N_0)$, a gain of 0.7 dB is expected with modified decoding for HC. The corresponding simulation results are presented in Section 4.3.

3.6.4 LDI Detector with Modified Decoding

Though the LDI detector does not employ sequence detection, the memory of GFSK modulation introduces DAE as may be observed from the EGD shown in Fig. 3.14. It is expected that the proposed modified decoding may be useful for LDI detector as well. For the repetition code, the application of soft decoding does not improve the performance over hard

decoding since the frequency of DAE in the LDI detector output is not as high as for the NSD detector (cf. Section 4.3). However, the application of SEC-DAEC decoding helps to improve the performance of the conventional LDI detectors for Bluetooth devices because of the presence of DAE at the LDI output. This has been confirmed by results shown in Section 4.3. Note that in the case of a memoryless channel no considerable performance gain is achieved by making use of this enhanced error-correcting capability of the (15,10) HC. This is probably the reason why this enhanced capability has not been exploited for the LDI detector in the Bluetooth literature so far.

3.7 Summary of the Proposed Receiver Structure

Fig. 3.18 shows the structure of the receiver designed for Bluetooth devices in the present research work. The proposed receiver is based on the decomposition approach given by

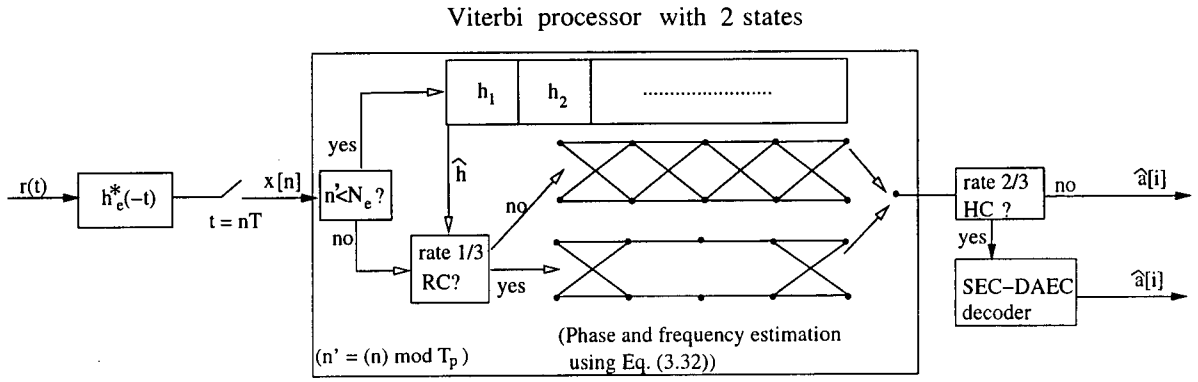

Figure 3.18: Proposed receiver structure.

Rimoldi/Huber&Liu to represent CPM [Rim88][HL89], resulting in a receiver consisting of one filter $h_e^*(-t)$ followed by a Viterbi processor. The novel combined filter $h_e(t)$, given by Eq. (3.21), provides robustness against interference. The filtered received signal is sampled and fed into a two state Viterbi processor. The Viterbi processor employs NSD where the phase is implicitly estimated using the α-metric as described in Section 3.3.2. The frequency

offset estimation using Eq. (3.32) is implemented to provide good performance under high frequency offset conditions. To ensure acceptable performance for all permitted values of h, $0.28 \leq h \leq 0.35$, it is proposed to use adaptive NSD, in which h is estimated using a 25 to 50 symbol estimation period N_e and quantized hypotheses for $h \in \{h_1, h_2, ..., h_{|\mathcal{H}|}\}$. The hypothesis yielding the maximum metric over the estimation period is the estimated $\hat{h}$ which is used to detect the rest of the received signal in a packet. The value of h is estimated for each packet whenever a new packet arrives, i.e., for the packet duration T_p, h is estimated when time instant n satisfies the expression $(n)\text{mod}(T_p) < N_e$. For efficient decoding performance of the rate 1/3 RC, modified joint NSD and decoding is used, for which the Viterbi processor switches to the modified trellis (cf. Fig. 3.18) for calculation of the path metric as described in Section 3.6.2. For the rate 2/3 HC, a modified SEC-DAEC decoder is used after NSD. The performance results for the proposed receiver are discussed in the following chapter.

Chapter 4

Results and Discussion

The performance of the receiver design proposed for Bluetooth devices in the third chapter was simulated using C++ language. The simulation results of the proposed NSD are presented in this chapter, along with a discussion on the performance and a comparison with state-of-the-art techniques. The channel model described in Section 2.1.2 has been used for simulations. Performance under various channel conditions is presented. To get reliable performance results, over 2.5 million information bits are transmitted in each run in blocks of 10000 bits. A minimum of 500 bit errors are observed achieving average percentage deviation of upper and lower limits of 99% confidence interval from the mean of less that 0.1 %.

Initially, in the first section of this chapter, $h = 1/3$ is assumed for the presented performance results as only 6 states are required in the Viterbi processor. The performance for other values of the modulation index is provided wherever found necessary. Section 4.1 gives the performance in the AWGN channel with uncoded transmission for different receiver filters, phase estimation metrics, and numbers of states. Thus in the first section the best combination of these parameters for the proposed receiver is obtained, which is then applied in the following section, where the performance under varying modulation

index conditions and in the presence of interference and frequency offset is considered. In Section 4.3, the performance of coded transmission with different decoding strategies is presented, followed by the performance under Rayleigh and Ricean channels in Section 4.4. The performance results of the proposed receiver in various scenarios are summarized in the concluding section.

4.1 Performance in an AWGN Channel for Uncoded Transmission

The BER performance as a function of $10\log_{10}(E_s/N_0)$ is investigated in an AWGN channel for uncoded transmission with $h = 1/3$ unless stated otherwise. The performance of the proposed receiver is compared with that of the LDI and the MLM-LDI detectors. The LDI receiver is simulated as described in Section 2.3.1. The performance results of the MLM-LDI detector are cited from [SWJ04]. In the rest of this section, the performances for different receiver filters, phase estimation methods, and trellis structures are presented, thus making a selection of the most suitable values for these parameters for the Bluetooth receiver possible.

4.1.1 Filter Selection

The BER performances of filter banks with 1, 2, and 3 matched filters (Eq. (3.13)) and that of the novel filter $h_e(t)$ (Eq. (3.21)) are compared using the receiver structure described in Section 3.1.2 with a signal mapper with 12 signal elements corresponding to $h = 1/3$ and assuming that the channel phase is known at the receiver. The BER vs. $10\log_{10}(E_s/N_0)$ curves for the four different cases are shown in Fig. 4.1. The curves for the LDI detector and the MLSD bound (cf. Eq. (2.25)) are also included for comparison purpose.

The curves for $D = 3$ and $D = 2$ coincide, indicating that there is no performance loss

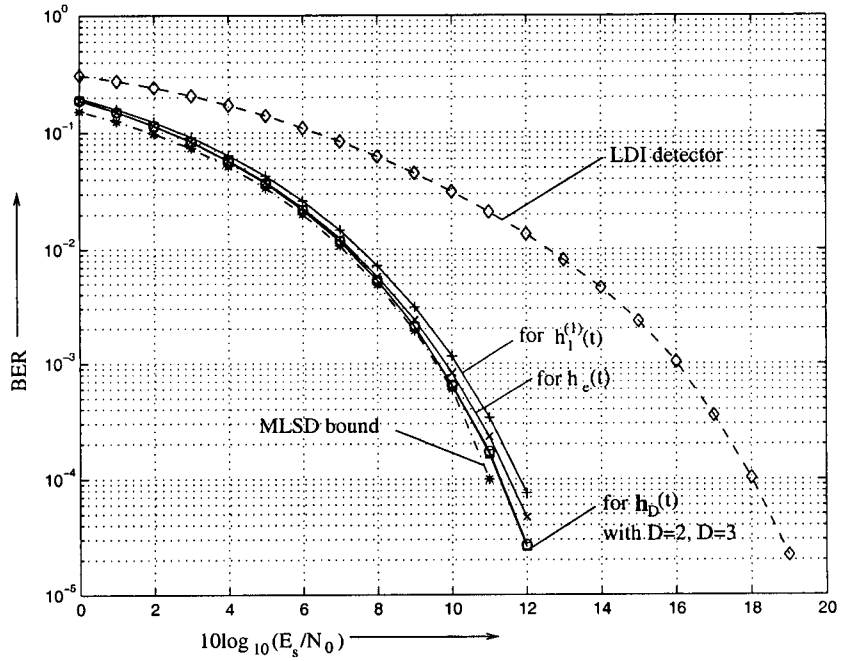

Figure 4.1: Performance comparison of different receiver filters: Coherent detection, full-state trellis, $h = 1/3$, AWGN channel with constant phase.

if the number of matched filters is reduced from 3 to 2. By reducing the dimension of the filter bank to one, $D = 1$, the observed performance loss at BER $= 10^{-3}$ is only approximately 0.5 dB. The high power efficiency with just one filter can be attributed to the high spectral efficiency of GFSK which allows only one basis function to represent the occupied bandwidth with sufficient accuracy. It is also worth noting that the curves closely follow the MLSD bound, indicating a negligible performance loss incurred by the application of alternative representation of CPM proposed by Rimoldi/Huber&Liu [Rim88][HL89] with reduced complexity receiver filters. The performance improves with the new one dimensional filter $h_e(t)$ by approximately 0.25 dB compared to the one dimensional matched filter $h_1^{(1)}(t)$. As the filter set $\boldsymbol{h}_D(t)$ proposed by Huber and Liu [HL89] is only an approximate set of basis functions, the minor improvement obtained using the modified filter $h_e(t)$ is not surprising. Therefore, it is proposed to use the new filter $h_e(t)$ for the novel receiver for Bluetooth devices.

4.1.2 NSD with Implicit Phase Estimation

The performance of NSD using the α-metric and the N-metric is evaluated in this section. The receiver employs one filter with impulse response $h_e(t)$.

The performance of NSD using the N-metric is shown in Fig. 4.2. The performance of NSD improves with increasing window size N, since the channel phase is assumed to be constant.

Fig. 4.3 shows the performance in the presence of phase jitter for $10\log_{10}(E_s/N_0) = 11$ dB. The BER is plotted against $\sigma_\Delta(T)$ where $\sigma_\Delta^2(T)$ denotes the variance of phase jitter. The standard deviation $\sigma_\Delta(T)$ is denoted by σ_Δ in the following discussion. For longer window length N the performance deteriorates at higher phase jitter variance because the assumption of constant channel phase is no longer valid.

The BER vs. $10\log_{10}(E_s/N_0)$ and BER vs. σ_Δ curves for the α-metric are shown in Figs. 4.4 and 4.5, respectively. As α increases the BER performance improves (cf. Fig. 4.4), closely approaching coherent detection performance at $\alpha = 0.95$. However, the deterioration in performance with channel phase variations increases for high α values (cf. Fig. 4.5) as expected. The identical curves for $N = 2$ in Fig. 4.2 and $\alpha = 0.0$ in Fig. 4.4 verifies the theory presented in Section 3.3.2.

The performance of NSD using the N-metric is similar to that of the α-metric as can be inferred by a comparison of Fig. 4.2 with Fig. 4.4 and Fig. 4.3 with Fig. 4.5. However, since the α-metric needs less arithmetic operations compared to the N-metric (cf. Section 3.3), the former will be used in the following discussion on NSD receiver performance. For better power efficiency, a value of α close to one is desirable, however, for robustness against channel phase variations a value of α close to zero is more suitable. Therefore, the appropriate choice of α depends on the channel conditions.

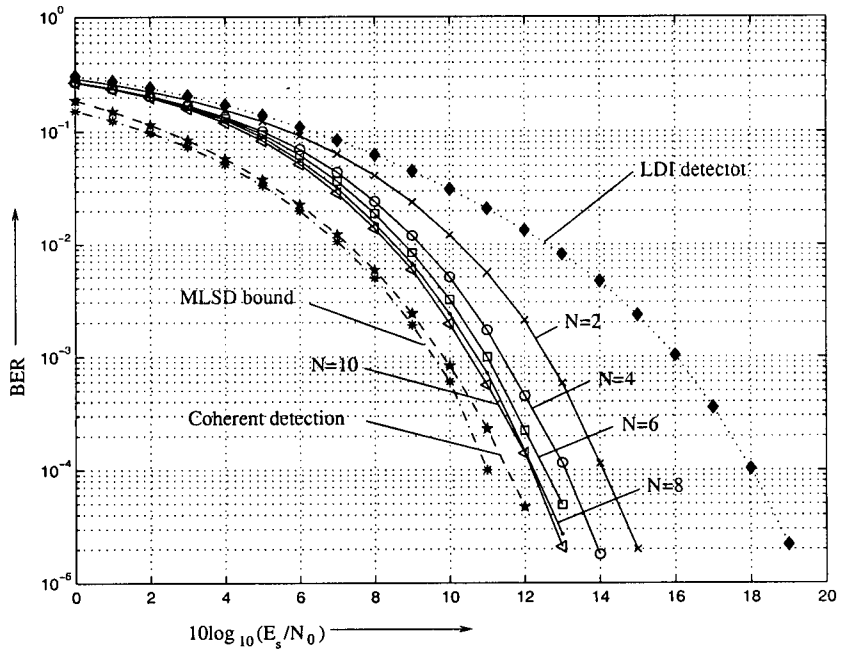

Figure 4.2: Performance of NSD using N-metric with filter $h_e(t)$ and $h = 1/3$ in an AWGN channel with constant phase.

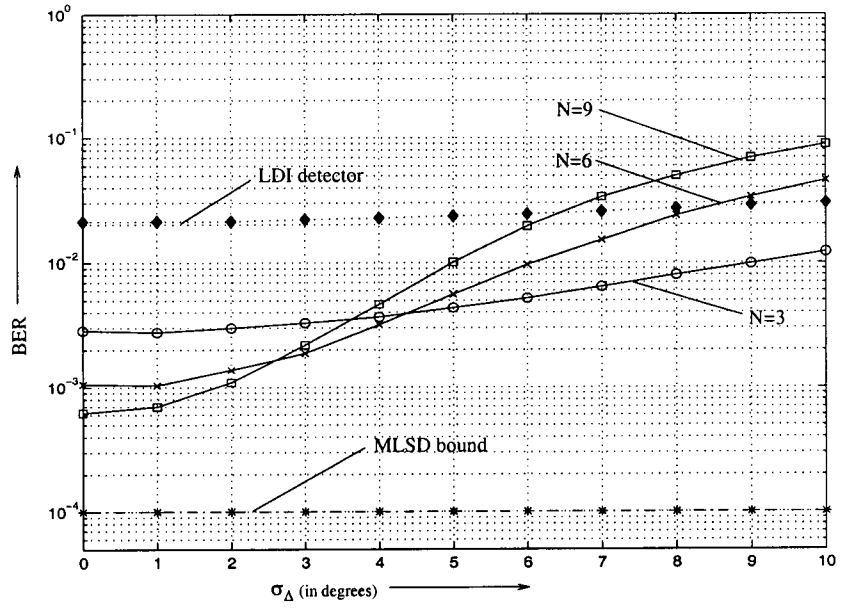

Figure 4.3: Performance of NSD using N-metric in the presence of phase jitter with filter $h_e(t)$ and $h = 1/3$ in an AWGN channel.

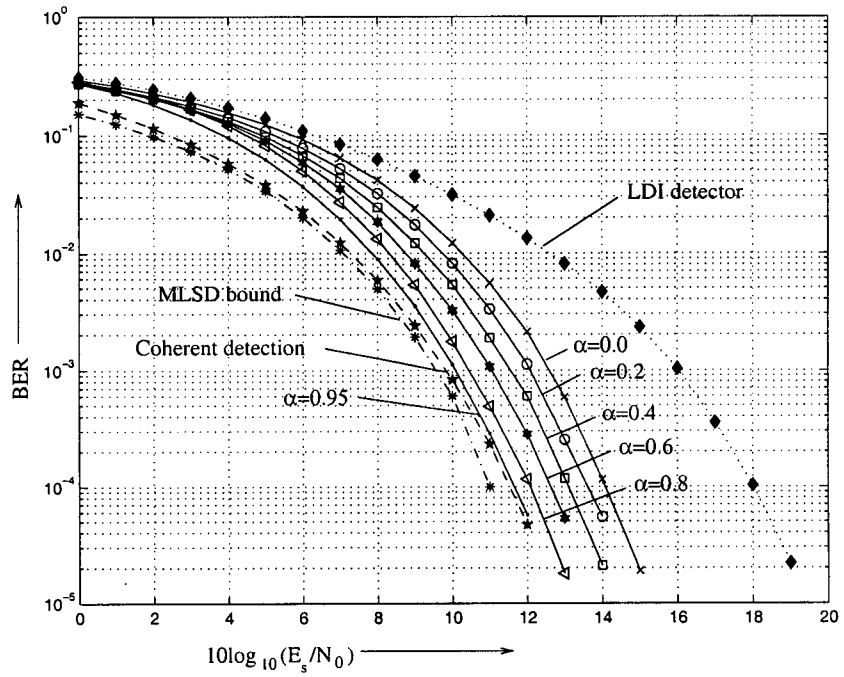

Figure 4.4: Performance of NSD using α-metric with filter $h_e(t)$ and $h = 1/3$ in an AWGN channel with constant phase.

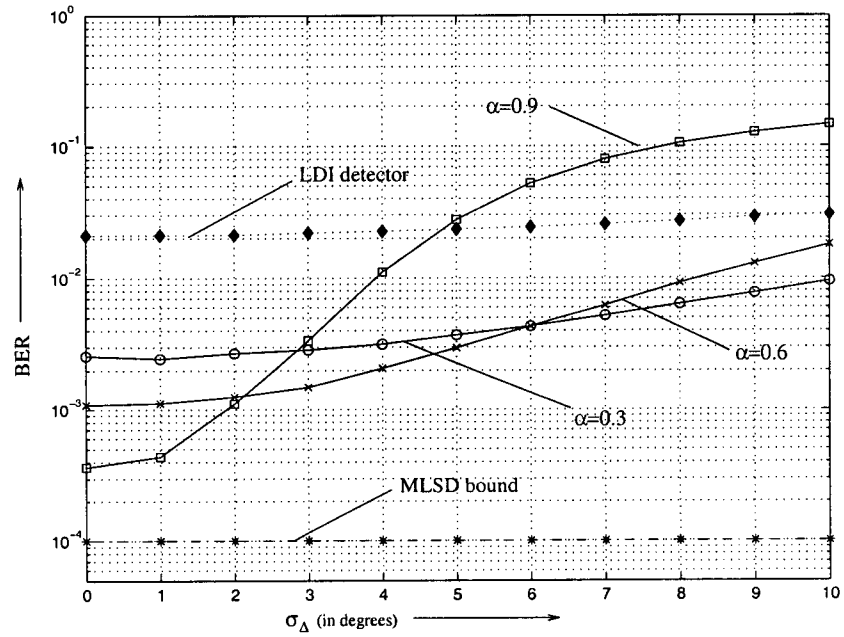

Figure 4.5: Performance of NSD using α-metric in the presence of phase jitter with filter $h_e(t)$ and $h = 1/3$ in an AWGN channel.

4.1.3 State Reduction

The performance with a reduced number of states is compared using coherent detection and a matched filter bank with $D = 3$. Fig. 4.6 shows that the loss in performance with a two-state trellis is negligible compared to a full-state trellis at high E_s/N_0 ratios. This is evident from the fact that at high E_s/N_0 ratios DAEs are the most prominent error events. As explained in Section 3.4, the minimum distance for DAE events remains the same for full-state and two-state trellis which explains the negligible performance loss with the two-state trellis compared to the full-state trellis at high E_s/N_0 ratios. On the other hand, the one-state trellis performance is highly degraded because the minimum distance drops by a factor of 65 compared to the full-state trellis as illustrated by an example in Section 3.4. The performances of NSD with a two-state trellis using one filter $h_e(t)$ and $\alpha = 0.4$ and $\alpha = 0.8$ closely follow the full-state trellis performance as can be observed from a comparison of Fig. 4.6 and Fig. 4.4.

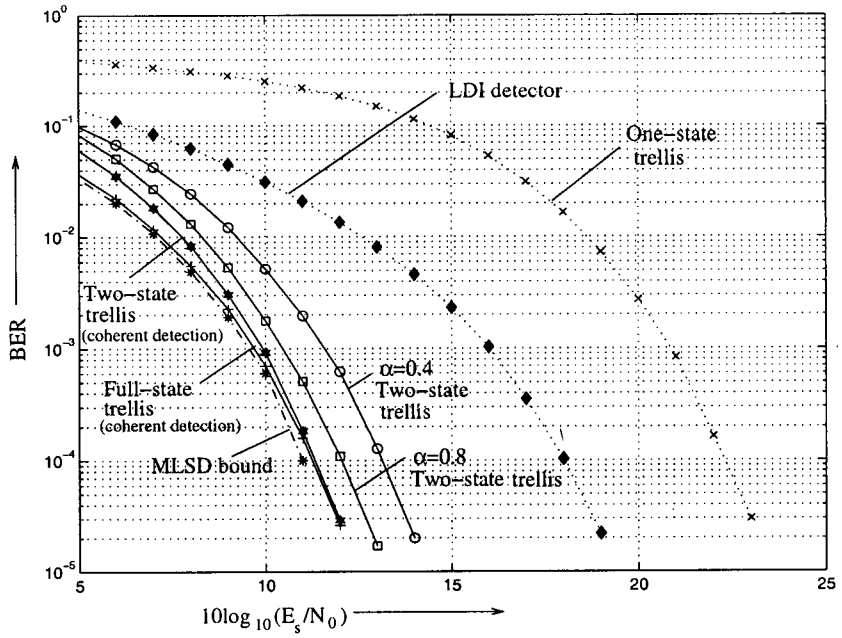

Figure 4.6: Performance with reduced number of states in the Viterbi processor: $h = 1/3$, AWGN channel with constant phase.

The performance of the two-state trellis with the α metric for $h = 0.28$ and $h = 0.35$ is shown in Fig. 4.7. For $h = 0.35$ a full-state Viterbi processor requires 40 states, however, as shown in the graph (cf. Fig. 4.7) the Viterbi processor with only two states gives satisfactory performance. The performance deteriorates with decreasing modulation index since the peak frequency deviation from the carrier frequency decreases [Pro01, Ch. 4]. The corresponding performances of the LDI detector and the MLM-LDI detector are also shown. The proposed receiver is more power efficient than the LDI detector because at BER $= 10^{-3}$ the LDI detector needs 5 to 6 dB more power. The MLM-LDI detector is inferior to the proposed receiver by 1 to 2 dB at BER of 10^{-3}.

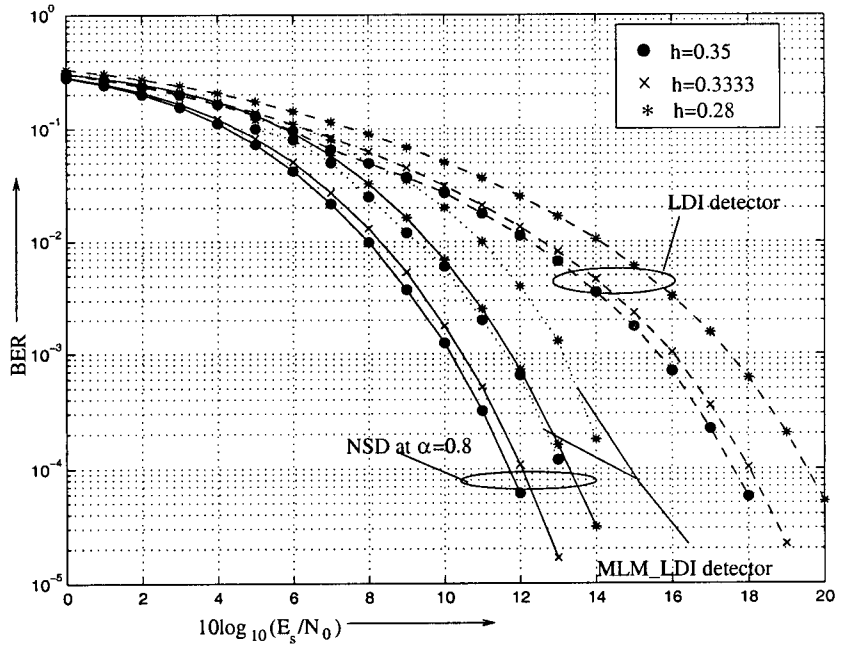

Figure 4.7: Performance comparison of NSD, LDI, and MLM-LDI detectors for different values of h.

4.1.4 Conclusions

From the above discussion, it may be concluded that one receiver filter with impulse response $h_e(t)$ (Eq. (3.21)) provides good performance. NSD with phase estimation using

the α-metric (Eq. (3.30)) with α between 0.4 to 0.8 is very efficient and gives satisfactory results in the presence of phase jitter. The two-state trellis results in a very simple receiver structure irrespective of the value of h with a performance comparable to that of the full-state trellis. Hence, the proposed receiver structure which is used for the further study of the receiver performance in this chapter, consists of one filter $h_e(t)$ followed by a two-state Viterbi processor and employs NSD with implicit phase estimation using the α metric unless mentioned otherwise.

4.2 Performance for Uncoded Transmission

The performance of the proposed receiver is now evaluated under various channel conditions specified in the Bluetooth standard. So far, the performance has been studied only for fixed h in the absence of frequency offset and interference. In this section, these conditions are relaxed. However, only uncoded transmission is considered.

4.2.1 Adaptive NSD Performance

The performance of the proposed receiver for varying modulation indices is now investigated. Fig. 4.8 shows the BER assuming $h = 0.28$, 0.30, 0.3333, and 0.35 at the receiver for $\alpha = 0.8$ at $10\log_{10}(E_s/N_0) = 11$ dB, as a function of the modulation index of the transmitted signal. Figs. 4.9 and 4.10 show the corresponding curves for $\alpha = 0.6$ and 0.4. It may be observed that the performance deteriorates as h at receiver deviates from the h at the transmitter. As the value of α decreases, the performance degradation with deviation from the transmitter h decreases because the mismatched h at receiver introduces frequency variation, and as discussed in Section 3.3.2, the performance deteriorates with increasing α if the channel phase is not constant. Considering for example the results for receiver $h = 0.30$, the observed BER increases by a factor of 10 if the h at transmitter deviates by -0.007 or

+0.012 for $\alpha = 0.8$ (cf. Fig. 4.8). For $\alpha = 0.6$, the range of h broadens as the respective values are -0.02 and +0.035, while for $\alpha = 0.4$ the repective values are -0.02 and +0.05, i.e., the range of h broadens further to $0.28 \leq h \leq 0.35$. Therefore, a lower value of α provides better robustness in case of a varying modulation index. The optimum performance is achieved if h is exactly known at the receiver. The corresponding performance curve is shown for $\alpha = 0.6$ in Fig. 4.9. The deviation from the optimum performance increases with the deviation from the true value of h.

Fig. 4.11 shows the required SNR at BER $= 10^{-3}$ as a function of the modulation index h for (a) the MLSD lower bound, (b) known h at the NSD receiver, (c) 8 cases of fixed h at the NSD receiver and (d) the LDI detector at $h = 1/3$. The number of bits transmitted in the simulations to obtain these curves was reduced to 1 million keeping the minimum observed errors the same as 500. The required E_s/N_0 ratio increases with the deviation from the true value of h as observed before. It can be noted that for $h = 0.31$ at receiver the required $10\log_{10}(E_s/N_0)$ increases by up to 1.0 dB compared to the case of known h at the receiver, when the h at transmitter varies from 0.30 to 0.32.

As a simple solution to estimate h, adaptive NSD was introduced in Section 3.5. The performance of ANSD is shown in Fig. 4.12 for $\alpha = 0.6$ and different numbers of hypotheses $|\mathcal{H}|$ and different estimation periods in symbols N_e. The modulation index h has been quantized in steps of 0.01, except for $h = 0.33$ where $h = 1/3$ has been chosen. Table 4.1 gives the corresponding values of k and p where $h = k/p$. The performance with 8, 4, and 2 hypotheses with estimation period N_e of 50 symbols is shown in Fig. 4.12. To study the effect of decreasing N_e, the performance of ANSD with 8 hypotheses and estimation period of 25 symbols is also shown. If $|\mathcal{H}| = 4$, the $\tilde{h}$ is chosen from the set $\{0.28, 0.30, 0.32, 0.34\}$, while for 2 hypotheses $\tilde{h}$ is either one of $\{0.30, 0.33\}$.

Comparing the curves for $N_e = 50$, it may be observed that the performance with 8

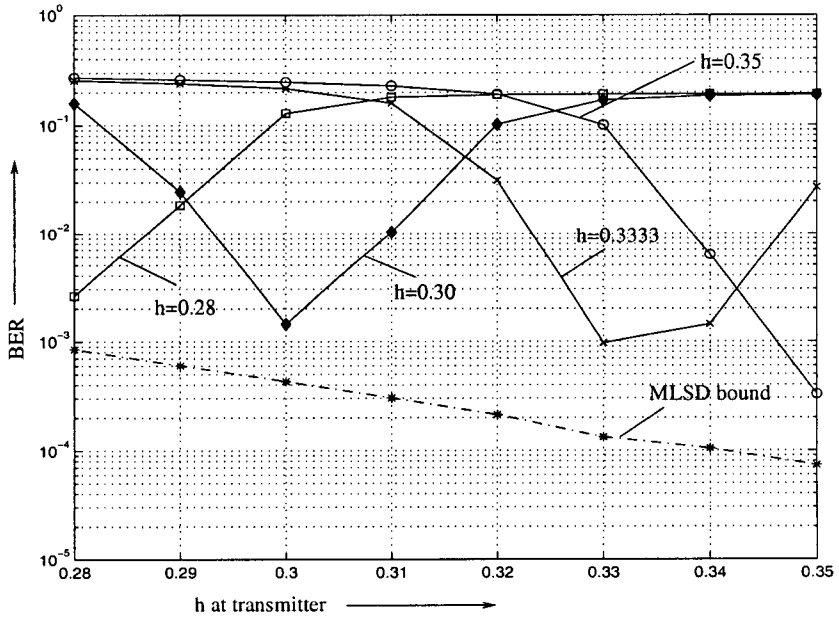

Figure 4.8: Performance of the proposed receiver for varying h with $\alpha = 0.8$ in an AWGN channel with constant phase.

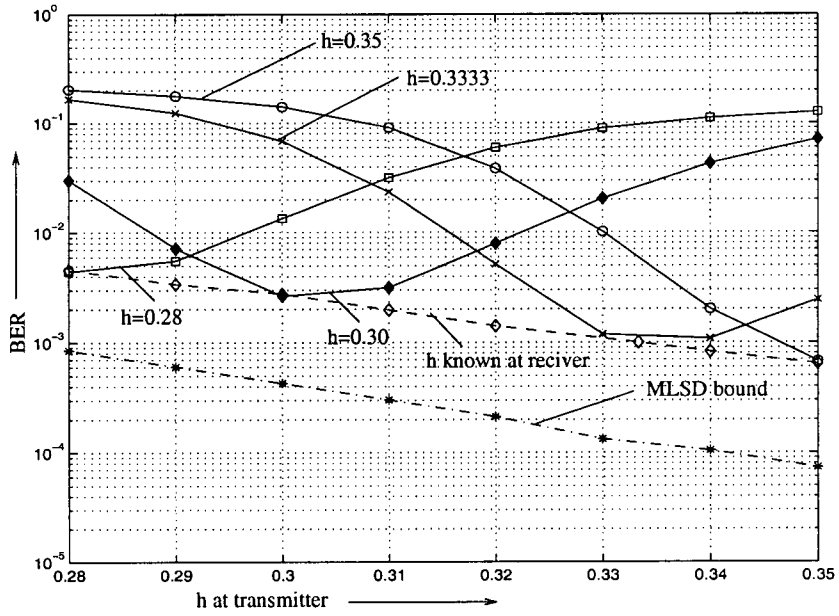

Figure 4.9: Performance of the proposed receiver for varying h with $\alpha = 0.6$ in an AWGN channel with constant phase.

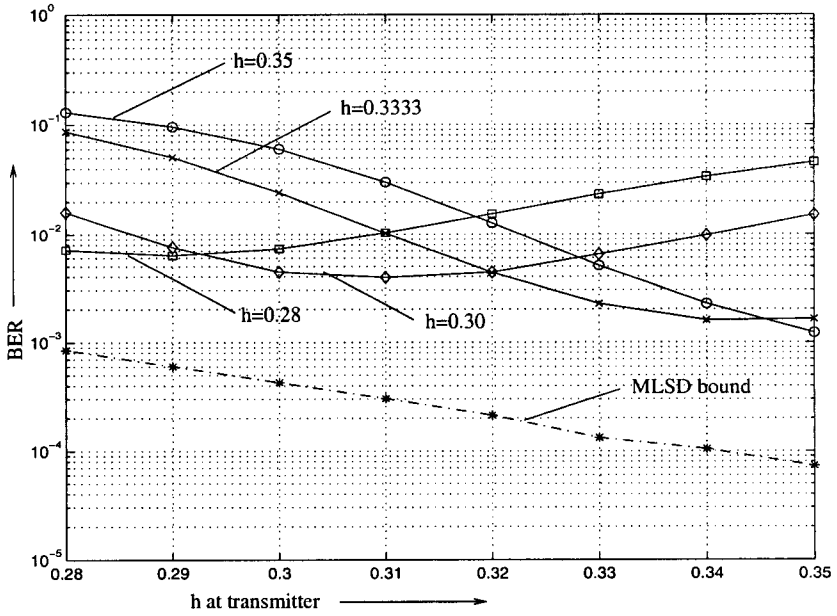

Figure 4.10: Performance of the proposed receiver for varying h with $\alpha = 0.4$ in an AWGN channel with constant phase.

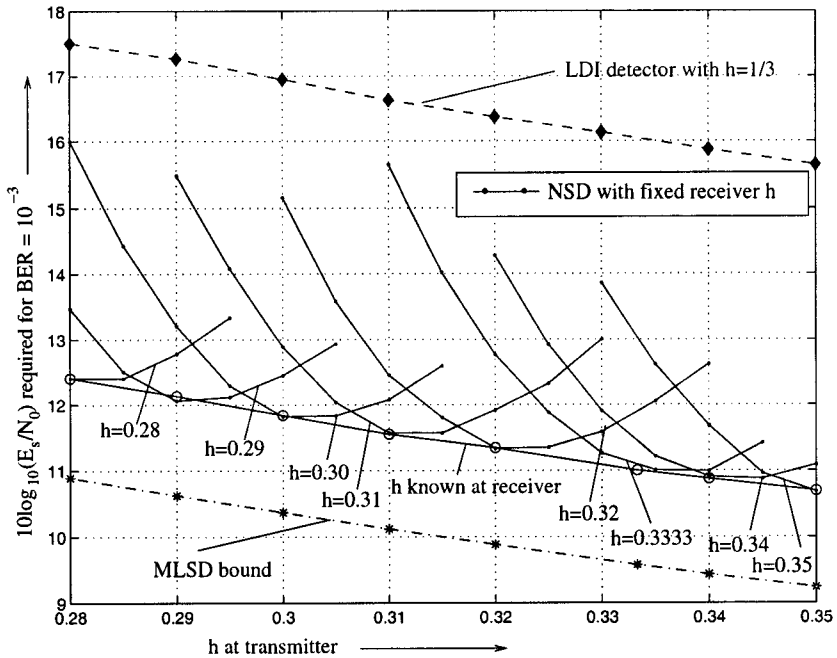

Figure 4.11: The required $10\log_{10}(E_s/N_0)$ for BER $= 10^{-3}$ for the proposed receiver for varying h with $\alpha = 0.6$ in an AWGN channel with constant phase.

Table 4.1: Representation of modulation index h for NSD.

h	0.28	0.29	0.30	0.31	0.32	0.33	0.34	0.35
k/p	7/25	29/100	3/10	31/100	8/25	1/3	17/50	7/20

hypotheses is the best with a maximum deviation of 0.5 dB in the required E_s/N_0 ratio from the optimum performance when h is known at the receiver. For 4 and 2 hypotheses the maximum deviation is 0.75 and 3.5 dB respectively. Since the deterioration in performance is quite high with the deviation of h from its true value, the observed degradation in performance with reduced $|\mathcal{H}|$ is expected. As N_e is reduced to 25 for $|\mathcal{H}| = 8$, the maximum deviation in the required E_s/N_0 ratio from the optimum performance increases to 0.8 dB compared to 0.5 dB for $N_e = 50$.

For further study of the performance of ANSD, $|\mathcal{H}| = 4$ and $N_e = 50$ has been assumed which gives satisfactory performance under varying modulation index conditions. The performance of the LDI detector with h=1/3 with variable h at the transmitter is 4 to 5 dB inferior to the proposed ANSD with $|\mathcal{H}| = 4$ and $N_e = 50$, while ANSD outperforms the MLM-LDI detector by approximately 0.8 dB at $h = 0.28$ and 0.6 dB at $h = 0.35$.

4.2.2 Performance in the Presence of Channel Phase Variations

In practice, Bluetooth devices are required to cope with high frequency offsets Δf and time-variant channel phases. The BER performance of NSD vs. ΔfT at $10\log_{10}(E_s/N_0) = 11$ dB is shown in Fig. 4.13 for $\alpha = 0.9$, 0.6, and 0.3 with $h = 1/3$. It may be observed that for $\alpha = 0.9$ and $\alpha = 0.6$, the BER rapidly increases as ΔfT approaches 0.02, while, the permitted normalized frequency offset ΔfT is 0.1. $\alpha = 0.3$ provides some robustness against frequency offset, but cannot cope with offsets as large as $\Delta f = 100$ kHz. The implementation of Eq. (3.32) with forgetting factor β for frequency estimation alleviates

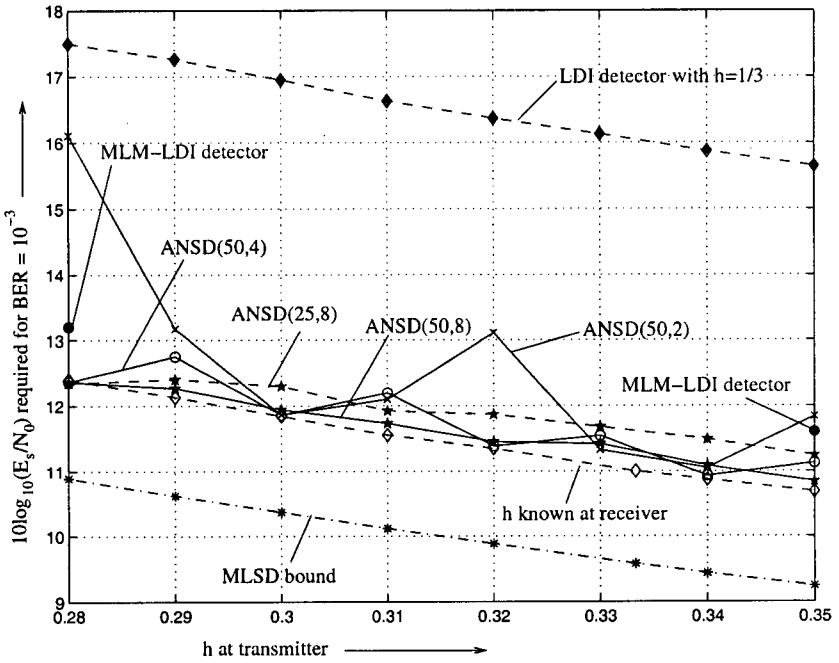

Figure 4.12: Performance comparison of the proposed receiver with ANSD for unknown h with $\alpha = 0.6$ in an AWGN channel with constant phase for different combination of N_e and $|\mathcal{H}|$ represented by ANSD(N_e,$|\mathcal{H}|$).

the effect of frequency offset to a great extent as can be observed from Fig. 4.13. The performance for three values of $\beta = 0.99$, 0.9, and 0.6 are shown in combination with $\alpha = 0.6$. As β approaches one, the performance deteriorates at high ΔfT, and if β is decreased to 0.6 the power efficiency decreases, however, the performance becomes independent of the frequency offset.

For a better comparison, the required $10\log_{10}(E_s/N_0)$ for a BER of 10^{-3} vs. ΔfT is plotted in Fig. 4.14 for $h = 1/3$, where the effect of phase jitter is also included. Eq. (3.30) was used for phase estimation for the curves with $\alpha = 0.6$ and 0.2, while, for the curves with $\alpha = 0.6$ and $\beta = 0.9$ Eq. (3.32) was used for the phase and frequency estimation. The performance of NSD without frequency estimation deteriorates very fast as ΔfT increases. $\alpha = 0.2$ provides better stability compared to $\alpha = 0.6$ because of the presence of a time-varying phase. Furthermore, it is observed that the performance for the implicit phase

estimation according to Eq. (3.32) is almost constant for $0 \leq \Delta fT \leq 0.1$, i.e., it provides the desired stability of the performance of NSD in the presence of high frequency offsets and phase jitter. Increasing σ_Δ from 2° to 5° does not affect the stability of NSD at high frequency offsets, though the required $10\log_{10}(E_s/N_0)$ increases by 0.4 dB. Also, the performance is close to the MLSD bound which presumes perfect synchronization between transmitter and receiver oscillator, hence implying that the proposed frequency estimation technique is very effective in combating the permitted high frequency offsets in Bluetooth devices.

There is a loss in the performance due to the phase noise introduced by frequency estimation according to Eq. (3.32) as can be observed from Fig. 4.15 which has been plotted for $h = 1/3$ and an AWGN with constant channel phase. At BER = 10^{-3}, the application of Eq. (3.32) deteriorates the performance by 1.3 dB with $\beta = 0.6$ and by 0.5 dB for $\beta = 0.9$ compared to the case when Eq. (3.30) is applied for phase reference estimation. For $\beta = 0.99$, there is negligible loss in performance, however, as seen from Fig. 4.13, the performance deteriorates at high frequency offsets. Thus the acceptable stability in the presence of frequency offset is achieved at $\beta = 0.9$ which comes at the expense of 0.5 dB increase in the required E_s/N_0 ratio at BER = 10^{-3}.

The new phase reference estimation using Eq. (3.32) also improves performance of NSD, if h is unknown as shown in Fig. 4.16, where the required $10\log_{10}(E_s/N_0)$ for BER = 10^{-3} is plotted as a function of h for an AWGN channel with constant phase. As seen from the curves drawn for fixed h at the receiver, the deterioration in performance with deviation from the true h is lower than that in Fig. 4.11. For $h = 0.31$ at receiver the required $10\log_{10}(E_s/N_0)$ increases only by up to 0.3 dB compared to the case of known h at the receiver, when the h at transmitter varies from 0.30 to 0.32. As was noted in Section 4.2.1, the corresponding increase is 1.0 dB without frequency estimation. The increase of 0.5

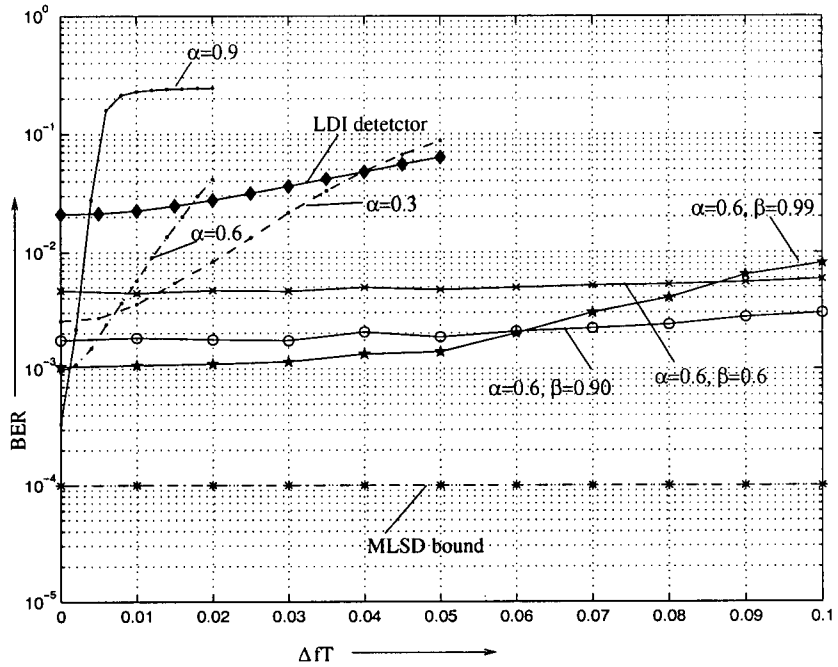

Figure 4.13: Performance of proposed NSD receiver in the presence of frequency offset with $h = 1/3$.

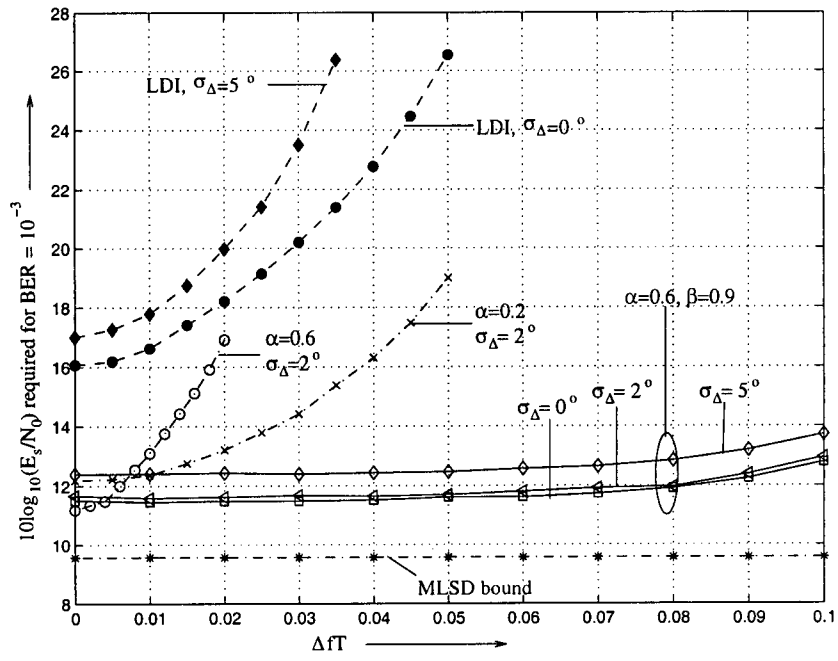

Figure 4.14: Performance of proposed NSD receiver in the presence of frequency offset and phase jitter with variance $\sigma_\Delta^2(T)$.

dB in the required $10\log_{10}(E_s/N_0)$ with the application of frequency estimation technique when h is known at receiver is expected as discussed in the previous paragraph.

The effect of β on ANSD performance in varying h conditions is shown in Fig. 4.17 where the required $10\log_{10}(E_s/N_0)$ for the target BER for ANSD is plotted as a function of h in an AWGN channel with constant phase for different combinations of α and β. The loss in the performance of ANSD with $\alpha = 0.6$ and $\beta = 0.9$, with respect to the performance with known h at receiver is negligible with $|\mathcal{H}| = 4$ and $N_e = 50$, while, the loss is only 0.6 dB with $|\mathcal{H}| = 2$ and $N_e = 50$. As was observed in the previous section the corresponding values for ANSD with $|\mathcal{H}| = 4$ and $|\mathcal{H}| = 2$ without frequency estimation are 0.75 dB and 1.1 dB, respectively. Therefore application of ANSD allows the use of only two hypotheses for a power efficient performance under varying h conditions. Furthermore, comparison of the performance curves of ANSD using Eq. (3.30) with $\alpha = 0.6$ and Eq. (3.32) with $\alpha = 0.6$ and $\beta = 0.9$ in Fig. 4.17 reveals that under varying h conditions with $|\mathcal{H}| = 4$ and $N_e = 50$, the performance of the two is comparable inspite of the phase noise due to Eq. (3.32) in the latter case. From these results the best values for α and β which give good performance under frequency offset and varying modulation index conditions are $\alpha = 0.6$ and $\beta = 0.9$, respectively.

The LDI detector is quite sensitive to frequency offset as can be seen in Figs. 4.13 and 4.14. As the variance of phase jitter increases, the performance of LDI detector becomes even worse. The performance of the LDI detector is approximately 4 dB inferior to ANSD with $\alpha = 0.6$ and $\beta = 0.9$ under varying modulation index conditions. The performance of the MLM-LDI detector at $h = 0.28$ and $h = 0.35$ assuming known h at receiver is inferior to ANSD with $N_e = 50$ and $|\mathcal{H}| = 4$ by less than 0.5 dB as can be observed from Fig. 4.17.

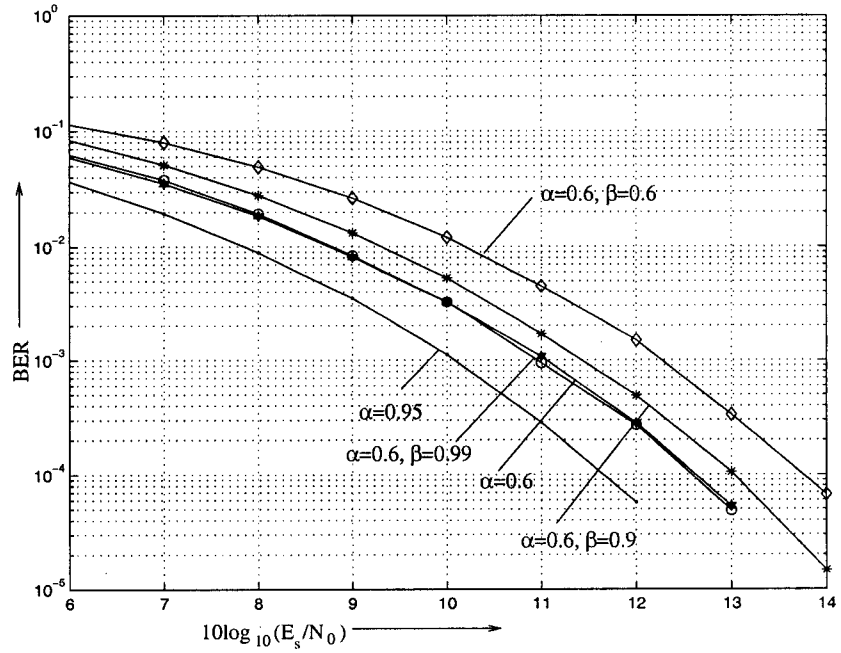

Figure 4.15: Performance of proposed NSD receiver for different values of β with $\alpha = 0.6$ and $h = 1/3$ in an AWGN channel with constant channel phase.

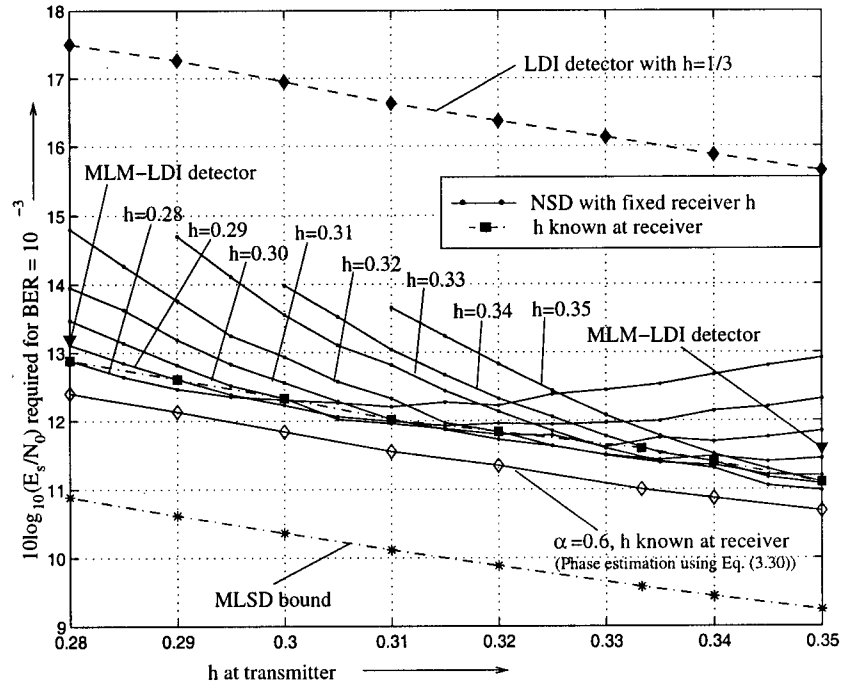

Figure 4.16: Performance the proposed NSD receiver for unknown h in an AWGN channel with constant phase. Eq. (3.32) for phase estimation has been used with $\alpha = 0.6$ and $\beta = 0.9$ if not stated otherwise.

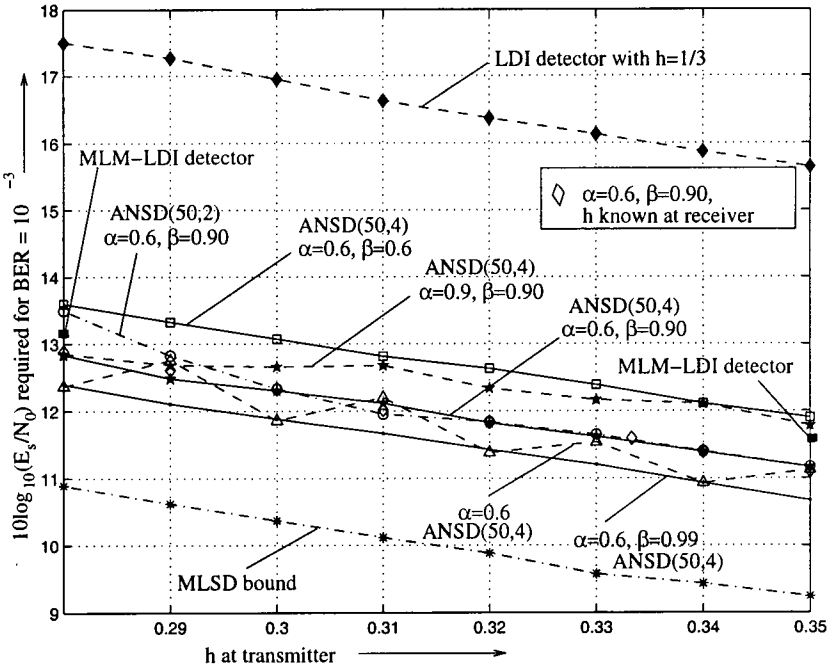

Figure 4.17: Performance of ANSD with $|\mathcal{H}| = 4$, $N_e = 50$ as a function of h in an AWGN channel with constant channel phase.

4.2.3 Performance in the Presence of Interference

The performance of the proposed ANSD in the presence of interference introduced by other Bluetooth devices (cf. Section 2.1.2) is now considered. Fig. 4.18 shows the graphs for required $10\log_{10}(E_s/N_0)$ for BER $= 10^{-3}$ vs. h at transmitter for interferer shifted by $\Delta f_{c,i}$ from the desired signal. $h_e(t)$ is used as receiver filter if not stated otherwise. The power ratios of the desired signal and the interferer are given in Table 2.1. The ANSD parameters are $\alpha = 0.6$, $\beta = 0.9$, $|\mathcal{H}| = 4$, and $N_e = 50$. Since the loss due to interference depends mainly on the filter characteristics, the performance of ANSD in the presence of interference is fairly independent of α and β.

The loss due to adjacent channel interference with the interferer 1, 2 and 3 MHz apart from the desired signal is within 1 dB for the entire range of h. The curves for $\Delta f_{c,i} = 2$ and 3 MHz are coinciding indicating a similar performance of ANSD for these two cases

of ACI. To compare the effectiveness of the applied receiver filter $h_e(t)$ in suppressing ACI with that of the matched filter $h_1^{(1)}(t)$, the performance of $h_1^{(1)}(t)$ is also shown in Fig. 4.18 with $\Delta f_{c,i} = 1$ MHz. The observed performance of matched filter is 1 dB inferior to that of $h_e(t)$, verifying the better effectiveness of $h_e(t)$ in suppressing ACI.

The performance loss experienced in the presence of co-channel interference (CCI) is 4 to 6 dB, which is quite high. The LDI detector also suffers from a high loss of approximately 4 dB in the presence of CCI. For ANSD a low value of $\alpha = 0.2$ helps suppressing CCI as shown in Fig. 4.18 achieving a gain of up to 2 dB compared to $\alpha = 0.6$. Higher values of α provide better phase estimation only if the channel phase is constant. However, the presence of CCI introduces a random time-varying phase, hence, deteriorating the performance at higher values of α.

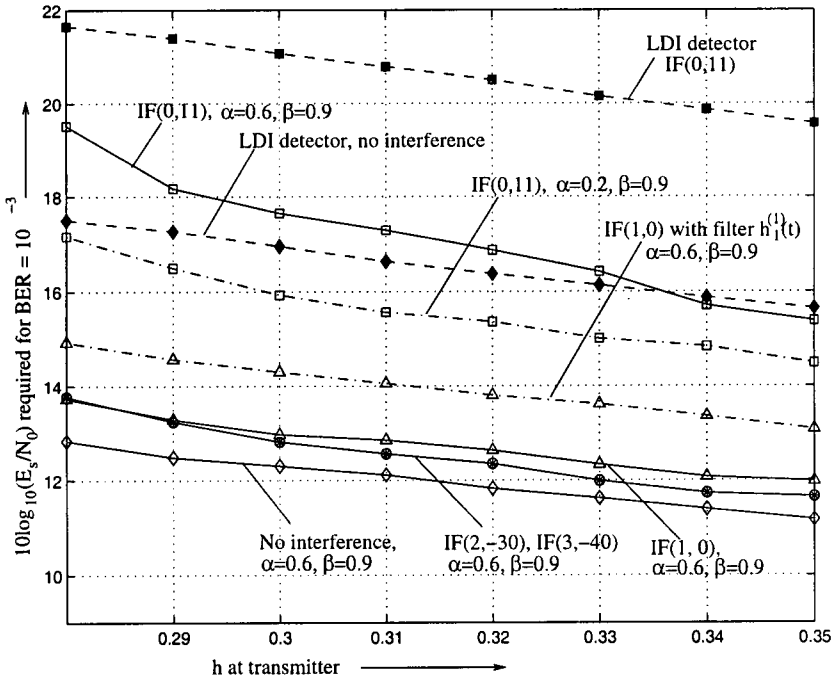

Figure 4.18: Performance of the proposed ANSD with $|\mathcal{H}| = 4$, $N_e = 50$, and $\beta = 0.9$ in the presence of interference using the representation IF($\Delta f_{c,i}$ in MHz,CIR in dB). $h_e(t)$ is used if not stated otherwise.

4.3 Performance with Channel Coding

As discussed in Section 3.6, GFSK modulation memory influences the error-gap distribution and hence, affects the coding performance. The high probability of occurrence of DAEs motivated the application of joint NSD and decoding for the RC and SEC-DAEC decoding for the expurgated HC. The BER performance of NSD with coded transmission and different decoding schemes for the RC and the HC are shown in Figs. 4.19 and 4.20, respectively, with $\alpha = 0.6$, $\beta = 0.9$, and $h = 1/3$. The channel is assumed to be AWGN with constant channel phase.

Fig. 4.19 shows the performance results for repetition coding for (a) the LDI detector with hard decoding, (b) the LDI detector with soft decoding, (c) NSD with hard decoding, (d) NSD with joint decoding, (e) and NSD with modified joint decoding. For comparison, the uncoded transmission results are also included along with the MLSD bounds according to Eq. (2.25). For the MLSD bound for repetition coded transmission $d^2_{\text{min}}(h)/R_c$ for $h = 1/3$ is 3.1 corresponding to the joint NSD and decoding curve in Fig. 3.17.

As observed from Fig. 4.19, at BER $= 10^{-3}$ hard decoding for NSD gives approximately 4 dB performance gain which is further improved by approximately 2 dB using the joint NSD and decoding. The additional gain of 2 dB with joint NSD and decoding is due to the fact that joint NSD and decoding helps to reduce the occurrence of DAE which otherwise is very high (cf. Section 3.6). The performance of the modified joint NSD and decoding which employs the trellis shown in Fig. 3.16 (b) with reduced calculations is only slightly inferior to the original joint NSD and decoding but requires a lower computational complexity, hence suggesting the implementation of modified joint NSD and decoding in the proposed receiver. The performance of NSD closely approaches the corresponding MLSD bound. For the LDI detector, hard decoding achieves the performance gain of approximately 7dB.

Application of soft decoding does not yield any further improvement as the frequency of DAE is not as high as in the case of NSD (cf. Figs. 3.12, 3.14).

The performance results for the expurgated Hamming coded transmission for (a) the LDI detector with SEC decoding, (b) the LDI detector with SEC-DAEC decoding, (c) NSD with SEC decoding and (d) NSD with SEC-DAEC decoding are shown in Fig. 4.20 along with the MLSD bound for SEC-DAEC decoder. The performance gain achieved by the SEC decoder for the NSD receiver is negligible. This is because of the high occurrence of DAE due to the GFSK modulation memory and sequence detection which cannot be corrected by the SEC decoder. Application of SEC-DAEC decoder, however, yields a performance gain of 1 dB. The LDI detector achieves a higher coding gain of approximately 2 dB with SEC decoding because of the higher occurrence of single errors compared to NSD as may be observed from Fig. 3.12. A further performance gain of 1 dB is also achieved for the LDI detector if the SEC-DAEC decoder is applied.

To achieve BER $= 10^{-3}$, the required $10\log_{10}(E_s/N_0)$ for Hamming coded transmission is 10.5 dB, while, for repetition coded transmission it is close to 5.5 dB. In a Bluetooth packet, the packet header is repetition coded, while, the payload is uncoded or Hamming coded except for the HV1 packet type. Therefore, for reliable transmission of the packet payload the minimum required $10\log_{10}(E_s/N_0)$ is 10.5 dB implying that the probability of receiving a corrupted repetition coded packet header is negligibly low.

The proposed receiver outperforms the LDI detector with repetition coded and Hamming coded transmission by 5 dB and 3 dB, respectively. The modified decoding strategies help the proposed receiver to perform better for coded transmission.

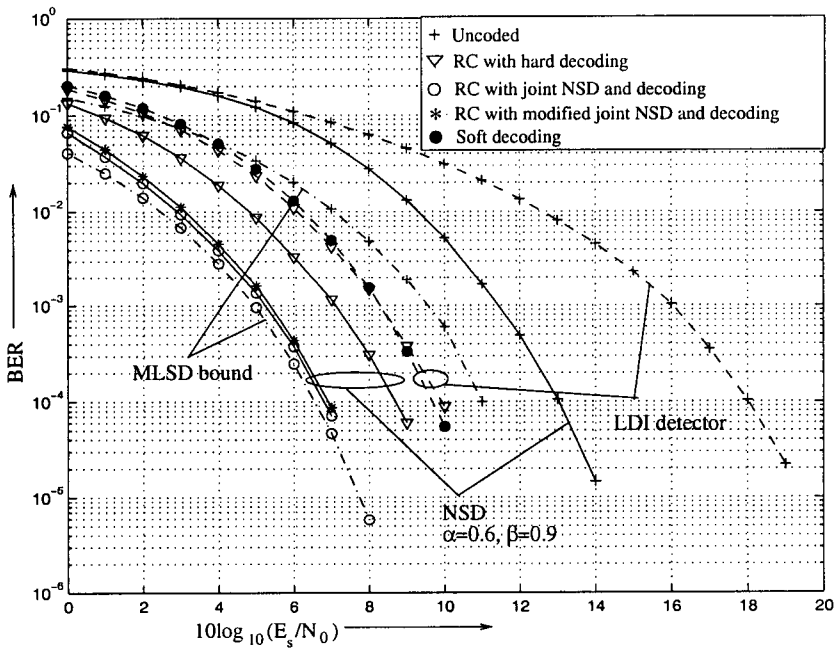

Figure 4.19: Performance of the proposed NSD receiver with $\alpha = 0.6$, $\beta = 0.9$, $h = 1/3$ and rate 1/3 RC for an AWGN channel with constant phase.

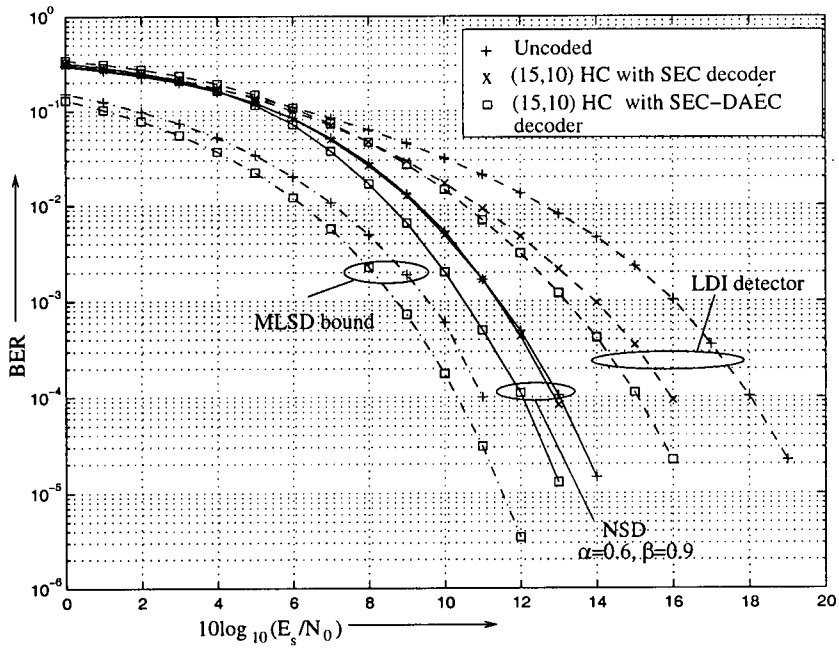

Figure 4.20: Performance of the proposed NSD receiver with $\alpha = 0.6$, $\beta = 0.9$, $h = 1/3$ and (15,10) HC for an AWGN channel with constant phase.

4.4 Packet Transmission over Fading Channel

Finally, the performance of the proposed NSD receiver for fading channels is studied. Since in the channel under consideration individual packets experience static fading, the packet error rate (PER) is the appropriate performance parameter. In the Bluetooth specifications three sizes of payload data packets have been defined, i.e., a packet can occupy a single, three, or five time slots. To observe the behavior of the proposed receiver in fading channels, data medium (DM3) and data high (DH3) packets which occupy three time slots, have been considered. The payload of DM3 packets is protected with the Hamming code, while the payload of DH3 packets is uncoded. The packet length is 976 and 1480 symbols, respectively, excluding packet header and the access code. A minimum of 75 packet errors are observed by transmitting over 1000 packets in each run of the simulation. According to the results in Section 4.3, the repetition coded packet header is safely assumed error free after decoding at the required SNR for reliable transmission of uncoded and Hamming coded payload.

Figs. 4.21, 4.22, and 4.23 depict the simulated PER vs. $10\log_{10}(E_s/N_0)$ for the relevant examples of Rayleigh fading and Ricean fading with Ricean factors of $K = 3$ and 10, respectively. The performance of NSD and the LDI detector are shown for coded and uncoded transmission. A comparison of the performance curves reveals that the gains of the proposed NSD receiver over the LDI detector for the AWGN channel are well reflected in an improved PER for fading channels. NSD receiver outperforms the LDI detector by 5 to 6 dB for uncoded transmission and by approximately 3 dB for Hamming coded transmission. As shown in Fig. 4.21, the performance gains of NSD with SEC decoder over uncoded transmission are small while with the DAEC-SEC decoder gains of up to 1.5 dB are achieved. The LDI detector also shows better gains with the DAEC-SEC decoder over the SEC decoder. The performance gain in Rayleigh faded channel over uncoded transmission is close to 4 dB with the DAEC-SEC decoder, which is 1 dB higher than that with the SEC

decoder (cf. Fig. 4.21). Similar results are observed in the Ricean faded channel with $K = 3$ and 10 in Figs. 4.22 and 4.23, respectively. Hence, the DAEC-SEC decoder is advantageous for the NSD receiver and the LDI detector in the faded channels as well.

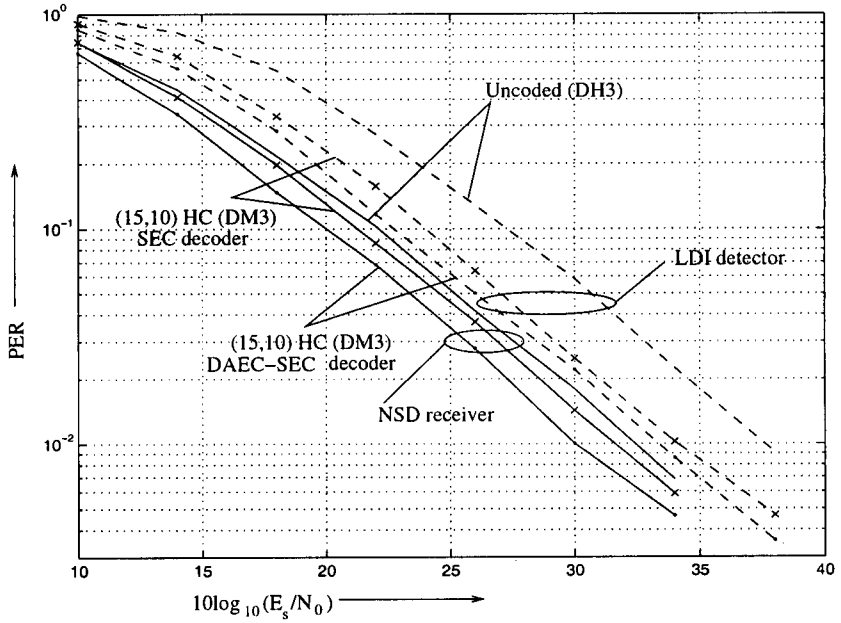

Figure 4.21: Packet error rate in Rayleigh fading channel for DM3 and DH3 packet types [BTS03]. $h = 1/3$, NSD with phase reference (Eq. (3.32)) with $\alpha = 0.6$ and $\beta = 0.9$.

4.5 Summary

The performance results shown in this chapter demonstrate the enhanced power efficiency of the NSD receiver which is directly translated into an increased throughput and/or an improved coverage for Bluetooth systems. The performance of coded and uncoded transmission in (a) the entire range of possible modulation indices h, (b) time-variant channel phase conditions, (c) presence of interference, and (d) fading channels has been investigated. The proposed decomposition based NSD receiver with phase estimation using the α-metric, provides a near optimum performance with a simple receiver structure. The reduction to a two-state trellis achieves the desired modulation-index-invariant trellis with negligible loss

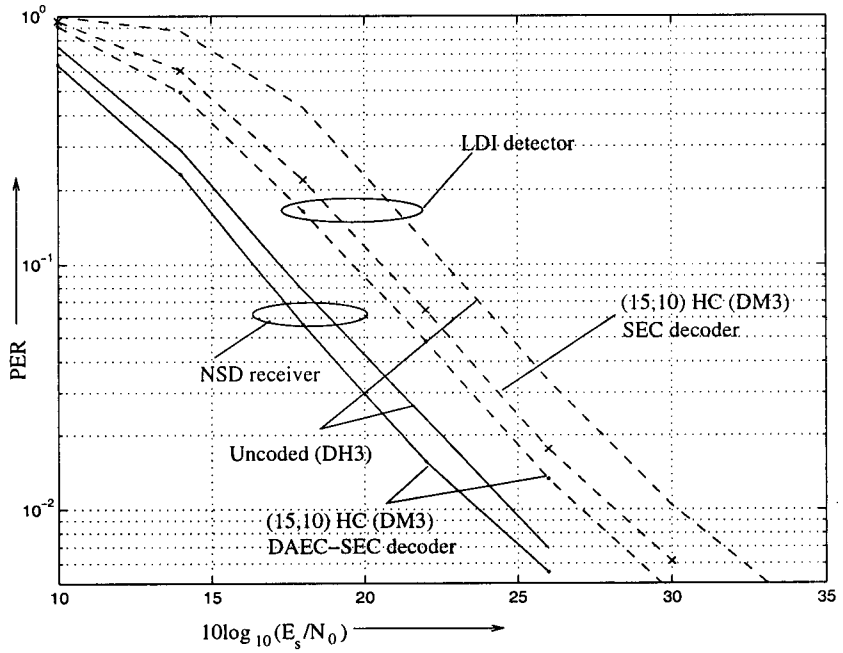

Figure 4.22: Packet error rate in Ricean fading channel with $K = 3$ for DM3 and DH3 packet types [BTS03]. $h = 1/3$, NSD with phase reference (Eq. (3.32)) with $\alpha = 0.6$ and $\beta = 0.9$.

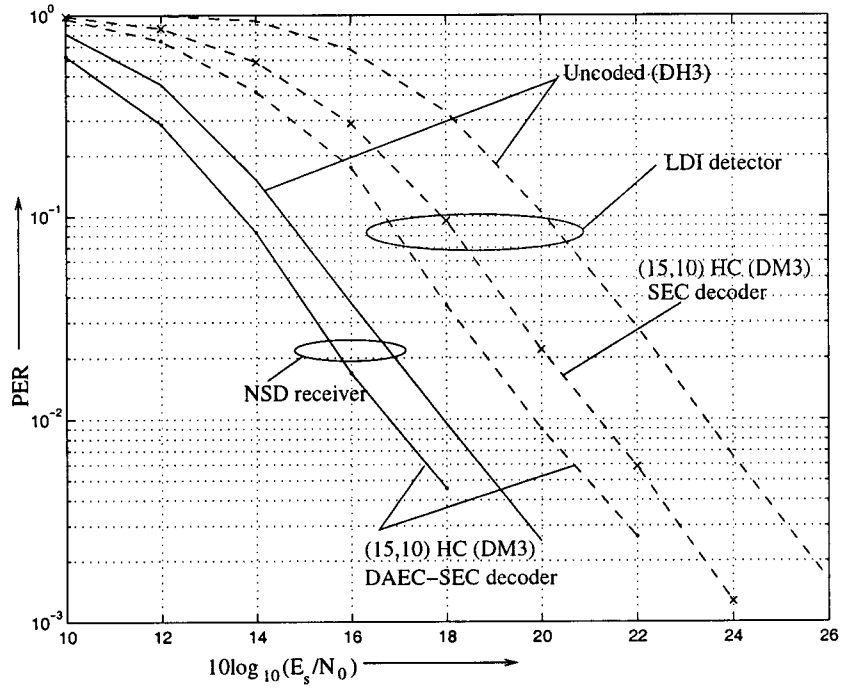

Figure 4.23: Packet error rate in Ricean fading channel with $K = 10$ for DM3 and DH3 packet types [BTS03]. $h = 1/3$, NSD with phase reference (Eq. (3.32)) with $\alpha = 0.6$ and $\beta = 0.9$.

in performance compared to the modulation-index-variant full-state trellis. The novel receiver filter $h_e(t)$ provides better robustness against interference compared to matched filter $h_1^{(1)}(t)$. An increase of 1 dB in the required $10\log_{10}(E_s/N_0)$ is observed in the presence of ACI. Adaptive NSD with just two hypotheses and an estimation period of 50 symbols gives close to optimum performance at the expense of a small increase in the complexity of the receiver. The proposed frequency estimation technique enables excellent performance of the NSD at the high frequency offsets permitted in the Bluetooth systems. However, its application also incurs 0.5 dB loss in performance, which is negligible compared to the gain achieved in the presence of frequency offsets. The modified decoding methods achieve 1 to 2 dB gain in performance compared to the conventional decoding methods, with only negligible added complexity. The proposed receiver outperforms the conventional LDI detector by 3 to 5 dB for typical Bluetooth channels.

Chapter 5

Conclusions and Future Work

5.1 Conclusions

In the present research work, the design of a simple and power-efficient receiver for Bluetooth devices has been investigated. The conventional LDI detector employed in Bluetooth devices provides a very cost-effective and robust receiver solution. However, this receiver is very power-inefficient and it cannot cope with the high frequency offsets of up to ± 100 kHz permitted in Bluetooth systems. Other state-of-the-art techniques which are more power efficient compared to the LDI detector are the MLM-LDI and the coherent MAP receivers. However, these receivers do not meet the requirement of a simple receiver structure. Furthermore, the performances with transmitter h varying from 0.28 to 0.35 and under high frequency offset conditions required for Bluetooth systems have not been investigated for MLM-LDI and MAP receivers.

Considering the practical applicability for Bluetooth devices, the proposed receiver has been designed to achieve (a) high power-efficiency, (b) cost-effective implementation, (c) good performance under varying h conditions, (d) good performance under high frequency offset conditions, (e) effective interference suppression, and (f) efficient decoding for coded transmission. To achieve near-optimum performance the Rimoldi/Huber&Liu decomposi-

tion approach was applied to GFSK, which allows independent desigining of the receiver filter and the Viterbi processor. The proposed receiver consists of one filter, $h_e(t)$, followed by a two-state Viterbi processor. The proposed NSD receiver design and the performance results can be summarized as follows:

- The one-dimensional matched filter $h_1^{(1)}(t)$ proposed by Huber&Liu has been modified by cascading it with a Gaussian pre-filter to obtain the novel filter $h_e(t)$. The modified receiver filter $h_e(t)$ has better stop-band characteristics compared to $h_1^{(1)}(t)$ that are helpful in suppressing ACI. The improved interference suppression ability of $h_e(t)$ is verified by the performance results shown in Fig. 4.18, see also [MLS04], [LSM04].

- A Viterbi processor is employed for noncoherent sequence detection, where the phase is implicitly estimated using the α-metric. A value of α close to one gives near-optimum performance as shown in Fig. 4.4. However, a high value of α cannot cope with the high frequency offsets. A simple and very effective frequency estimation algorithm is devised to provide good performance under high frequency offset conditions. The performance of designed NSD receiver with frequency estimation using Eq. (3.33) is almost independent of the frequency offset as shown in Fig. 4.14, see also [MLS04], [LSM04].

- The number of states in the Viterbi processor is reduced to 2 from $2p$ by applying per-survivor processing, thereby transforming the modulation-index-variant trellis structure into a modulation-index-invariant trellis. The performance loss incurred due to state reduction is negligible (cf. Fig. 4.6), however, the complexity of the receiver is reduced to a great extent.

- To ensure good performance when the modulation index h at the transmitter is unknown at the receiver, an h estimation algorithm is devised which estimates h based

on the best path metrics for a duration of 50 symbols for 2 to 4 hypotheses of h. At the expense of a small added complexity, the adaptive NSD allows for fast adaptation of NSD to the actually used h, cf. Fig. 4.17, [MLS04], and [LSM04].

- For efficient decoding of coded transmission, modified decoding strategies are suggested which specifically address the high occurrence of DAE due to the memory introduced by the GFSK modulation. For repetition coded transmission it is proposed to perform modified joint NSD and decoding that provides close to 2 dB gain at a BER of 10^{-3} (cf. Fig. 4.19) over a conventional hard decoding. A modified decoding algorithm for (15,10) Hamming coded transmission provides approximately 1 dB gain in performance to achieve 10^{-3} BER with only negligible added complexity, cf. Fig. 4.20, [MLS04], and [LSM04].

The performance results under typical channel conditions for Bluetooth systems show that the proposed NSD receiver outperforms the LDI detector by 3 to 5 dB for coded and uncoded transmission. Furthermore, the designed receiver has a simpler structure compared to the MLM-LDI detector and it outperforms the MLM-LDI detector by 0.5 to 1 dB. The performance of the NSD receiver for high frequency offsets is better than that of any of the state-of-the-art techniques for Bluetooth receivers available in literature. Therefore, the present receiver design is an attractive solution for low-complexity yet power-efficient Bluetooth devices.

The proposed modified decoding scheme for the (15,10) Hamming code also enhances the performance of the LDI detector by 1 dB. As the implementation of the designed decoder does not demand any substantial increase in complexity, the improved decoding method can benefit current Bluetooth devices that employ LDI detectors, at no extra cost, cf. [LMS04a], [LMS04b].

5.2 Recommendations for Future Work

- For practical applicability of the proposed NSD receiver, it is suggested to develop a cost-effective hardware implementation.
- The interference from co-existing WLAN networks may be investigated as both Bluetooth and WLANs operate in the ISM band.
- The coherent MAP receiver, which employs Laurent's decomposition approach to GFSK, also shows high performance gains over the LDI detector. The application of implicit phase estimation and the proposed estimation algorithms for h and the frequency offset to the MAP receiver may be considered in future research on Bluetooth systems.

Glossary

Abbreviations

ACL	Asynchronous Connectionless
ANSD	Adaptive Noncoherent Sequence Detection
ARQ	Automatic Repeat Request
AWGN	Additive White Gaussian Noise
BER	Bit Error Rate
BSC	Binary Symmetric Channel
CIR	Carrier to Interferer (power) Ratio
CPM	Continuous Phase Modulation
CRC	Cyclic Redundancy Check
DAE	Double Adjacent Error
DH	Data High rate (packet)
DM	Data Medium rate(packet)
DV	Data Voice (packet)
ECB	Equivalent Complex Baseband
EGD	Error Gap Distribution
FCC	Federal Communications Commission
FEC	Forward Error Correction
FHS	Frequency Hop Synchronization
FHSS	Frequency Hopping Spread Spectrum
GFSK	Gaussian Frequency Shift Keying
HC	Hamming Coding
HV	High Quality Voice (packet)
FEC	Forward Error Correction
I&D	Integrate and Dump
ISI	Inter-Symbol Interference
ISM	Industrial, Scientific and Medical
LDI	Limiter Discriminator Integrate & Dump

LOS	Line of Sight
MAP	Maximum a Posteriori Probability
Mbps	Mega bits per second
MLM	Max-Log-Maximum likelihood
MLSD	Maximum Likelihood Sequence Detection
NSD	Noncoherent Sequence Detection
PER	Packet Error Rate
PSP	Per Survivor Processing
RC	Repetition Coding
SCO	Synchronous Connection Oriented
SEC	Single Error Correcting
SEC-DAEC	Single Error Correcting-Double Adjacent Error Correcting
SD	Sequence Estimation
SIG	Special Interest Group
SNR	Signal to Noise (power) Ratio
VA	Viterbi Algorithm
WER	Word Error Rate
WLAN	Wireless Local Area Network
WPAN	Wireless Personal Area Network

Variables

α	Forgetting factor for phase estimation using Eq. (3.30)
β	Forgetting factor for frequency estimation using Eq. (3.34)
$\phi(t, \boldsymbol{a})$	Information carrying CPM phase
ϕ_0	Constant channel phase
$\phi_c(t)$	Time varying channel phase
$\Phi(t, \boldsymbol{a})$	Phase of the CPM signal modulated by information bits $\boldsymbol{a}$
$\psi(t, \boldsymbol{b})$	Modified information carrying phase
$\Delta\phi_c(t, \tau)$	Phase jitter
$\sigma_\Delta \equiv \sigma_\Delta(T)$	Standard deviation of phase jitter in degrees
$\theta[n-L]$	Phase state at time instant nT
$\Psi[n-L]$	Modified normalised phase state at time instant nT
$\boldsymbol{\rho}(\tilde{\boldsymbol{d}}[i])$	Vector of D elements representing correlation of signal elements $\rho(t, \tilde{\boldsymbol{d}}[i])$ with the matched filters $\boldsymbol{h}_D(t)$ multiplied by matrix $\boldsymbol{C}^{-1}$ (cf. Eq. (3.16))
$\rho(t, \boldsymbol{d}[i])$	Signal element corresponding to address vector $\boldsymbol{d}[i]$
$\lambda[i]$	Branch metric at instant iT
$\Lambda[i]$	Sequence metric at instant iT
γ_N	Difference sequence of two sequences of data symbols of length N
$\boldsymbol{a}$	Input binary data stream of bits, $a[i] \in \{\pm 1\}$
$\hat{\boldsymbol{a}}$	Estimated binary bit stream, $\hat{a}[i] \in \{\pm 1\}$
$\boldsymbol{b}$	Unipolar information sequence, $b[i] \in \{0, 1\}$
BT	Time bandwidth product
D	Dimension of the filter bank at the receiver front end
$\boldsymbol{d}[i]$	Address vector of $L+1$ coordinates corresponding to a signal element at instant iT,$\boldsymbol{d}[i] = \{\Psi[n-L+1],\, b[i-L], ..., b[i]\}$
$\tilde{\boldsymbol{d}}[i]$	Address vector corresponding to a hypothetical information sequence
$\hat{\boldsymbol{d}}[i]$	Address vector corresponding to the estimated information sequence
$d_{\min}$	Minimum Euclidean distance between two sequences
$d_{\min}(h)$	Upper bound for minimum Euclidean distance between two sequences as a function of h
E_s	Average signal energy per transmitted information symbol

f_c	Passband carrier frequency
f_r	Reference carrier frequency
Δf	Frequency offset between transmitter and receiver
$\Delta f_{c,i}$	Frequency offset of the interferer from carrier
g	Static fading gain
$g(t)$	CPM frequency baseband pulse
$h = k/p$	Modulation index for CPM where k and p are relatively prime integers
$\tilde{h}$	Hypothetical Modulation index
$\hat{h}$	Estimated Modulation index
$\mathcal{H}$	Set of hypothetical modulation indices
$\boldsymbol{h}_D(t)$	Impulse reponse of the bank of matched filter at the receiver with dimension D, $\boldsymbol{h}_D(t) = \{h_D^{(1)}, ..., h_D^{(D)}\}$
$h_e(t)$	Impulse reponse of the novel filter given by Eq. (3.21)
$i(t)$	Collective interferecnce
K	Ricean factor
L	Phase memory in terms of information symbols
M	Modulation level
N_0	Single sided power spectral density of noise
N_e	Estimation period in symbols for ANSD
$n(t)$	Continuous time complex baseband white Gaussain noise process
$q(t)$	Baseband phase response (phase pulse) for CPM
$q_{\text{ref}}[i]$	Estimated phase reference at instant iT
$q_{\text{ref}}^{\alpha}[i]$	Phase reference at instant iT estimated using α-metric and Eq. (3.30) or Eq. (3.32)
$q_{\text{ref}}^{N}[i]$	Phase reference at instant iT estimated using N-metric
R_c	Code rate
$r(t)$	Noisy random-phase complex baseband receiver signal
$s(t, \boldsymbol{a})$	Complex baseband transmitted signal corresponding to information sequence $\boldsymbol{a}$
$s(t, \boldsymbol{d})$	Complex baseband transmitted signal corresponding to sequence of address vectors $\boldsymbol{d}$
$\boldsymbol{S}_n$	State vector for full-state trellis at time instant nT

$\boldsymbol{S}_n^1$	State vector for one-state trellis at instant nT
$\boldsymbol{S}_n^2$	State vector for two-state trellis at instant nT
$s_{\mathrm{RF}}(t)$	Passband transmitted signal
t	Continuous time
T	Modulation interval
T_d	Root mean square delay spread introduced by channel
T_p	Packet duration
$\boldsymbol{x}[i]$	Vector of D elements representing filtered samples of $r(t)$ at time instant iT, $\boldsymbol{x}[i] = \{x_1[i], ..., x_D[i]\}$

Definitions

$\ln x$	Natural logarithm of x
$\lceil . \rceil$	Ceiling function
$\bar{a}[i]$	Complement of $a[i]$
$I_0(x) = \frac{1}{2\pi} \int_{-\pi}^{\pi} e^{x\cos(\psi)} d\psi$	Zeroth order modified Bessel function of the first kind
$\boldsymbol{x}^T$	Transpose of matrix $\boldsymbol{x}$
x^*	Complex congulate of x
$\boldsymbol{x}^H = \boldsymbol{x}^{T*}$	Hermitian transpose of matrix $\boldsymbol{x}$
$\Re\{x\}$	Real part of the complex number x
$Q(t) = 1/\sqrt{2\pi} \int_t^{\infty} \mathrm{e}^{-\tau^2/2} \mathrm{d}\tau$	The standard Gaussian Q function
$x(t) * y(t) = \int_{-\infty}^{\infty} x(\tau) y(t-\tau) d\tau$	Continuous-time convolution of the functions $x(t)$ with $y(t)$
$x[i] * y[i] = \sum_{k=-\infty}^{k=\infty} x[k] y[i-k]$	Discrete-time convolution of the functions $x[i]$ with $y[i]$

Bibliography

[AAS86] J. B. Anderson, T. Aulin, and C.-E. Sundberg. Digital Phase Modulation. *Plenum Press, New York*, 1986.

[AFK72] J.-P. A. Adoul, B. D. Fritchman, and L. N. Kanal. A critical statistic for channels with memory. *IEEE Transactions on Information Theory*, 18(1):133-141, January 1972.

[ARS81] T. Aulin, N. Rydbeck and C.-E. Sundberg. Continuous phase modulation - part II: partial response signaling. *IEEE Transactions on Communications*, 29(3):210-225, March 1981.

[AS81] T. Aulin and C.-E. Sundberg. Continuous phase modulation - part I: full response signaling. *IEEE Transactions on Communications*, 29(3):196-209, March 1981.

[Bis01] C. Bisdikian. An overview of the Bluetooth wireless technology. *IEEE Communications Magazine*, pp:86-94, December 2001.

[Bla80] Richard E. Blahut. Theory and practice of error control codes. *Addison-Wesley, Reading, Massachusetts*, 1983.

[BT.com] The official Bluetooth website: *http://www.bluetooth.com/news/index.asp?A=2&PID=479.* Big Future For Bluetooth. BBC On line, January 16, 2003.

[BT.org] The official Bluetooth membership site: *http://www.bluetooth.org.*

[BTS03] Bluetooth special interest group. Specifications of the Bluetooth system, Version 1.2. November 2003.

[CR98] G. Colavolpe and R. Raheli. Noncoherent sequence detection of continuous phase modulations. In *Proceedings of IEEE Global Telecommunications Conference*, 1:556-561, November 1998.

[CR99] G. Colavolpe and R. Raheli. Noncoherent sequence detection. *IEEE Transactions on Communications*, 47(9):1303-1307, September 1999.

[CR02] G. Colavalpe and R. Raheli. Detection of linear modulations in the presence of strong phase and frequency instabilities. *IEEE Transactions on Communications*, 50(10):1617-1626, October 2002.

[DMR00] A. Demir, A. Mehrotra, and J. Roychowdhury. Phase noise in oscillators: A unifying theory and numerical methods for characterization. *IEEE Transactions on Circuits and Systems*, 47(5):655-674, May 2000.

[FCC] FCC 47 Code of Federal Regulations (CFR), October 1, 1993 Edition

[HL89] J. Huber and W. Liu. An alternative approach to reduced-complexity CPM receivers. *IEEE Journal on Selected Areas in Communications*, 7(9):1437-1449, December 1989.

[HL01] S. Hong and Y.-H. Lee. Fractionally-spaced differential detection of GFSK signals with small *h*. *IEICE Transactions on Communications*, E84-B(12):3226-3234, December 2001.

[JNG02] W. Jia, A. Nallanathan, and H. K. Garg. Performance of a Bluetooth system in multipath fading channels with interference. In *International Workshop*

on Mobile and Wireless Communications Network, pp:579-582, September 2002.

[JSP96] G. J. M. Janssen, P. A. Stigter, and R. Prasad. Wideband indoor channel measurements and BER analysis of frequency selective multi-path channels at 2.4, 4.75 and 11.5 GHz. *IEEE Transactions on Communications*, 44(10):1272-1288, October 1996.

[Kay89] S. Kay. A fast and accurate single frequency estimator. *IEEE Transactions on Acoustics, Speech, Signal Processing*, 37(12):1987-1990, December 1989.

[KB90] W. Koch and A. Baier. Optimum and sub-optimum detection of coded data disturbed by time-varying intersymbol interference. In *Proceedings of IEEE Global Telecommunications Conference*, 3:1679-1684, 1990.

[Lau86] P. A. Laurent. Exact and approximate construction of digital phase modulations by superimposition of amplitude modulated pulses (AMP). *IEEE Transactions on Communications*, 34(2):150-160, Februrary 1986.

[LDF93] C.-L. Liu, W. S. Djen, and K. Feher. A low-cost dual-mode noncoherent receiver with robust frequency-offset compensation. In *Proceedings of IEEE Vehicular Technology Conference*, pp:412-415, May 1993.

[Liu90] W. Liu. Complexity reduction of coherent receivers for digital continuous phase modulation. Dissertation in Fachbereich Elektrotechnik, Universität der Bundeswehr München, 1990.

[LMS04a] L. Lampe, M. Jain, and R. Schober. Improved decoding for Bluetooth systems. *To be published in IEEE Transactions on Communications*, 2004.

[LMS04b] L. Lampe, M. Jain, and R. Schober. Improved decoding for Bluetooth systems. *Submitted to IEEE International Conference on Communications (ICC) '05*, July 2004.

[LSEH01] L. Lampe, R. Schober, G. Enzner, and J. Huber. Noncoherent coded continuous phase modulation. In *Proceedings of IEEE International Conference on Communications (ICC)*, pp:2216-2220, June 2001.

[LSM04] L. Lampe, R. Schober, and M. Jain. Noncoherent sequence detection receiver for Bluetooth systems. *Submitted to IEEE Journal on Selected Areas in Communications*, April 2004.

[LVNKM03] H. Liu, V. Venkatesan, C. Nilsen, R. Kyker, and M. E. Magaña. Performance of frequency hopped noncoherent GFSK in correlated Rayleigh fading channels. In *Proceedings of IEEE International Conference on Communications (ICC)*, 4:2779-2783, May 2003.

[MLS04] M. Jain, L. Lampe, and R. Schober. Sequence detection for Bluetooth systems. *To be presented in IEEE Global Telecommunications Conference'04*, March 2004.

[Paw81] R. F. Pawula. On the theory of error rates for narrow-band digital FM. *IEEE Transactions on Communications*, 29(11):1634-1643, November 1981.

[Pro01] John G. Proakis. Digital Communications. *McGraw-Hill Higher Education, Fourth Edition*, 2001.

[PYPJC01] C.-H. Park, Y.-H. You, J.-H. Paik, M.-C. Ju, and J.-W. Cho. Channel estimation and DC-offset compensation schemes for frequency-hopped Bluetooth networks. *IEEE Communications Letters*, 5:4-6, 2001.

[Rap96] T. S. Rappaport. Wireless Communications - Principles and Practice. *IEEE Press, New York*, 1996.

[Rim88] B. E. Rimoldi. A decomposition approach to CPM. *IEEE Transactions on Information Theory*, 34(2):260-270, March 1988.

[RPT95] R. Raheli, A. Polydoros, and C.-K. Tzou. Per-survivor processing: A general approach to MLE in uncertain environments. *IEEE Transactions on Communications*, 43(234):354-364, February-April 1995.

[SG99] R. Schober and W. H. Gerstacker. Metric for noncoherent sequence estimation. *Electronics Letters*, 35(25):2178-2179, December 1999.

[She01] R. Shepherd. Bluetooth wireless technology in the home. *Electronics and Communications Engineering Journal*, 13(5):195-203, October 2001.

[SHS03] R. Schiphorst, F. W. Hoeksema, and C. G. Slump. A (simplified) Bluetooth maximum a posteriori probability (MAP) receiver. In *Proceedings of IEEE Workshop on Signal Processing and Advance Wireless Communications, Rome*, June 2003.

[SJ03a] T. Scholand and P. Jung. Least squares based post-integration filtering for robust digital LDI receivers. In *Proceedings of IEEE ISSPIT, Darmstadt, Germany*, 2003.

[SJ03b] T. Scholand and P. Jung. Novel receiver structure for Bluetooth based on modified zero-crossing demodulation. In *Proceedings of IEEE Global Telecommunications Conference*, 2:729-733, December 2003.

[SW93] M. K. Simon and C. C. Wang. Differential versus limiter-discriminator detection of narrow-band FM. *IEEE Transactions on Communications*, 31(11):1227-1234, November 1983.

[SWJ04] T. Scholand, A. Waadt, and P. Jung. Max-log-ML symbol estimation post-processor for intermediate frequency LDI detectors. *Electronics Letters*, 40(5):183-184, February 2004.

[SV01a] A. Soltanian and R. E. Van Dyck. Physical Layer performance for coexistence of Bluetooth and IEEE 802.11b. In *Proceedings of Virginia Technology Symposium on Wireless Personal Communications, Blackburg, VA*, June 2001.

[SV01b] A. Soltanian and R. E. Van Dyck. Performance of the Bluetooth system in fading dispersive channels and interference. In *Proceedings of IEEE Global Telecommunications Conference*, pp:3499-3503, November 2001.

[TCKW85] T. Tjhung, N. Chun, Y. Kee, and P. Wittke. Error performance analysis for narrow-band duo-binary FM with discriminator detection. *IEEE Transactions on Communications*, 33(5):399-408, May 1985.

[Wic95] S. B. Wicker. Error control systems for digital communication and storage. *Prentice-Hall Inc., Upper Saddle River, New Jersey*, 1995.

[Wol78] J. Wolf. Efficient maximum-likelihood decoding of linear block codes using a trellis. *IEEE Transactions on Information Theory*, 24(1):76-80, January 1978.

[Zdnet] Richard Shim. *http://zdnet.com/2100-1104_2-5194762.html.* Broadcom to acquire Bluetooth company. CNET News.com, April 19, 2004.

[ZW99] H.-J. Zepernick and T. A. Wysocki. Multi-path channel parameters for the indoor radio at 2.4 GHz band. In *Proceedings of IEEE Vehicular Technology Conference*, pp:190-193, May 1999.